THE SYNTHESIS AND PHOTOPHYSICAL CHARACTERIZATION OF MACROCYCLIC CHROMIUM(III) COMPLEXES

by

Ashley Jo Schuman

A Dissertation

Submitted to the Faculty of Purdue University

In Partial Fulfillment of the Requirements for the degree of

Doctor of Philosophy

Department of Chemistry

West Lafayette, Indiana

August 2021

THE PURDUE UNIVERSITY GRADUATE SCHOOL
STATEMENT OF COMMITTEE APPROVAL

Dr. Tong Ren, Chair

Department of Chemistry

Dr. Suzanne Bart

Department of Chemistry

Dr. Christina Li

Department of Chemistry

Dr. Adam Wasserman

Department of Chemistry

Approved by:

Dr. Christine Hrycyna

To my Grammy.

ACKNOWLEDGMENTS

I would like to acknowledge the individuals who have provided encouragement and support during my graduate student lifetime. Graduate school presented several challenges, and I am grateful for those who stuck with me through it all.

To my first group at Purdue, the Taskernauts. Although the group was short-lived, the friendships were not. To Elijah, for sharing a garden with me and being a great listener. To Chris, for his perspective on life and help navigating educational research. To Kevin, for his hilarious analogies and data visualization skills. To Alex, for introducing me to activities and places in Lafayette. To Ashton, for inviting me to your sporting events and giving me the Hedwig keychain that I keep my lab keys on. To Jared, for telling the best dad jokes and being an endless source of positivity.

I never anticipated getting a PhD in inorganic chemistry, but the members of the Ren group made the transition manageable. I am blessed to have spent the last 3.5 years working with some wonderful people and am especially grateful to Dr. Ren for taking a chance on me. To Lyndsy, for being an excellent work bestie, carrying free furniture back to lab on my behalf, and quoting Jurassic Park more frequently than the average person. To Leo, for fueling my iced coffee addiction and always living his best life. To Adharsh, for his cat parenting advice, research insight, and encouragement to pursue a non-traditional career pathway. To Susie, for her pep talks and mentorship.

To the friends who made sure I had a life outside of lab. Elias, Cameron, Josh, Daria, Youlin, Kevin, and Jordan, thanks for the great times.

Finally, to my chosen family. To Michael, for his unwavering support and always making time for me. We have been on many adventures together and I cannot wait to see what our future holds. The cats and I are blessed to have him. To Squid and Otis, for their companionship, especially during the pandemic. May they continue to bring immense joy to my life.

TABLE OF CONTENTS

LIST OF TABLES 8
LIST OF FIGURES 9
LIST OF SCHEMES 11
LIST OF ABBREVIATIONS 12
ABSTRACT 13
CHAPTER 1. INTRODUCTION 14
1.1 Photophysics of Chromium(III) 14
1.2 Cyclam 15
1.3 Cr(cyclam) Bis-alkynyl Complexes 16
1.3.1 Origins 16
1.3.2 Magnetic Applications 16
1.3.3 Optoelectronic Applications 19
1.4 *C*-substituted Cyclam Derivatives and Cr^{III}(cyclam') Bis-alkynyl Complexes 21
1.5 References 22
CHAPTER 2. MACROCYCLIC CHROMIUM(III) CATECHOLATE COMPLEXES 24
2.1 Abstract 24
2.2 Introduction 24
2.3 Results and Discussion 26
2.3.1 Synthesis 26
2.3.2 Molecular Structures 27
2.3.3 Electrochemistry 31
2.3.4 UV-vis Spectroscopic Analysis 32
2.3.5 Emission Studies 33
2.3.6 Temperature-Dependent Magnetic Susceptibility 35
2.3.7 Density Functional Theory (DFT) Calculations 36
2.4 Conclusion 38
2.5 Experimental Section 38
2.6 Supporting Information 41
2.6.1 Crystallographic Details 41

2.6.2 Electrochemical Details 44
2.6.3 Absorption Details 45
2.6.4 Spectroelectrochemical Characterization of $[2.3]^{1+/2+}$ 46
2.6.5 Temperature Dependent Magnetic Susceptibility 46
2.6.6 Computational Details 49
2.7 References 51
CHAPTER 3. A UNIQUE SERIES OF CHROMIUM(III) MONO-ALKYNYL COMPLEXES SUPPORTED BY TETRAAZAMACROCYCLES 54
3.1 Abstract 54
3.2 Introduction 54
3.3 Results and Discussion 56
3.3.1 Synthesis 56
3.3.2 Molecular Structures 57
3.3.3 UV-vis Spectroscopic Analysis 61
3.3.4 Emission Studies 63
3.4 Conclusion 67
3.5 Experimental Section 67
3.6 Supporting Information 70
3.6.1 Synthetic Details 70
3.6.2 X-ray Crystallographic Details 71
3.6.3 Absorption Details 78
3.6.4 IR Characterization 80
3.6.5 Emission Details 81
3.7 References 87
CHAPTER 4. CHROMIUM(III) BIS-ALKYNYL COMPLEXES SUPPORTED BY *C*-SUBSTITUTED CYCLAM MPC 90
4.1 Abstract 90
4.2 Introduction 90
4.3 Results and Discussion 92
4.3.1 Synthesis 92
4.3.2 Molecular Structures 93

4.3.3 UV-vis Spectroscopic Analysis 96
4.3.4 Emission Studies 97
4.4 Conclusion 99
4.5 Experimental Section 99
4.6 Supporting Information 101
4.6.1 Synthetic Details 101
4.6.2 X-ray Crystallographic Details 102
4.6.3 Absorption Details 108
4.6.4 Emission Details 109
4.7 References 112
VITA 115
LIST OF PUBLICATIONS 116

LIST OF TABLES

Table 2.1. Selected bond lengths (Å) and angles (°) for $[2.1]^+$, $[2.2]^+$, $[2.3]^+$, and $[2.3]^{2+}$ 29

Table 2.2. Electrochemical Potentials (V, vs Fc^+/Fc) for $[2.1]^+$ – $[2.3]^+$ 31

Table 2.3. Photophysical Data for Complexes $[2.1]^+$, $[2.2]^+$, and $[2.3]^+$. 34

Table 3.1. Selected bond lengths (Å) and bond angles (°) for 3.1a – 3.4a. 60

Table 3.2. Photophysical data for mono-alkynyl complexes 3.1a – 3.4a and bis-alkynyl complexes 3.1b – 3.4b..... 66

Table 4.1. Selected bond lengths (Å) and bond angles (°) for 4.1 – 4.3. 96

Table 4.2. Photophysical data for complexes 4.1 – 4.3. 99

LIST OF FIGURES

Figure 1.1. Jablonski diagram with relevant photophysical processes (left) and microstates for relevant electronic states (right) for phosphorescent Cr(III) complexes of O_h symmetry. 14

Figure 1.2. Cyclam (left) and its five conformations adopted upon insertion of a transition metal (right). 16

Figure 1.3. *trans*-[Cr(cyclam)($C_2R)_2$][Ni($mdt)_2$] complexes. 17

Figure 1.4. *trans*-[Cr(cyclam)(C_2-MeEDT-TTF)$_2]^+$ cationic bis-alkynyl complex. 18

Figure 1.5. TTF-based alkynyl ligands. 18

Figure 1.6. *cis-/trans*-[Cr(cyclam)($C_2R)_2]^+$ complexes (left) and various R groups (right). 20

Figure 1.7. *C*-substituted cyclam derivatives. 21

Figure 2.1. ORTEP plot of $[2.1]^+$ at 30% probability level. Hydrogen atoms and Cl^- counteranion are omitted for clarity. 27

Figure 2.2. ORTEP plot of $[2.2]^+$ at 30% probability level. Hydrogen atoms and Cl^- counteranion are omitted for clarity. 28

Figure 2.3. ORTEP plot of $[2.3]^+$ at 30% probability level. Hydrogen atoms and PF_6^- counteranion are omitted for clarity. 28

Figure 2.4. ORTEP plot of $[2.3]^{2+}$ at 30% probability level. Hydrogen atoms and counteranions (Cl^- and PF_6^-) are omitted for clarity. 29

Figure 2.5. Cyclic voltammograms of $[2.1]^+$, $[2.2]^+$, and $[2.3]^+$ recorded at a 0.1 V/s scan rate in a 1.0 mM MeCN solution of 0.2 M *n*-Bu_4NPF_6. 31

Figure 2.6. Absorption spectra of $[2.1]^+$, $[2.2]^+$, and $[2.3]^+$ in MeCN with d−d transitions magnified in the inset. 32

Figure 2.7. Absorption spectra of $[2.3]^+$ and $[2.3]^{2+}$ in MeCN. 33

Figure 2.8. Time-delayed emission spectra of $[2.1]^+$, $[2.2]^+$, and $[2.3]^+$ at 77 K in 2-methyltetrahydrofuran at varying delay times. 34

Figure 2.9. Temperature dependent magnetic susceptibility of catecholate complexes $[2.2]^+$, $[2.3]^+$, and semiquinonate complex $[2.3]^{2+}$ from 1.8–300 K. The solid lines represent the fitting results. Courtesy of Z.-B. Hu. 35

Figure 2.10. Frontier molecular orbitals of $[2.1]^+$ (left), $[2.2]^+$ (center) and $[2.3]^+$ (right) derived from DFT calculations. MOs are plotted at |isovalue| = 0.025. Courtesy of A. Raghavan. 37

Figure 3.1. ORTEP plot of $[3.1a]^+$ at 30% probability level. H atoms and the Cl^- counterion were omitted for clarity. 58

Figure 3.2. ORTEP plot of $[3.2a]^+$ at 30% probability level. H atoms, $^-$OTf counterion, and disorder were omitted for clarity. 58

Figure 3.3. ORTEP plot of $[3.3a]^+$ at 30% probability level. H atoms, $^-$OTf counterion, and disorder were omitted for clarity. 59

Figure 3.4. ORTEP plot of $[3.4a]^+$ at 30% probability level. H atoms, $^-$OTf counterion, and disorder were omitted for clarity. 59

Figure 3.5. UV-vis absorption spectra of complexes 3.1a and 3.1b as CH_2Cl_2 solutions. 61

Figure 3.6. UV-vis absorption spectra of complexes 3.2a and 3.2b as CH_2Cl_2 solutions. 62

Figure 3.7. UV-vis absorption spectra of complexes 3.3a and 3.3b as CH_2Cl_2 solutions. 62

Figure 3.8. UV-vis absorption spectra of complexes 3.4a and 3.4b as CH_2Cl_2 solutions. 63

Figure 3.9. Normalized emission spectra of complexes 3.1a and 3.1b in a 4:1 EtOH/MeOH glass measured at 77 K. 64

Figure 3.10. Normalized emission spectra of complexes 3.2a and 3.2b in a 4:1 EtOH/MeOH glass measured at 77 K. 65

Figure 3.11. Normalized emission spectra of complexes 3.3a and 3.3b in a 4:1 EtOH/MeOH glass measured at 77 K. 65

Figure 3.12. Normalized emission spectra of complexes 3.4a and 3.4b in a 4:1 EtOH/MeOH glass measured at 77 K. 66

Figure 4.1. ORTEP plot of $[4.1]^+$ at 30% probability level. H atoms and the Cl^- counterion were omitted for clarity. 94

Figure 4.2. ORTEP plot of $[4.2]^+$ at 30% probability level. H atoms and disordered counterions (Cl^- and NO_3^-) were omitted for clarity. 94

Figure 4.3 ORTEP plot of $[4.3]^+$ at 30% probability level. H atoms, PF_6^- counterion, and disorder were omitted for clarity. 95

Figure 4.4. UV-vis absorption spectra of 4.1 – 4.3 as CH_2Cl_2 solutions. 96

Figure 4.5. Emission spectra of (a) 4.1, (b) 4.2, and (c) 4.3 at 77 K in 4:1 EtOH:MeOH and room temperature in degassed MeCN. 98

LIST OF SCHEMES

Scheme 2.1. Oxidation states of orthoquinones 25

Scheme 2.2. Synthesis of *cis*-Cr^{III}(HMC) catecholate complexes; $[2.1]^+$ = $[Cr^{III}(HMC)(Cat)]^+$, $[2.2]^+$ = $[Cr^{III}(HMC)(L2)]^+$, and $[2.3]^+$ = $[Cr^{III}(HMC)(L3)]^+$ 26

Scheme 3.1. General synthesis of Cr^{III}(HMC) mono-alkynyl complexes through acid degradation of Cr^{III}(HMC) bis-alkynyl complexes. 57

Scheme 4.1. Synthetic pathway for macrocyclic Cr^{III} alkynyl complexes. 91

Scheme 4.2. Synthesis of trans-$[Cr(MPC)(C_2Ar)_2]^+$ complexes. Conditions: (i) 5 eq LiC_2Ar in THF, 2 h 93

LIST OF ABBREVIATIONS

Cyclam	1,4,8,11-tetraazacyclotetradecane
Cyclam’	*C*-substituted derivatives of 1,4,8,11-tetraazacyclotetradecane
DMC	5,12-dimethyl-1,4,8,11-tetraazacyclotetradecane
HMC	5,5,7,12,12,14-hexamethyl-1,4,8,11-tetraazacyclotetradecane
MPC	5,12-dimethyl-7,14-diphenyl-1,4,8,11-tetraazacyclotetradecane
TMS	trimethylsilyl
UV-vis	Ultraviolet-visible
FT-IR	Fourier transform infrared radiation
ESI-MS	Electrospray ionization mass spectrometry
DFT	Density functional theory
HOMO	Highest occupied molecular orbital
LUMO	Lowest unoccupied molecular orbital
SOMO	Singly occupied molecular orbital
CV	Cyclic voltammetry
FC^+/FC	Ferrocenium/Ferrocene

ABSTRACT

Tetraazamacrocycles, such as cyclam (1,4,8,11-tetraazacyclotetradecane), are useful ancillary ligands in the formation of organometallic complexes. Coordination of a 3d metal can lead to the formation of square planar complexes, such as with Ni^{II} and Cu^{II}, or octahedral complexes upon coordination of additional ligands, such as with $Co^{II/III}$ and $Cr^{II/III}$. Notably with Cr, a mixture of *cis*- and *trans*- octahedral complexes are formed, and the isomerism can be influenced through *C*-substitution of the cyclam macrocycle. Herein, Cr^{III} complexes featuring *C*-substituted cyclam derivatives and either redox-active ligands or alkynyl ligands are reported.

Chapter 1 features an introduction to the photophysical processes of Cr(III), an overview of cyclam and its derivatives, and a brief review of Cr^{III}(cyclam/cyclam') bis-alkynyl complexes for various applications. Chapter 2 discusses the structural, optical, electronic, and magnetic characterizations of *cis*-[Cr(HMC)catecholate]$^{+}$ and *cis*-[Cr(HMC)semiquinonate]$^{2+}$ complexes, which feature redox-active catecholate and semiquinonate ligands. Chapter 3 highlights a series of *trans*-[Cr(HMC)(C_2Ar)Cl]$^{+}$ complexes, which expands upon prior research on bis-alkynyl complexes. Chapter 4 discusses how a different *C*-substituted cyclam derivative, MPC, is used to produce *trans*-[Cr(MPC)Cl_2]$^{+}$ starting material in higher quantity than the HMC derivative. This allows for higher amounts of *trans*-[Cr(MPC)(C_2Ar)$_2$]$^{+}$ complexes to be synthesized, making it a more practical macrocycle for the future pursuit of dissymmetric bis-alkynyl complexes.

CHAPTER 1. INTRODUCTION

This dissertation features macrocyclic chromium complexes with redox-active ligands (Chapter 2) and alkynyl ligands (Chapters 3 and 4). To better understand the research within, Chapter 1 provides a brief introduction to the photophysical processes of octahedral Cr(III) complexes, tetraazamacrocycles (cyclam and its derivatives), and previous Cr^{III}(cyclam/cyclam') bis-alkynyl complexes.

1.1 Photophysics of Chromium(III)

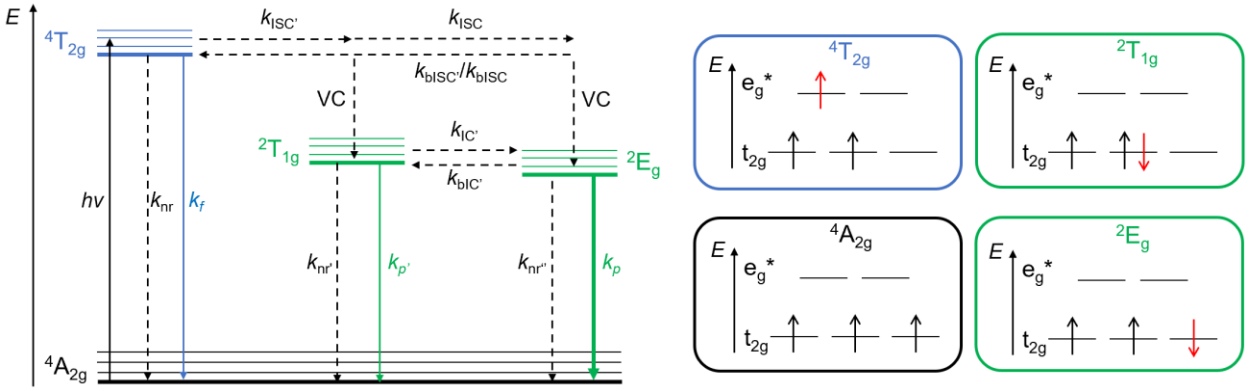

Figure 1.1. Jablonski diagram with relevant photophysical processes (left) and microstates for relevant electronic states (right) for phosphorescent Cr(III) complexes of O_h symmetry.[2]

It is pertinent to discuss the photophysical processes of octahedral Cr(III) complexes to understand the emission reported for the complexes in Chapters 2-4. The emission of Cr(III) complexes has been widely studied since the first known emissive Cr(III) complex,[1] and several reviews on this topic have been published.[2–4] As shown in the Jablonski diagram in Figure 1.7, a photon is absorbed by the complex, resulting in excitation of an electron to a high lying $^4T_{2g}$ state. Several excited state decay mechanisms may occur from this vibrationally excited $^4T_{2g}$ state. Fluorescence (k_f) is observed when the molecule returns to the ground state radiatively. Non-radiative decay (k_{nr}) to the $^4A_{2g}$ ground state is also possible. Alternatively, intersystem crossing (k_{ISC}) may occur to one of the two low-lying doublet states ($^2T_{1g}$ or ^2E_g) followed by vibrational cooling (VC). Phosphorescence (k_p) is observed upon radiative decay to the $^4A_{2g}$ ground state. Non-radiative decay pathways are also possible. Emission originates from the lowest excited level

or any levels in thermal equilibrium with it,[5] the latter of which can give rise to dual emission from the ^2E_g and $^2T_{1g}$ states.

The phosphorescence lifetimes of octahedral Cr(III) complexes largely depend on both the radiative and non-radiative decay pathways, of which multiple avenues are possible.[4] Although the emissive ^2E_g state is independent of ligand field strength, the $^4T_{2g}$ state is susceptible to changes in ligand field. For example, $[Cr(tpy)_2]^{3+}$ has a short phosphorescence lifetime because the small ligand field lowers the energy of the $^4T_{2g}$ state, making it similar in energy to the emissive ^2E_g state.[2] As a result, back intersystem crossing (k_{bISC}) from the ^2E_g state to the $^4T_{2g}$ state and non-radiative relaxation (k_{nr}) dominate over phosphorescence (k_p). Tetragonal and trigonal distortion of the excited states have also been known to increase k_{nr} and decrease the emission lifetimes of Cr(III) complexes.[4]

1.2 Cyclam

Cyclam (1,4,8,11-tetraazacyclotetradecane) and its derivatives are commonly used ancillary ligands in the synthesis of transition metal complexes. The resulting complexes are typically octahedral with coordinating ligands in the axial (*trans-)* position, but *cis*- complexes have been known with Co^{III}, Fe^{III}, Ni^{II}, and Cr^{III} metal centers.[6–9] As shown in Figure 1.2, cyclam has five configurations, which are named according to the stereochemistry around the N atoms: *trans-I* (RSRS), *trans-II* (RRRS), *trans-III* (RRSS), *trans-IV* (RSSR), and *trans-V* (RRRR).[10] The *trans-III* conformation is the most stable arrangement, as it permits the five-membered MN_2C_2 rings to be gauche while allowing the six-membered MN_2C_3 rings to adopt the chair conformation.[6] The *trans-III* conformation is adopted by the *trans*-$[Cr(HMC)(C_2Ar)_2]^+$ and *trans*-$[Cr(HMC)(C_2Ar)Cl]^+$ complexes featured in Chapter 3, and the *trans*-$[Cr(MPC)(C_2Ar)_2]^+$ complexes discussed in Chapter 4, where HMC and MPC are the *C*-substituted cyclam derivatives (further discussed in Section 1.4). The *trans-V* arrangement is the most favorable for *cis*-complexes, as seen in the crystal structures of the *cis*-[Cr(HMC)(catecholate)]$^+$ complexes featured in Chapter 2.

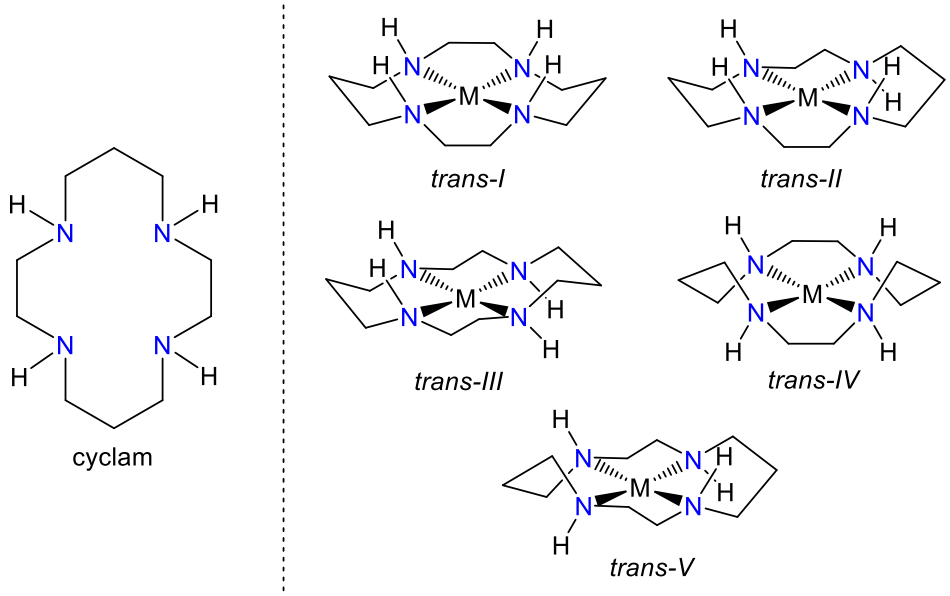

Figure 1.2. Cyclam (left) and its five conformations adopted upon insertion of a transition metal (right).[10]

1.3 Cr(cyclam) Bis-alkynyl Complexes

1.3.1 Origins

Berben and Long reported the first known *trans*-$[Cr^{III}(cyclam)(C_2R)_2]^+$ complexes in the pursuit of building blocks for single-molecule magnetic materials (R = H, $SiMe_3$, and *m*-PhC_2H).[11] Acetylide ligands were chosen as an alternative to their previously studied cyano complexes because their higher charge and symmetric nature should enhance the orbital overlap between Cr and C≡C, and thus increase the strength of magnetic exchange coupling. Efforts were made to synthesize hexagon shaped molecules composed of Cr(cyclam) bridged by 1,3-$Ph(C_2H)$; however, only *trans*-$[Cr(cyclam)(C_2$-*m*-$PhC_2H)_2]^+$ was formed. Although only the synthesis and structural properties of the Cr(cyclam) bis-alkynyl complexes were reported, Berben's dissertation paved the way for other groups to explore the structural, magnetic, and optical properties of *trans*-$[Cr(cyclam)(C_2R)_2]^+$ type complexes.

1.3.2 Magnetic Applications

Nishi and Nishijo have explored the structural and magnetic properties of several *trans*-$[Cr(cyclam)(C_2R)_2]^+$ type cations in the pursuit of molecule-based magnetic materials. To promote

strong π–d interactions, an ethynyl linker is employed to connect a conjugated molecule to the *S* = 3/2 Cr^{III}(cyclam) center. In addition to modification of the cationic complexes, they have investigated the effects of various counteranions and solvates on the magnetic properties.[12–17]

Nishi and Nishijo's earliest work pairs *trans*-$[Cr(cyclam)(C_2\text{-3-thiophene})_2]^+$ and *trans*-$[Cr(cyclam)(C_2Ph)_2]^+$ with $[Ni(mdt)_2]^-$ (mdt = 1,3-dithiole-4,5-dithiolate), as shown in Figure 1.3.[12] The transition metal dithiolate counteranion was selected because of its large π-orbital perpendicular to the molecular plane, which may result in enhanced intermolecular orbital overlap and strong exchange interaction. A ferrimagnetic transition was observed at 2.3 K as a result of weak interchain antiferrimagnetic interactions between the $[Cr(cyclam)(C_2\text{-3-thiophene})_2]^+$ and $[Ni(mdt)_2]^-$.

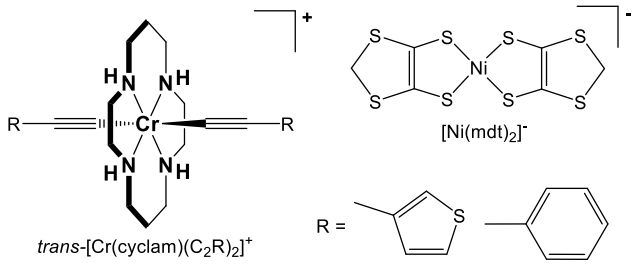

Figure 1.3. *trans*-$[Cr(cyclam)(C_2R)_2][Ni(mdt)_2]$ complexes.

Efforts then shifted to tetrathiafulvalene (TTF) based alkynyl ligands. Electrochemical oxidation of *trans*-$[Cr^{III}(cyclam)(C_2\text{-MeEDT-TTF})_2]^{n+}$ type complexes (as shown in Figure 1.4; MeEDT-TTF = 5-methyl-4',5'-ethylenedithio-TTF) led to the dimerization of tetrathiafulvalene ligands on adjacent complexes, resulting in delocalization of a cationic charge and spin over the dimer.[13] This delocalization and the d–π intramolecular interaction between Cr^{III} and the TTF-acetylide ligand gave rise to high ferromagnetic transition temperatures (23.0 K) for the ClO_4^- and BH_4^- salts. Nishijo's subsequent study of the structural and magnetic properties of *trans*-$[Cr(cyclam)(C_2\text{-MeEDT-TTF})][Anion]_2(Solvent1)_2(Solvent2)$ type complexes explored the varied distance between the ferrimagnetic chains (Anion = BF_4^-, ClO_4^-, ReO_4^-; Solvent 1 = PhF, PhCl, PhBr, PhI; Solvent 2 = MeCN, PhBr, PhI).[14] As the interchain distance decreased, the weak ferromagnetic transition temperature increased from 14.5 to 26.0 K. The investigation of *trans*-$[Cr^{III}(cyclam)(C_2\text{-MeEDT-TTF})_2]^{n+}$ paired with TCNQ (7,7,8,8-tetracyanoquinodimethane) revealed that neutral TCNQ molecules stack in between the TTF ligands to form a charge transfer

complex in crystals of *trans*-[Cr(cyclam)(C_2-MeEDT-TTF)$_2$](TCNQ)$_3$.[15] These crystals exhibited a ferrimagnetic transition at 4.8 K.

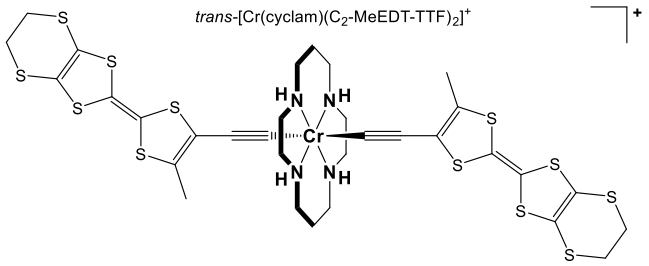

Figure 1.4. *trans*-[Cr(cyclam)(C_2-MeEDT-TTF)$_2$]$^+$ cationic bis-alkynyl complex.

Nishijo's subsequent projects modified the TTF ligand framework, as shown in Figure 1.5. Electrochemical oxidation of *trans*-[Cr(cyclam)(C_2-MeBMT-TTF)$_2$]$^{n+}$ (MeBMT-TTF = 5-methyl-4',5'-bis(methylthio)TTF) and *trans*-[Cr(cyclam)(C_2-MeEDO-TTF)$_2$]$^{n+}$ (MeEDO = MeEDO-TTF = 5-methyl-4',5'-ethylenedioxyTTF) resulted in the formation of various salts.[16] The crystals structures contain a chain of Cr^{III}(cyclam)-acetylide-TTF type complexes, where adjacent TTF ligands form a dimer, as observed for the C_2-MeEDT-TTF bis-alkynyl complexes. A weak ferromagnetic transition was observed at 21 K for *trans*-[Cr(cyclam)(C_2-MeEDO-TTF)$_2$](ClO_4)$_2$(PhCl)(H_2O)$_2$ as a result of weak antiferromagnetic interaction of the TTF dimers and single-ion anisotropy of a TTF-type ligand.

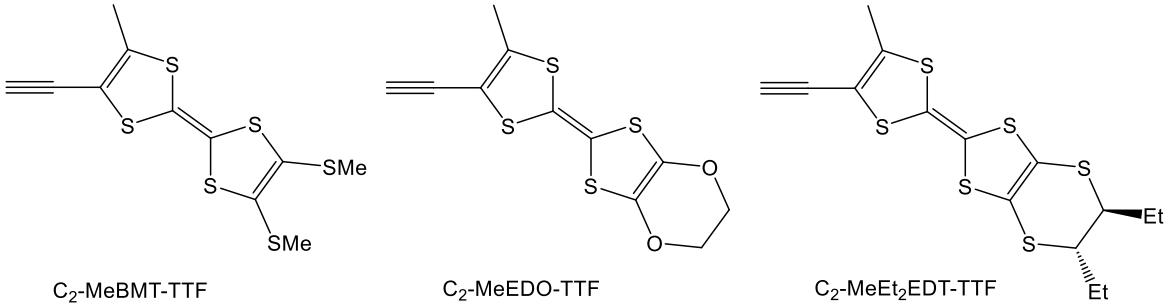

Figure 1.5. TTF-based alkynyl ligands.

Additional work with the modified ethynyl-TTF ligand C_2-MeEt$_2$EDT-TTF paired cationionic Cr(cyclam) bis-alkynyl complexes with two transition metal dithiolate counteranions to form *trans*-[Cr(cyclam)(C_2-MeEt$_2$EDT-TTF)$_2$][[Ni(mnt)$_2$]$_3$ and *trans*-[Cr(cyclam)(C_2-

$MeEt_2EDT\text{-}TTF)_2$][[Ni(dmit)$_2$] complexes (mnt = maleonitriledithiolate; dmit = 2-thioxo-1,3-dithiole-4,5-dithiolate).[17] The *trans*- diethyl groups in the axial position impeded π-stacking of the TTF units and [Ni(dmit)]$^-$, which resulted in weak spin-spin interactions between Cr(III) and the anion. The *trans*- diethyl groups in the equatorial position allowed the π-stacking of TTF units and the [Ni(mnt)$_2$]$^-$ anions, which behaved as a one-dimensional S = 1/2 antiferromagnetic chain and connected the S = 3/2 Cr^{III} antiferromagnetically.

1.3.3 Optoelectronic Applications

The Wagenknecht group has synthesized and characterized several *cis-/trans*-[Cr(cyclam)(C_2R)$_2$]$^+$ type complexes to examine the intramolecular energy transfer between Cr^{III} and alkynyl ligands, shown in Figure 1.6. An initial communication provided the structural analysis of *trans*-[Cr(cyclam)(C_2Ph)$_2$]$^+$ and the resulting vibrational and optical spectroscopic characterizations.[18] Synthesis and spectroscopic characterizations were also provided for R = CH_3 and CF_3 complexes. A follow-up article reported a series of *cis-/trans*-[Cr(cyclam)(C_2R)$_2$]$^+$ complexes (R = Ph, $PhCH_3$, $PhCF_3$, PhF, cyclohexane, Np, Ant, and PhCN).[19] Vibrational spectroscopy confirmed the presence of a C≡C bond, UV-vis showed vibronically structured d–d transitions that partake in intensity stealing from a MLCT band, low temperature emission from the $^2T_{1g} \rightarrow {}^4A_{2g}$ (O_h) was observed, and emission lifetimes were determined. Deuterated cyclam (amine N–D) and phenylacetylene (C–D) were employed to establish the effect of deuteration on the lifetimes of *trans*-[Cr(cyclam)(C_2Ph)$_2$]$^+$ at 77 K and room temperature. No isotope effect was observed for the deuterated aryl ring, however, the deuterated cyclam complexes experienced a ~4x increase in lifetime, indicating the N–H bonds are coupled to the $^2T_{1g}$ excited state and have a significant effect on the excited state relaxation pathways.

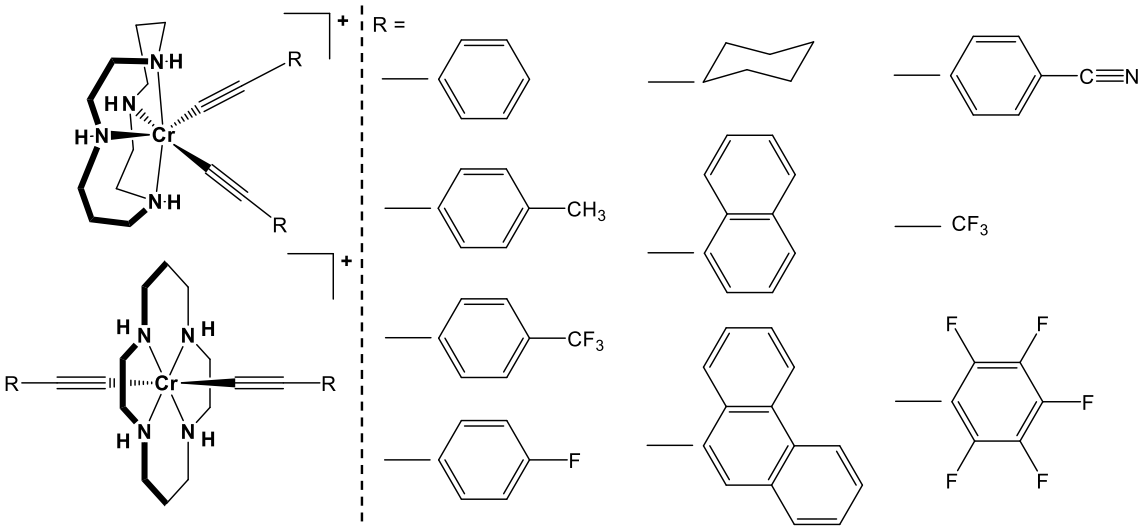

Figure 1.6. *cis-/trans*-[Cr(cyclam)($C_2R)_2$]$^+$ complexes (left) and various R groups (right).

In the pursuit of a bis-alkynyl complex with similar properties to *trans*-[Cr(cyclam)$(CN)_2]^+$, the Wagenknecht lab synthesized and characterized *trans*-[Cr(cyclam)$(C_2CF_3)_2]^+$.[20] They reported that the trifluoropropynyl ligand more closely resembles the CN^- ligand than their previously reported arylalkynyl Cr(cyclam) complexes on the basis of emission from the ^2E_g state (instead of the $^2T_{1g}$ state) and phosphorescence lifetime comparisons. The structural analysis of *cis*-[Cr(cyclam)$(C_2Ph)_2]^+$ and the optimized synthesis and photophysical characterization of *cis*-[Cr(cyclam)$(C_2CF_3)_2]^+$ was reported in a subsequent publication.[5] A new complex, *trans*-[Cr(cyclam)$(C_2C_6F_5)_2]^+$, was synthesized to compare the fluorinated electron withdrawing alkynyl ligand with the previously employed C_2CF_3 ligand.[21] The absorption spectrum showed vibronic structuring similar to previously reported arylalkynyl complexes, although structuring was not observed in the spectrum of the C_2CF_3 complex. The emission spectrum was also similar to arylalkynyl complexes, indicating that the $C_2C_6F_5$ ligand is a better π donor than C_2CF_3 despite both containing electron withdrawing groups.

Collaboration between the Wagenknecht and Ren groups led to the realization of Cr(cyclam) bis-alkynyl complexes with cross-conjugated *gem*-DEE ligands (*gem*-DEE = *geminal*-diethynylethene).[22] It was found that the *gem*-DEE ligands behave similarly to linear alkynyl ligands, though *gem*-DEE acts as a better π donor.

1.4 *C*-substituted Cyclam Derivatives and Cr^{III}(cyclam') Bis-alkynyl Complexes

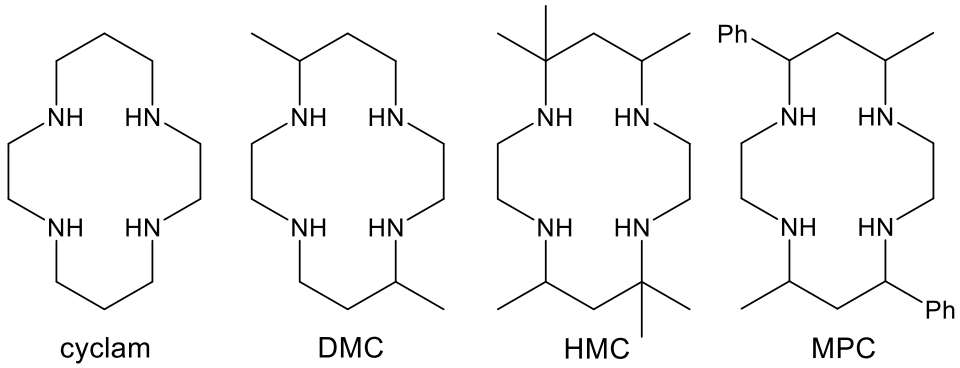

Figure 1.7. *C*-substituted cyclam derivatives.

The *C*-substituted cyclam derivatives DMC (5,12-dimethyl-1,4,8,11-tetraazacyclotetradecane), HMC (5,5,7,12,12,14-hexamethyl-1,4,8,11-tetraazacyclotetradecane), and MPC (5,12-dimethyl-7,14-diphenyl-1,4,8,11-tetraazacyclotetradecane), shown in Figure 1.7, have previously been used by the Ren group to form transition metal complexes of Co(III), Ni(II), Fe(III), and/or Cr(III).[22–30] In regards to Cr^{III} complexes, the *C*-substituted cyclam derivatives are advantageous because of the facile separation of *cis*-/*trans*-$[Cr(cyclam')Cl_2]^+$ starting materials. Moreover, the orientation of the substituents can strongly encourage *cis*- or *trans*- coordination geometries. For example, the *meso* and *racemic* conformations of HMC enforce the *trans* and *cis* geometries, respectively, in a variety of complexes.[30] Research on $[Cr(HMC)(C_2R)_2]^+$ complexes (R = Ph, C_2SiMe_3) indicated the bis-alkynyl complexes retain their *cis* and *trans* ligand coordination after the arylalkynylation of *cis*-/*trans*-$[Cr(HMC)Cl_2]Cl$.[23,25] In contrast, arylalkynylation of *cis*-$[Cr(DMC)Cl_2]Cl$ yielded a mixture of *cis*- and *trans*-$[Cr(DMC)(C_2R)_2]Cl$ products (R = Ph, Fc, H, and C_2TMS).[25] Unsubstituted $[Cr(cyclam)(C_2R)_2]^+$ type complexes tend to prefer the *trans*- orientation, with limited examples of preference towards the *cis*- orientation.[9] Only *trans*-$[Cr(MPC)(C_2R)_2]^+$ complexes have thus far been isolated (Chapter 4).

1.5 References

1. K. DeArmond and L. S. Forster, *J. Chem. Phys.*, **1940**, 8, 790–797

2. C. Förster and K. Heinze, *Chem. Soc. Rev.*, 2020, **49**, 1057–1070

3. A. D. Kirk, *Chem. Rev.*, 1999, **99**, 1607–1640

4. L. S. Forster, *Chem. Rev.*, 1990, **90**, 331–353

5. J. N. Demas and G. A. Crosby, *J. Am. Chem. Soc.*, 1970, **92**, 7762–7270

6. L. F. Lindoy, *The Chemistry of Macrocyclic Ligand Complexes*, Cambridge University Press, Cambridge, 1989

7. R. Guilard, O. Siri, A. Tabard, G. Broeker, P. Richard, D. J. Nurco and K. M. Smith, *J. Chem. Soc. Dalton Trans.*, 1997, 3459–3463

8. E. J. Billo, *Inorg. Chem.*, 1981, **20**, 4019–4021

9. P. U. Thakker, C. Sun, L. Khulordava, C. D. McMillen and P. S. Wagenknecht, *J. Organomet. Chem.*, 2014, **772-773**, 107–112

10. E. K. Barefield, *Coord. Chem. Rev*., 2010, **254**, 1607–1624

11. L. A. Berben, Ph.D. Dissertation, University of California, Berkeley, 2005

12. J. Nishijo, K. Judai, S. Numao and N. Nishi, *Inorg. Chem*., 2009, **48**, 9402–9408

13. J. Nishijo, K. Judai and N. Nishi, *Inorg. Chem.*, 2011, **50**, 3446–3470

14. J. Nishijo and M. Enomoto, *Inorg. Chem*., 2013, **52**, 13263–13268

15. J. Nishijo, *Polyhedron*, 2013, **66**, 43–47

16. J. Nishijo, Y. Shima and M. Enomoto, *Polyhedron*, 2017, **136**, 35–41

17. J. Nishijo, M. Uchida, M. Enomoto and M. Akita, *Transit. Met. Chem.*, 2021, **46**, 373–380

18. D. L. Grisenti, W. W. Thomas, C. R. Turlington, M. D. Newsom, C. J. Priedemann, D. G. VanDerveer and P. S. Wagenknecht, *Inorg. Chem*., 2008, **47**, 11452–11454

19. C. Sun, C. R. Turlington, W. W. Thomas, J. H. Wade, W. M. Stout, D. L. Grisenti, W. P. Forrest, D. G. VanDerveer and P. S. Wagenknecht, *Inorg. Chem*., 2011, **50**, 9354–9364

20. C. Sun, P. U. Thakker, L. Khulordava, D. J. Tobben, S. M. Greenstein, D. L. Grisenti, A. G. Kantor and P. S. Wagenknecht, *Inorg. Chem.*, 2012, **51**, 10477–10479

21. L. E. Eddy, P. U. Thakker, C. D. McMillen, J. A. Pienkos, J. J. Cordoba, C. E. Edmunds and P. S. Wagenknecht, *Inorg. Chim. Acta*., 2019, **486**, 141–149

22. W. P. Forrest, Z. Cao, R. Hambrick, B. M. Prentice, P. E. Fanwick, P. S. Wagenknecht and T. Ren, *Eur. J. Inorg. Chem.*, 2012, **2012**, 5616–5620

23. S. F. Tyler, E. C. Judkins, Y. Song, F. Cao, D. R. McMillin, P. E. Fanwick and T. Ren, *Inorg. Chem.*, 2016, **55**, 8736–8743

24. E. C. Judkins, S. F. Tyler, M. Zeller, P. E. Fanwick and T. Ren, *Eur. J. Inorg. Chem.*, 2017, **2017**, 4068–4076

25. E. C. Judkins, M. Zeller and T. Ren, *Inorg. Chem.*, 2018, **57**, 2249–2259

26. T. D. Cook, S. F. Tyler, C. M. McGuire, M. Zeller, P. E. Fanwick, D. H. Evans, D. G. Peters and T. Ren, *ACS Omega*, 2017, **2**, 3966–3976

27. B. M. Oxley, B. L. Mash, M. Zeller, S. D. C. Banziger and T. Ren, *Acta Cryst. E.*, 2018, **74**, 522–529

28. B. L. Mash and T. Ren, *J. Organomet. Chem.*, 2019, **880**, 143–149

29. R. A. Clendening, M. Zeller and T. Ren, *Acta Cryst. C.*, 2019, **75**, 1509–1516

30. B. L. Mash, Y. Yang and T. Ren, *Organometallics*, 2020, **39**, 2019–2025

31. D. A. House, R. W. Hay and M. A. Ali, *Inorg. Chim. Acta*, 1983, **72**, 239–245

CHAPTER 2. MACROCYCLIC CHROMIUM(III) CATECHOLATE COMPLEXES

Reprinted (adapted) with permission from A. J. Schuman, A. Raghavan, S. D. C. Banziger, Z.-B. Hu, B. L. Mash, A. L. Williams and T. Ren, *Inorg. Chem.*, 2021, **60**, 4447–4455. Copyright 2021, American Chemical Society. DOI: 10.1021/acs.inorgchem.0c03224

2.1 Abstract

The synthesis and structural, electrochemical, spectroscopic, and magnetic characterizations of Cr^{III}(HMC) catecholate and semiquinonate complexes are reported herein, where HMC is 5,5,7,12,12,14-hexamethyl-1,4,8,11-tetraazacyclotetradecane. *cis*-$[Cr(HMC)(Cat)]^+$ complexes (Cat = catecholate, [**2.1**]$^+$; tetrachlorocatecholate, [**2.2**]$^+$; and 3,5-di-*tert*-butylcatecholate, [**2.3**]$^+$) were prepared from the reaction between the appropriate catechol and $[Cr^{III}(HMC)Cl_2]Cl$ reduced in situ by zinc. Chemical oxidation of [**2.3**]$^+$ by $FcPF_6$ resulted in *cis*-$[Cr(HMC)(SQ)]^{2+}$ ([**2.3**]$^{2+}$, SQ = 3,5-di-*tert*-butylsemiquinonate). Single crystal X-ray diffraction studies revealed the *cis*-chelation of the Cat/SQ ligand around the Cr metal center and confirmed the Cat/SQ nature of the ligands. Reversible oxidations of Cat to SQ were observed in the cyclic voltammograms of [**2.1**]$^+$ – [**2.3**]$^+$, while the Cr^{III} center remains redox inactive. The absorption spectrum of the SQ complex [**2.3**]$^{2+}$ exhibits an intense spin-forbidden transition in solution. Time-delayed phosphorescence spectra recorded at 77 K revealed that all catecholate complexes emit from the ^2E state, while [**2.2**]$^+$ also emits from the $^2T_1$ state. Temperature-dependent magnetic susceptibility measurements indicate the Cat complexes exist as $S = 3/2$ systems, while the SQ complex behaves as an $S = 1$ system, resulting from strong antiferromagnetic coupling of the $S = 3/2$ Cr center with the $S = 1/2$ SQ radical. Density functional theory (DFT) shows the similarities between the SOMOs of [**2.1**]$^+$ and [**2.2**]$^+$ and differences in their LUMOs in the ground state.

2.2 Introduction

Redox-active ligands have been of recent interest due to their ability to serve as an electron reservoir for transition metal catalysts.[1,2] Catecholate and its derivatives are the classic example of such ligands, which may exist in three valence states depending on the coordination environment: catecholate (Cat), semiquinonate (SQ), and benzoquinone (BQ) (Scheme 2.1).[3,4] Cat and SQ are

known to readily coordinate to 3d transition metals, while BQ complexes remain elusive in the literature.[5] Cat/SQ complexes containing Mn, Fe, and Cu have been examined for various biological applications,[6] especially modeling the chemistry of catechol dioxygenases.[7–9] Co Cat/SQ complexes exhibit valence tautomerism,[10,11] making them a strong candidate for molecular switches and spin-crossover materials.[12,13] Metal−organic frameworks bridged by chloranilate (dianion of 3,6-dichloro-2,5-dihydroxy-1,4-benzoquinone) exhibited exceptionally high magnetic ordering temperature (M = Fe)[14] and expedient metal transport (M = Mn).[15]

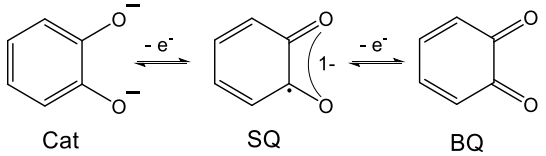

Scheme 2.1. Oxidation states of orthoquinones

Metal−Cat/SQ complexes supported by an ancillary ligand (L) can be found throughout the literature. Paramagnetic metal-semiquinone systems are of interest because they contain only two components with unpaired spin, enabling the study of exchange coupling effects on electronic and photochemical properties. The photophysical properties of chromium(III) complexes are well established in the absence of electron exchange,[16–18] making chromium(III) Cat/SQ complexes ideal candidates for further study. The Cat/SQ ligand allows for exchange coupling to be turned on (SQ) or off (Cat) based on the oxidation state of the ligand, without altering the composition of the complex ion. Variation of the steric and electronic structure of L enables further tuning of M−Cat interactions in *cis*-$[M(L)Cat)]^+$ complexes.[3,4] Dei and co-workers have investigated a number of catecholate metal complexes supported by HMC (5,5,7,12,12,14-hexamethyl,1,4,8,11-tetraazacyclotetradecane, abbreviated as "CTH" by Dei) with metal center as Mn,[19,20] Fe,[20,21] Co,[22,23] Ni,[20,24–27] and Rh.[25] Especially relevant to this work, $Cr^{II}(HMC)Cl_2$ reacted with 3,5-di-*tert*-butylbenzoquinone (DTBBQ) or tetrachlorobenzoquinone (TCBQ) to afford the semiquinonate complex $[Cr^{III}(HMC)(DTBSQ)]^{2+}$ or the catecholate complex $[Cr^{III}(HMC)(TCCat)]^+$, respectively, and an intense spin-forbidden transition ($^4A_2 \rightarrow {}^2E$) was identified for the semiquinonate complexes.[28] Similarly, the reaction between $Cr^{II}(HMC)Cl_2$ and 2,5-dihydroxy-1,4-benzoquinone (H_2DHBQ) afforded a tetraoxolene-bridged Cr^{III} dimer.[20] While these results are interesting, none of the Cr^{III}(HMC) based complexes were structurally

characterized, hence leaving the structure-property relationship ambiguous. Additionally, work on Cr(HMC) by Dei focused on species with SQ ligands, leaving species with Cat ligands underexplored.

Described in this contribution are facile preparation of complexes [**2.1**]$^{+}$ ([Cr(HMC)(catecholate)]$^{+}$), [**2.2**]$^{+}$ ([Cr(HMC)(tetrachlorocatecholate)]$^{+}$), and [**2.3**]$^{+}$ (([Cr(HMC)(3,5-di-*tert*-butylcatecholate)]$^{+}$, Scheme 2.2) and subsequent conversion of [**2.3**]$^{+}$ to [**2.3**]$^{2+}$ and molecular structures of complexes [**2.1**]$^{+}$, [**2.2**]$^{+}$, [**2.3**]$^{+}$, and [**2.3**]$^{2+}$. Complexes [**2.1**]$^{+}$ – [**2.3**]$^{+}$ were further characterized with voltammetric and emission spectroscopic techniques. Variable temperature magnetic susceptibility measurements were conducted for complexes [**2.2**]$^{+}$, [**2.3**]$^{+}$, and [**2.3**]$^{2+}$. DFT calculations were performed on [**2.1**]$^{+}$, [**2.2**]$^{+}$, [**2.3**]$^{+}$, and [**2.3**]$^{2+}$ to better understand the ground state electronic structures of these complexes.

2.3 Results and Discussion

2.3.1 Synthesis

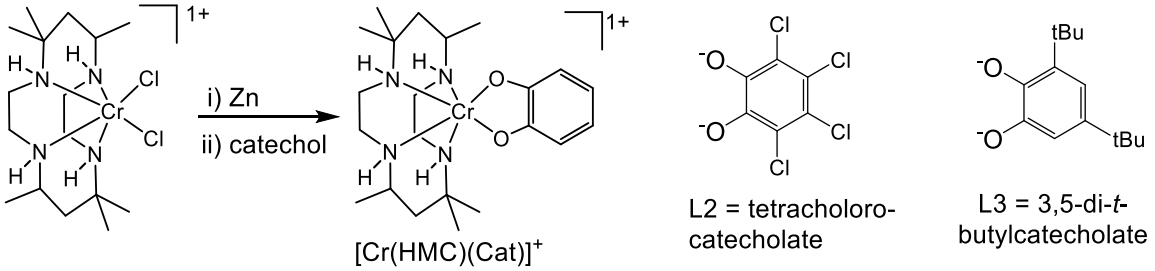

Scheme 2.2. Synthesis of *cis*-Cr^{III}(HMC) catecholate complexes; [**2.1**]$^{+}$ = [Cr^{III}(HMC)(Cat)]$^{+}$, [**2.2**]$^{+}$ = [Cr^{III}(HMC)(L2)]$^{+}$, and [**2.3**]$^{+}$ = [Cr^{III}(HMC)(L3)]$^{+}$

In general, *cis*-[Cr(HMC)Cl$_2$]Cl reacted with the corresponding catechol ligand upon in situ reduction of Cr^{III} to Cr^{II} using mossy Zn, as shown in Scheme 2.2. Cr^{III} complexes were formed upon oxidation of Cr^{II} complexes in air. The reaction between *cis*-[Cr(HMC)Cl$_2$]Cl and 1 equiv of catechol under reflux yielded complex [**2.1**]Cl as a forest green powder in 69% yield after purification over a silica plug. Complex [**2.2**]Cl was synthesized by using the same procedure and isolated as a sky blue powder in 62% yield after purification. Complex [**2.3**]Cl was obtained in a similar manner and isolated as [**2.3**]PF$_6$ in 65% yield after an anion exchange using KPF$_6$(aq) and extraction in EtOAc. Chemical oxidation of [**2.3**]PF$_6$ with FcPF$_6$ yields [**2.3**](PF$_6$)$_{1.5}$Cl$_{0.5}$ (see the

discussion below regarding the presence of 0.5 equiv of Cl^-) as a jade green powder in 89% yield. As noted earlier, the previous syntheses of Cr^{III}(HMC) complexes by Dei started from air-sensitive Cr^{II}(HMC)Cl_2, and the yields were not reported.[20,28] Our approach, overcoming the kinetic inertness of Cr^{III} through an in situ reduction, is more straightforward and could be applicable for preparation of other Cr^{III} complexes.

2.3.2 Molecular Structures

Single crystals of [**2.1**]Cl, [**2.2**]Cl, [**2.3**]PF_6, and [**2.3**]$(PF_6)_{1.5}Cl_{0.5}$ were grown via slow diffusion of hexanes into either a CH_2Cl_2 solution ([**2.1**]Cl, [**2.2**]Cl) or a benzene solution ([**2.3**]PF_6) or vapor diffusion of Et_2O into a MeCN solution ([**2.3**]$(PF_6)_{1.5}Cl_{0.5}$). The molecular structures determined from single crystal X-ray diffraction are shown in Figures 2.1−2.4, which show the *cis*-chelation of the catecholate/semiquinonate ligand. The N1−Cr1−N3 bond angles, as listed in Table 2.1, range between 168.48° and 172.68° for all four compounds, indicative of pseudo-octahedral coordination.

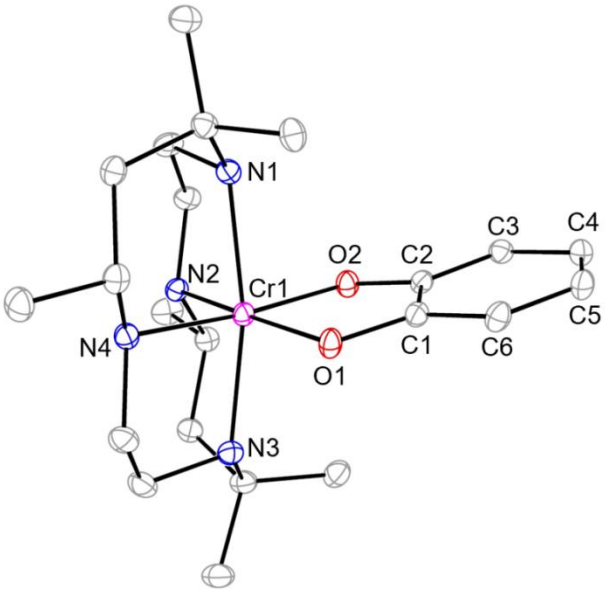

Figure 2.1. ORTEP plot of [**2.1**]$^+$ at 30% probability level. Hydrogen atoms and Cl^- counteranion are omitted for clarity.

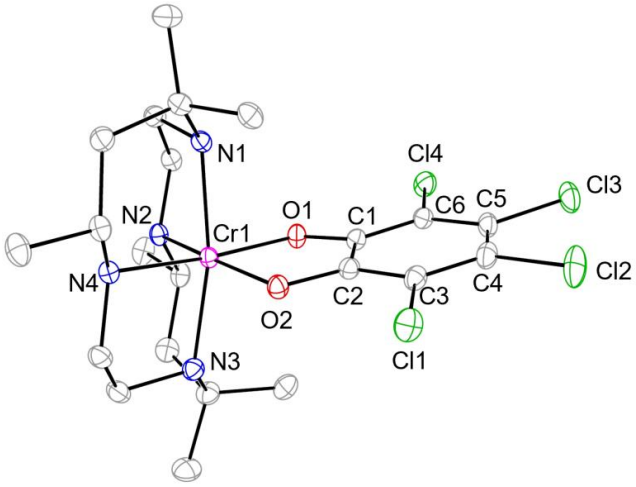

Figure 2.2. ORTEP plot of [**2.2**]$^{+}$ at 30% probability level. Hydrogen atoms and Cl^{-} counteranion are omitted for clarity.

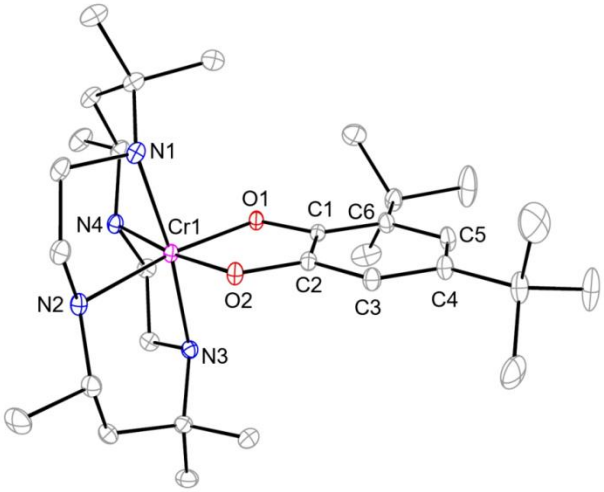

Figure 2.3. ORTEP plot of [**2.3**]$^{+}$ at 30% probability level. Hydrogen atoms and PF_6^{-} counteranion are omitted for clarity.

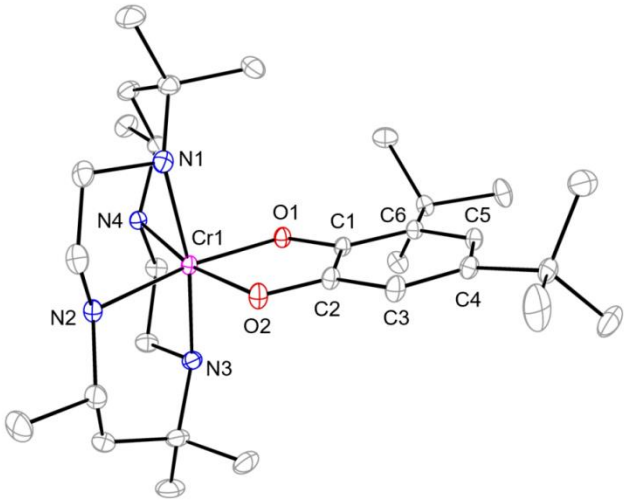

Figure 2.4. ORTEP plot of [**2.3**]$^{2+}$ at 30% probability level. Hydrogen atoms and counteranions (Cl^- and PF_6^-) are omitted for clarity.

Table 2.1. Selected bond lengths (Å) and angles (°) for [**2.1**]$^+$, [**2.2**]$^+$, [**2.3**]$^+$, and [**2.3**]$^{2+}$

	[**2.1**]$^+$	[**2.2**]$^+$	[**2.3**]$^+$	[**2.3**]$^{2+}$
Cr1–N1	2.143(2)	2.121(2)	2.124(1)	2.140(1)
Cr1–N2	2.112(2)	2.094(1)	2.122(1)	2.094(1)
Cr1–N3	2.138(2)	2.124(2)	2.127(1)	2.135(1)
Cr1–N4	2.122(2)	2.125(1)	2.123(1)	2.089(1)
Cr1–O1	1.940(2)	1.961(1)	1.920(1)	1.9469(9)
Cr1–O2	1.953(1)	1.941(1)	1.908(1)	1.943(1)
O1–C1	1.349(2)	1.341(2)	1.366(2)	1.304(2)
O2–C2	1.365(3)	1.329(2)	1.359(2)	1.301(2)
C1–C2	1.419(3)	1.419(2)	1.411(2)	1.442(2)
C2–C3	1.387(3)	1.387(2)	1.389(2)	1.412(2)
C3–C4	1.396(3)	1.401(2)	1.396(2)	1.370(2)
C4–C5	1.388(3)	1.387(3)	1.400(2)	1.444(2)
C5–C6	1.404(3)	1.405(2)	1.410(2)	1.378(2)
C6–C1	1.387(3)	1.391(2)	1.402(2)	1.428(2)
O1–Cr1–O2	84.56(6)	84.02(5)	85.57(4)	81.27(5)
Cr1–O1–C1	111.31(2)	110.45(5)	111.01(8)	114.93(9)
Cr1–O2–C2	110.52(2)	111.62(5)	111.15(8)	114.4(1)
N1–Cr1–N3	168.64(7)	168.48(6)	172.68(5)	169.06(5)

The lattice of complex [**2.3**]$^{2+}$ contains a cavity in which the hydrogen atoms of N2 and N4 face inward. Strong hydrogen bond interactions paired with the possibility for two cationic units to face each other create an encapsulated point which can contain a single hydrogen bond accepting atom. This results in partial occupation of a Cl^- anion contained in the pocket, which could not be

removed despite attempts of anion exchange. The formula is then [**2.3**]$(PF_6)_{1.5}Cl_{0.5}$ exactly, with one chloride residing on a crystallographic 2-fold axis and being encapsulated between two symmetry-related [**2.3**]$^{2+}$. A structural plot depicting two cationic units and the encapsulated chloride anion is provided in Figure 2.S1. A nearly identical formula, "$[Cr(CTH)(DTBSQ)]_2Cl(PF_6)_3$", was proposed based on elemental analysis by Dei.[28] Because the cationic unit of interest is unchanged, and the anion mixture stabilizes the complex, more intensive attempts to remove the Cl^- anion were deemed unnecessary.

It was predicted that [**2.1**]$^+$ − [**2.3**]$^+$ would be catecholate complexes while the oxidized [**2.3**]$^{2+}$ would be a semiquinonate complex. Structural parameters determined are consistent with such designation. The C−C bond lengths within a catechol ring should be nearly identical due to the aromaticity of the ring while the semiquinone species should display alternating bond lengths due to the localization of electrons in double bonds. Upon examining the crystallographic data for [**2.1**]$^+$, [**2.2**]$^+$, and [**2.3**]$^+$, it is evident that they are catecholate complexes. The cyclic C−C bond lengths are similar to one another, and all three complexes exhibit Cr−O bond lengths within the expected range of values for transition metal−catecholate complexes. On the contrary, [**2.3**]$^{2+}$ exhibits alternating C−C bond lengths, 1.36−1.45 Å, which is within the documented range for semiquinone species.[29] The intradiol C−O and C1−C2 bond distances can also distinguish between semiquinones (∼1.29 and ∼1.44 Å, respectively) and catecholates (∼1.35 and 1.39 Å, respectively), further supporting the assignment of [**2.1**]$^+$ − [**2.3**]$^+$ as catecholates and [**2.3**]$^{2+}$ as a semiquinonate.[30] Further supporting the delocalization of the SQ charge, the Cr−O1 and Cr−O2 bond lengths in [**2.3**]$^{2+}$ are identical with the experimental errors, and these bonds are slightly elongated from those in [**2.3**]$^+$. Sato and co-workers observed comparable Cr−O bond distances in the crystal structure of $[(Cr(CTH))(Co(CTH))(\mu\text{-dhbq})](PF_6)_3$ at 200 K (1.933 and 1.940 Å), where Cr^{III} is coordinated to a bridging semiquinonate ligand.[31] To compensate for the reduced donicity of SQ compared to CAT in [**2.3**]$^{2+}$, the nitrogen centers trans to SQ (N2 and N4) are about 0.045 Å closer to the Cr center than the other two nitrogens (N1 and N3).

2.3.3 Electrochemistry

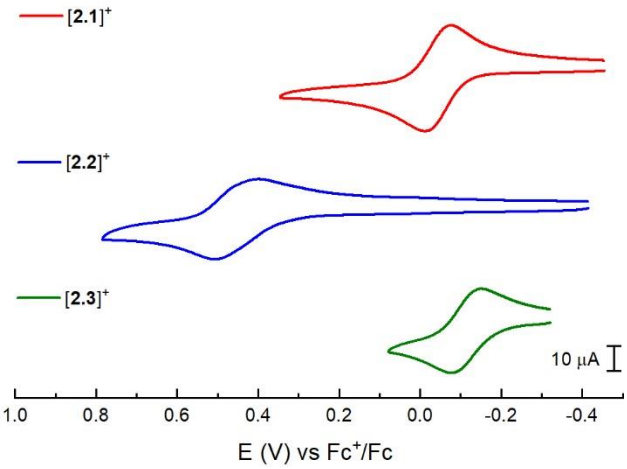

Figure 2.5. Cyclic voltammograms of [**2.1**]$^+$, [**2.2**]$^+$, and [**2.3**]$^+$ recorded at a 0.1 V/s scan rate in a 1.0 mM MeCN solution of 0.2 M *n*-Bu_4NPF_6.

Electrochemical measurements in MeCN indicate that all three complexes undergo a reversible one-electron oxidation. The anodic cyclic voltammograms are presented in Figure 2.5 while the redox potentials are given in Table 2.2. These redox events are ligand-centered, resulting from the conversion of catecholate to semiquinonate. The oxidations for [Cr(CTH)TCCat]PF_6 and [Cr(CTH)TBCat]Cl were previously reported at 0.84 and 0.21 V (vs SCE),[28] which are close to our reported values. Irreversible oxidations for the conversion of semiquinonate to quinonate were observed at 1.40 V (vs Fc^+/Fc) for [**2.1**]$^+$, 1.58 V for [**2.2**]$^+$, and 1.03 V for [**2.3**]$^+$ (Figure 2.S2). No chromium-based redox events occurred within the solvent window. The di-*tert*-butyl substituents have a marginal effect on the redox properties of the catecholate, shifting the redox potential of [**2.3**]$^+$ cathodically by 0.071 V with respect to that of [**2.1**]$^+$. On the contrary, the tetrachloro substitution has a profound effect, shifting the potential of [**2.2**]$^+$ by 0.46 V anodically from that of [**2.1**]$^+$.

Table 2.2. Electrochemical Potentials (V, vs Fc^+/Fc) for [**2.1**]$^+$ – [**2.3**]$^+$

	***E*(Cat/SQ)**	***E*(SQ/BQ)[a]**
[**2.1**]$^+$	−0.043	1.40
[**2.2**]$^+$	0.415	1.58
[**2.3**]$^+$	−0.114	1.03

[a]Irreversible couple; E_{pa} is reported.

2.3.4 UV-vis Spectroscopic Analysis

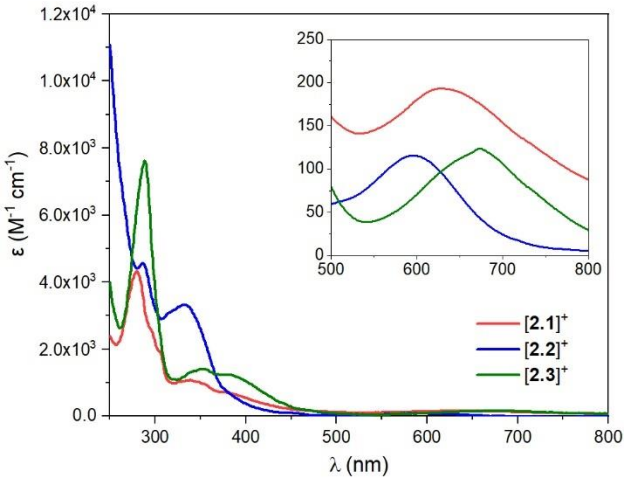

Figure 2.6. Absorption spectra of [**2.1**]$^+$, [**2.2**]$^+$, and [**2.3**]$^+$ in MeCN with d−d transitions magnified in the inset.

The UV-vis absorption spectra of [**2.1**]$^+$, [**2.2**]$^+$, and [**2.3**]$^+$ recorded in MeCN are shown in Figure 2.6. Spin-allowed d−d transitions occur between 500 and 800 nm, as highlighted in the inset. Compared to [**2.1**]$^+$ (λ_{max} at 629 nm), the λ_{max} of [**2.2**]$^+$ is blue-shifted to 596 nm, while that of [**2.3**]$^+$ is red-shifted to 678 nm. Because intraligand (n → π* and π → π*) transitions or charge-transfer (MLCT or LMCT) transitions are possible in the UV region, a solvent dependence study was conducted in MeOH, THF, and EtOAc in addition to MeCN (Figure 2.S3). While the molar absorptivity varied depending on the solvent, the λ_{max} values for the two transitions were nearly identical, ranging between 351−354 nm and 377−380 nm (Table 2.S2). This indicates that they are most likely intraligand in nature, although it should be noted that not all charge-transfer bands are solvatochromic.[32] The absorption spectra of [**2.3**]$^+$ and [**2.3**]$^{2+}$ recorded in MeCN are shown in Figure 7, while the spectral series of [**2.3**]$^+$ being oxidized to [**2.3**]$^{2+}$ while holding the potential at 0.43 V is provided in Figure 2.4. Spectral assignments for [**2.3**]$^{2+}$ were previously suggested by Dei and Benelli.[28] A prominent feature is the intense, sharp transition observed at 674 nm, which is attributed to a spin-forbidden transition of $^4A_2(Cr^{III}) \rightarrow {}^2E(SQ)$ parentage with an effective C_{2v} symmetry. This is due to strong exchange coupling between Cr^{III} and the SQ radical. Intense transitions observed at 469 and 440 nm have been previously assigned as MLCT in nature because of the observed red-shift in the presence of electron-withdrawing groups on the semiquinone ligand.[28] Intraligand transitions appear below 400 nm.

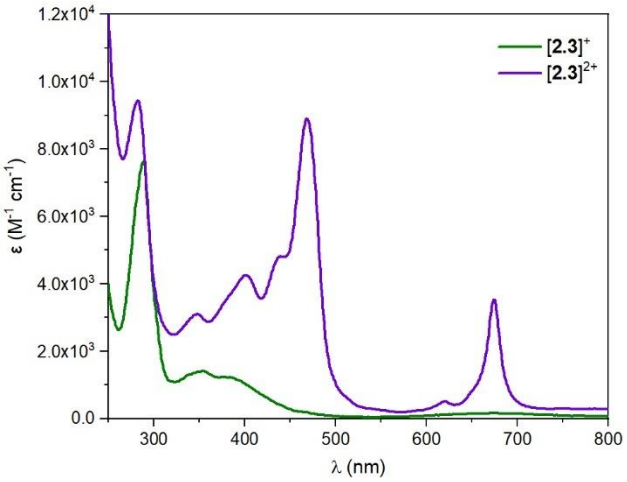

Figure 2.7. Absorption spectra of [**2.3**]$^{+}$ and [**2.3**]$^{2+}$ in MeCN.

2.3.5 Emission Studies

The emission spectra of [**2.1**]$^{+}$ − [**2.3**]$^{+}$ in 2-methyltetrahydrofuran glass at 77 K are shown in Figure 2.8, with phosphorescence lifetimes reported in Table 2.3. Because of low symmetry, the emissive state for Cr^{III} can sometimes be difficult to assign, and thus the lowest-energy state may not be of ^{2}E parentage. For example, Forster has documented that the energy of the $^{2}T_1$ state can drop below that of the ^{2}E state in the presence of a strongly tetragonal ligand field, as in the cases of *trans*-[Cr(cyclam)F_2]$^{+}$ and *trans*-[Cr(HMC)F_2]$^{+}$.[17] The ^{2}E emission spectra are typically narrow, while those of $^{2}T_1$ are broad. Nevertheless, spectral shape alone is insufficient to make a formal assignment.

All three catecholate complexes exhibit ^{2}E emission with a λ_{max} ranging between 720 and 730 nm. Although ^{2}E emission for Cr^{III} complexes typically occurs between 660 and 700 nm, it has been documented that the emission red-shifts upon increasing the number of N−H bonds directly bound to the metal center.[33] McCusker and co-workers reported ^{2}E emission of [Cr(tren)(DTBCat)]PF_6 (tren = tris(2-aminoethyl)amine) centered at 725 nm with a lifetime of 50 μs,[34] which is comparable to [**2.1**]$^{+}$ with a lifetime of 50 μs and [**2.3**]$^{+}$ with a lifetime of 57 μs. Other *cis*-[$Cr^{III}N_4X_2$]$^{+}$ type complexes have displayed similar phosphorescence lifetimes.[33]

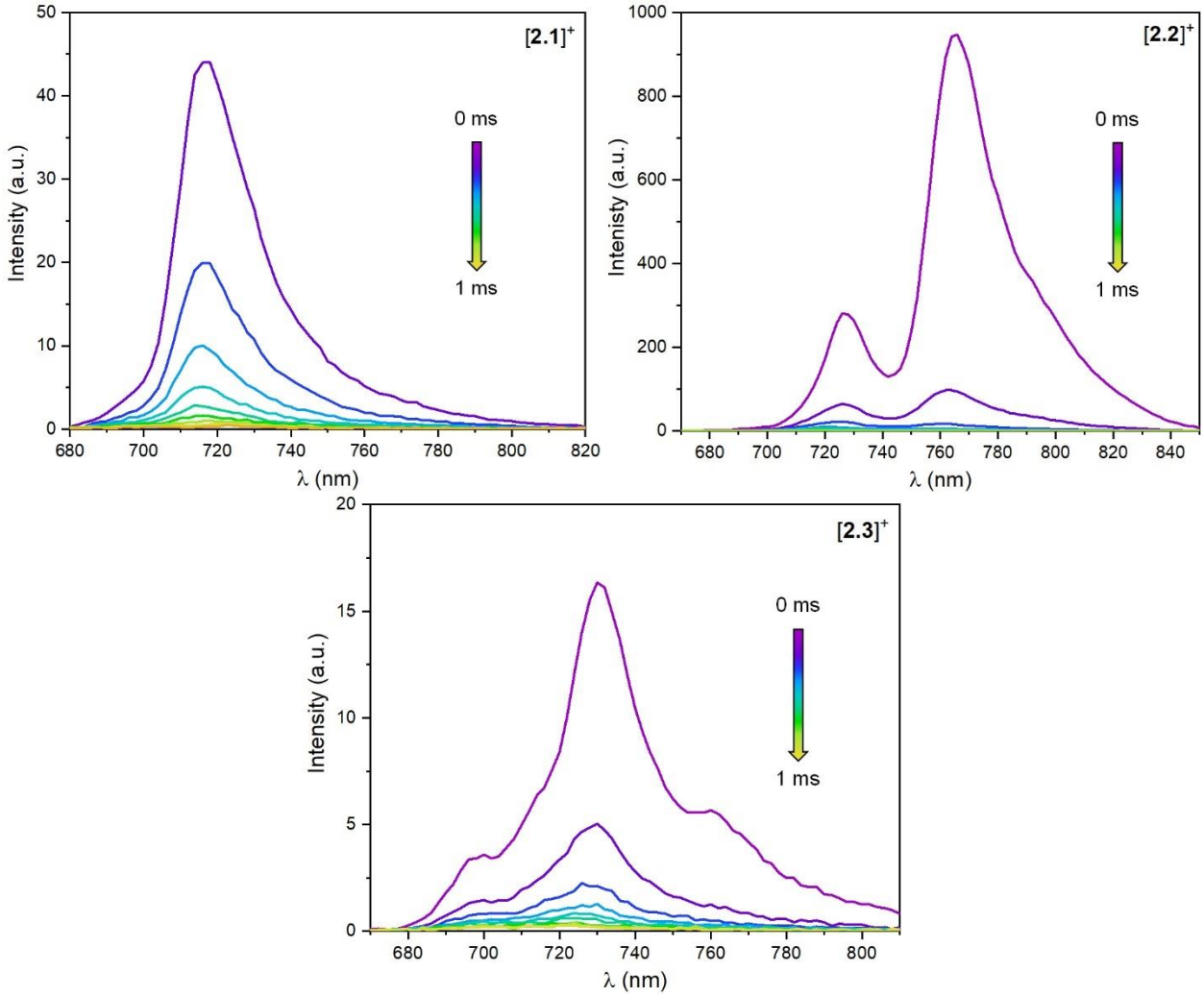

Figure 2.8. Time-delayed emission spectra of [**2.1**]$^+$, [**2.2**]$^+$, and [**2.3**]$^+$ at 77 K in 2-methyltetrahydrofuran at varying delay times.

Table 2.3. Photophysical Data for Complexes [**2.1**]$^+$, [**2.2**]$^+$, and [**2.3**]$^+$.

	$\tau(^2E)$ (μs)	$\tau(^2T_1)$ (μs)	λ_{ex} (nm)	λ_{max}(nm)
[**2.1**]$^+$	50		340	720
[**2.2**]$^+$	38	22	350	726, 762
[**2.3**]$^+$	57		340	730

The spectrum of [**2.2**]$^+$ is quite different from those of [**2.1**]$^+$ and [**2.3**]$^+$. While [**2.2**]$^+$ exhibits ^2E emission around the same wavelength as [**2.1**]$^+$ and [**2.3**]$^+$, an intense, but shorter lived emission from the $^2T_1$ state is also observed centered at 762 nm. Although the energy levels of doublet states, such as $^2T_1$, are not influenced by ligand field strength, they are impacted by the nephelauxetic effect.[17] The delocalization of electrons over the catecholate ligand and away from

the Cr^{III} center reduces repulsion and expands the electron cloud, resulting in lower energy emission. Revisiting the crystallographic data of [**2.1**]$^+$ − [**2.3**]$^+$, it is evident that [**2.2**]$^+$ possesses the longest Cr−O bond lengths of the series. The $^2T_1$ energy is lowered below the ^2E state, and dual emission is observed.

Phosphorescence was not observed for [**2.3**]$^{2+}$ at 77 K in 2-methyltetrahydrofuran between 600 and 800 nm, which is consistent with the absence of emission in [Cr(tren)3,6-DTBSQ](PF$_6$)$_2$ reported by McCusker.[34] If emission is present, it may be short-lived and not measurable on the time scale of our instrument.

2.3.6 Temperature-Dependent Magnetic Susceptibility

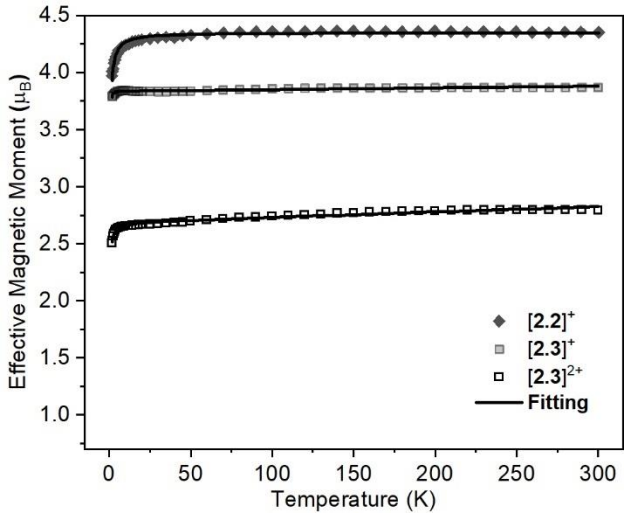

Figure 2.9. Temperature dependent magnetic susceptibility of catecholate complexes [**2.2**]$^+$, [**2.3**]$^+$, and semiquinonate complex [**2.3**]$^{2+}$ from 1.8–300 K. The solid lines represent the fitting results. Courtesy of Z.-B. Hu.

Magnetic susceptibility measurements can provide insight into the differences between electron-donating and -withdrawing groups on catecholate, in addition to the contrast in ground-state configurations between catecholate and semiquinone complexes. Effective magnetic moments for solid state samples of complexes [**2.2**]$^+$, [**2.3**]$^+$, and [**2.3**]$^{2+}$ between 1.8 and 300 K are shown in Figure 2.9. The observed magnetic moment for [**2.3**]$^+$ at 300 K is 3.88 μB, which is in excellent agreement with the expected value of 3.87 μB for a spin-only Cr^{III} ion (S = 3/2). However, [**2.2**]$^+$ has an effective magnetic moment of 4.35 μB at 300 K, which is higher than

expected. This could be due to a larger Landé factor caused by the spin−orbital coupling of Cr^{III} ion. The effective magnetic moment of [**2.3**]$^{2+}$ is expected to have a spin-only value of 2.83 μB, resulting from the very strong antiferromagnetic coupling of Cr^{III} (S = 3/2) and the semiquinone ligand (S = 1/2) to yield an S = 1 system. It is worth mentioning that instead of superexchange, the coupling in [**2.3**]$^{2+}$ is direct exchange in nature due to the proximity of SQ and Cr(III), which is similar to the case of N_2^{3-} radical-bridged terbium complex.[35] The observed magnetic moment of [**2.3**]$^{+}$ at 300 K is 2.79 μB, which is in good agreement with the spin only value. Dei reported an effective magnetic moment of 2.9 μB at room temperature for $[Cr(CTH)(3,5\text{-}DTBSQ)]_2(PF_6)_3Cl$, which is similar to our reported value. While the effective magnetic moments remain nearly constant between 25 and 300 K for all three complexes, small decreases are observed below 25 K, which are mainly ascribed to the zero-field splitting effect (see Section 2.6.5). Plots of $\chi_M T$ vs T and M vs H can be found in Figures 2.S5 and 2.S6.

2.3.7 Density Functional Theory (DFT) Calculations

To better understand the ground-state electronic structures of Cr^{III}(HMC) catecholate complexes, DFT calculations were performed on the monocationic complexes [**2.1**]$^{+}$ − [**2.3**]$^{+}$; frontier molecular orbitals (MOs) for all three are shown in Figure 2.10. In the quartet ground state, which has been verified by using magnetic susceptibility measurements, the three singly occupied MOs (SOMO, SOMO−1, and SOMO−2) belong to the near-degenerate set of d_{xy}, d_{yz}, and d_{xz} orbitals. The highest fully occupied orbital is almost exclusively catecholate based, with negligible contributions from Cr and the HMC ligand. The difference between [**2.2**]$^{+}$ and the other two complexes lies in the ordering of the lowest unoccupied orbitals LUMO−LUMO+2. In the cases of [**2.1**]$^{+}$ and [**2.3**]$^{+}$, the LUMO is a d_{z^2} orbital, which is ca. 0.4 eV lower than the predominantly catecholate-based LUMO+1. Reflecting the strong electron-withdrawing nature of four chloro substituents, the LUMO of [**2.2**]$^{+}$ is entirely catecholate-based, with a very closely spaced (ca. 0.02 eV) LUMO+1 of d_{z^2} character. In all three complexes, the presence of both the catecholate oxygens and the HMC nitrogens in the equatorial plane raises the energy of the $d_{x^2-y^2}$ over the d_{z^2} orbital to the LUMO+2 (not pictured). Considering that the occupied orbitals do not substantially differ among the three complexes, it is likely that the differences seen in the emission spectra of [**2.1**]$^{+}$/[**2.3**]$^{+}$ and [**2.2**]$^{+}$ (Figure 2.8) arise due to the differences in relative ordering of the unoccupied orbitals.

Furthermore, ground-state DFT calculations performed on the oxidized, dicationic complex [**2.3**]$^{2+}$ corroborate the antiferromagnetic coupling between the S = 3/2 Cr^{III} and S = 1/2 semiquinone ligand. Spin-density calculations place three unpaired electrons on Cr and one unpaired electron mainly delocalized over the O1, C1, C2, and O2 atoms (Figure 2.S8). In accordance with the radical anionic nature of the ligand, the experimentally observed alternating C−C/C=C bond lengths of the semiquinone ligand are faithfully reproduced by DFT (Table 2.S3).

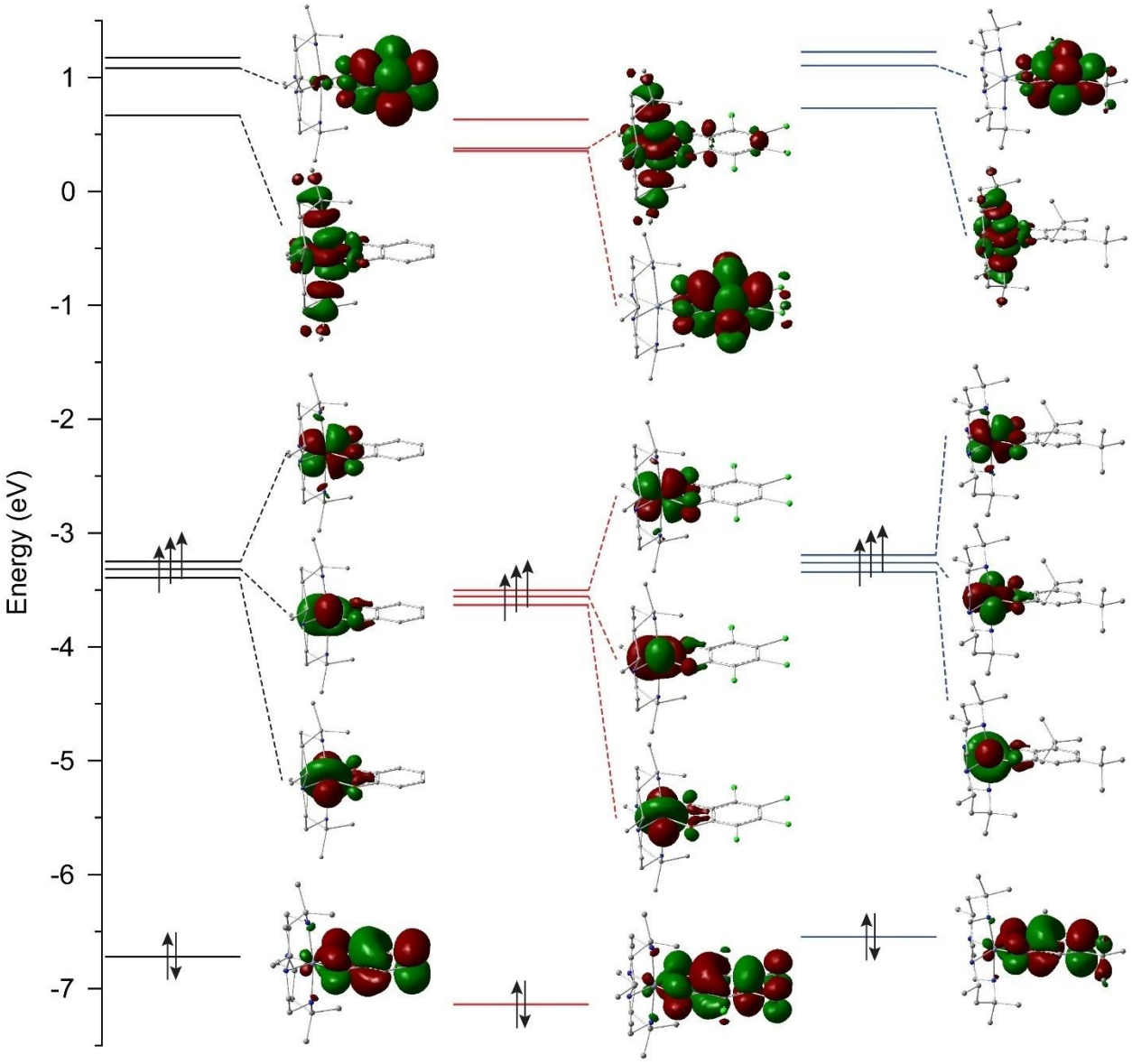

Figure 2.10. Frontier molecular orbitals of [**2.1**]$^{+}$ (left), [**2.2**]$^{+}$ (center) and [**2.3**]$^{+}$ (right) derived from DFT calculations. MOs are plotted at |isovalue| = 0.025. Courtesy of A. Raghavan.

2.4 Conclusion

Three Cr^{III}(HMC) complexes bearing catecholate ligands and one complex bearing a semiquinonate ligand were prepared and characterized. Bond lengths confirmed the oxidation state of the Cat/SQ ligands. Among the catecholate series, it is evident that the electron-donating groups in [**2.3**]$^+$ result in properties similar to [**2.1**]$^+$, while electron-withdrawing groups in [**2.2**]$^+$ result in significantly larger deviations from [**2.1**]$^+$. The most noteworthy differences with [**2.2**]$^+$ are that the reversible Cat/SQ oxidation is shifted by 0.458 V compared to [**2.1**]$^+$, and there is dual emission from the ^2E and $^2T_1$ states (instead of solely ^2E emission). Comparison of [**2.3**]$^+$ and [**2.3**]$^{2+}$ showed that the semiquinonate ligand displayed rich absorption spectra with a spin-forbidden transition. The magnetic susceptibility indicated there is strong antiferromagnetic coupling between the Cr(III) (S = 3/2) and SQ (S = 1/2) ligand in [**2.3**]$^{2+}$, resulting in an effective magnetic moment of 2.83 μB at 300 K, which closely aligns with the spin-only value expected for an S = 1 system.

2.5 Experimental Section

Materials. Catechol was purchased from Alfa Aesar, 3,5-di-*tert*-butylcatechol from ACROS Organics, mossy zinc from Mallinckrodt Chemical Works, and methanol from Fisher. HMC,[36] *cis*-[Cr(HMC)Cl_2]Cl,[37] and 3,4,5,6-tetrachlorocatechol[38] were prepared by using literature procedures. All reactions were performed in an open atmosphere.

Physical Measurements. UV−vis spectra were obtained with a JASCO V-670 spectrophotometer. ESI-MS were analyzed on an Advion mass spectrometer. Emission studies were performed on a Varian Cary Eclipse fluorescence spectrophotometer. Cyclic voltammograms were recorded in 0.2 M *n*-Bu_4NPF_6 solution (MeCN, N_2-degassed) on a CHI620A voltammetric analyzer with a glassy carbon working electrode, a Pt-wire auxiliary electrode, and an Ag/AgCl reference electrode with ferrocene used as an external reference. Spectrochemical analysis was performed by using an OTTLE (optically transparent thin-layer electrochemical) liquid-sample cell with a 0.2 mm optical path length, 0.3 mL sample volume, and a CaF_2 window procured from F. Hartl, Reading, UK. The cell was equipped with a mesh Pt working electrode, a mesh Pt auxiliary electrode, and an Ag reference electrode. The analyte concentration was 1.0 mM in 4 mL of dry MeCN at a 0.1 M *n*-Bu_4NPF_6 electrolyte concentration. The temperature-dependent

magnetic susceptibility was measured on a MPMS-XL7 SQUID magnetometer. Elemental analysis was performed by Atlantic Microlab, Inc. (Norcross, GA).

Synthesis of *cis*-[Cr(HMC)(catecholate)]Cl ([2.1]Cl). *cis*-[Cr(HMC)Cl_2]Cl (0.241 g, 0.545 mmol) and catechol (0.120 g, 1.09 mmol) were combined in 30 mL of methanol with ~0.5 g of mossy zinc. The reaction mixture was stirred and refluxed for 6 h. The crude reaction mixture was purified over a silica gel plug by using CH_2Cl_2, 1:1 CH_2Cl_2:MeCN, MeCN, 2:1 MeCN:MeOH, and MeOH. The product was recrystallized from CH_2Cl_2/Et_2O to give [**2.1**]Cl as a dark green solid (69% based on Cr). ESI-MS [M^+] 444 m/z, where [M^+] denotes the cationic species of [**2.1**]$^+$. Elem. Anal. Found (Calcd) for *cis*-[Cr(HMC)(catecholate)]Cl·1CH_2Cl_2: C, 48.60 (48.90); H, 7.66 (7.49); N, 9.53 (9.92). CV [$E_{1/2}$/V, ΔE_p/V, $i_{backward}/i_{forward}$]: Cat/SQ, −0.43, 0.063, 0.94; E_{pa} SQ/BQ, 1.40. UV−vis, λ_{max}/nm (ε/M^{-1} cm^{-1}): 629 (193), 370 (733), 340 (1080), 312 (sh), 293 (sh), 280 (4320).

Synthesis of *cis*-[Cr(HMC)(3,4,5,6-tetrachlorocatecholate)]Cl ([2.2]Cl). *cis*-[Cr(HMC)Cl_2]Cl (0.100 g, 0.226 mmol) and 3,4,5,6-tetrachlorocatechol (0.056 g, 0.226 mmol) were combined in 30 mL of methanol with ~0.5 g of mossy zinc. The reaction mixture was stirred and refluxed for 3 h. The crude reaction mixture was purified over a silica gel plug, and [**2.2**]Cl was eluted with 2:1 MeCN:MeOH. The product was a sky blue solid (62% based on Cr). Product was recrystallized with CH_2Cl_2/Et_2O. ESI-MS [M^+] 582 m/z, where [M^+] denotes the cationic species of [**2.2**]$^+$. Elem. Anal. Found (Calcd) for *cis*-[Cr(HMC)(3,4,5,6-tetrachlorocatecholate)]Cl·1.5CH_2Cl_2: C, 37.36 (37.88); H, 5.18 (5.27); N, 7.71 (7.52). CV [$E_{1/2}$/V, ΔE_p/V, $i_{backward}/i_{forward}$]: Cat/SQ, −0.415, 0.105, 0.93; E_{pa} SQ/BQ, 1.58. UV-vis, λ_{max}/nm (ε/M^{-1} cm^{-1}): 596 (117), 333 (3320), 286 (4570).

Synthesis of *cis*-[Cr(HMC)(3,5-di-*tert*-butylcatecholate)](PF_6) ([2.3]PF_6). *cis*-[Cr(HMC)Cl_2]Cl (0.500 g, 0.113 mmol) and 3,5-di-*tert*-butylcatechol (0.025 g, 0.114 mmol) were combined in 30 mL of methanol with ~0.5 g of mossy zinc. The reaction mixture was stirred and refluxed for 18 h. The crude reaction mixture was filtered, and solvent volume was reduced by using a rotary evaporator. A saturated aqueous solution of KPF_6 was added to the crude reaction mixture. The product was extracted with EtOAc. The solvent was removed, and the product was dissolved in THF. The product [**2.3**]PF_6 was obtained by adding hexanes to THF to yield a lime green solid (65% based on Cr). ESI-MS [M^+] 557 m/z, where [M^+] denotes the cationic species of [**2.3**]$^+$. Elem. Anal. Found (Calcd) for *cis*-[Cr(HMC)(3,5-di-*tert*-butylcatecholate)](PF_6): C, 50.93 (51.35); H, 8.13 (8.04); N 7.59 (7.98). CV [$E_{1/2}$/V, ΔE_p/V, $i_{backward}/i_{forward}$]: Cat/SQ, −0.114, 0.075,

0.95; E_{pa} SQ/BQ, 1.03. UV-vis, λ_{max}/nm (ε/M^{-1} cm^{-1}): 678 (167), 351 (1690), 372 (1430), 289 (8150).

Synthesis of [Cr(HMC)3,5-di-*tert*-butylsemiquinonate]$(PF_6)_{1.5}Cl_{0.5}$ ([2.3]$(PF_6)_{1.5}Cl_{0.5}$). Ferrocenium hexafluorophosphate (23.5 mg, 0.0711 mmol) was added to a solution of [**2.3**]PF_6 (0.050 g, 0.0711 mmol) in MeCN and was stirred for 30 min. The remaining $FcPF_6$ was filtered off. A jade green solid was precipitated out by adding hexanes to a solution of [**2.3**]$^{2+}$ in THF or CH_2Cl_2. The solid was washed with hexanes to remove any remaining ferrocene. The product was recrystallized with MeCN/Et_2O to result in a jade green solid (89% based on [**2.3**]PF_6). Elem. Anal. Found (Calcd) for *cis*-[Cr(HMC)(3,5-di-*tert*-butylsemiquinone)]$(PF_6)_{1.5}Cl_{0.5}\cdot 2CH_2Cl_2$: C, 40.26 (39.96); H, 6.43 (6.29); N, 5.88 (5.82). UV-vis, λ_{max}/nm (ε/M^{-1} cm^{-1}): 674 (3548), 652 (sh), 621 (515), 469 (8895), 440 (4810), 400 (4260), 348 (3100), 283 (9433).

X-ray Crystallographic Analysis. B. L. Mash collected and refined the crystallographic data of complexes [**2.1**]$^+$, [**2.2**]$^+$, and [**2.3**]$^+$. S. D. C. Banziger collected and refined the crystallographic data of complex [**2.3**]$^{2+}$. X-ray diffraction data for [**2.1**]Cl, [**2.2**]Cl, [**2.3**]PF_6, and [**2.3**]$(PF_6)_{1.5}Cl_{0.5}$ were collected at 150 K on a Bruker Quest diffractometer with Mo Kα radiation (λ = 0.71073 Å). Data were collected and processed by using APEX3 and reduced by using SAINT.[39] The structures were solved by using the SHELXTL suite of programs and refined by using Shelxl2016.[40-41] Details of data collection and structure refinement are provided in Table 2.S1.

Computational Details. All DFT calculations were performed by using Gaussian 16, Rev. A.03.[42] Geometry optimizations were performed on [**2.1**]$^+$, [**2.2**]$^+$, [**2.3**]$^+$, and [**2.3**]$^{2+}$ by using their respective X-ray structures as initial geometries. Minima were confirmed by using frequency analyses; no imaginary frequencies were found. Calculations were attempted by using multiple functionals. Data from emission spectra (phosphorescence) were used as a constraint for the minimum-energy difference between the quartet ground state and the doublet excited state. Based on this, the M06-2X functional[43] was found to perform satisfactorily for both complexes. The def2tzvp basis set was used for Cr and the def2svp basis set for all other atoms.[44] Dispersion forces were modeled by using Grimme's D3 empirical dispersion model.[45] All calculations were performed in acetonitrile as solvent described by using the polarizable continuum model (PCM).[46]

2.6 Supporting Information

2.6.1 Crystallographic Details

Single crystals of the investigated compounds were coated with a trace of Fomblin oil and were transferred to the goniometer head of a Bruker Quest diffractometer with a fixed chi angle, a Mo Kα wavelength (λ = 0.71073 Å) sealed tube fine focus X-ray tube, single crystal curved graphite incident beam monochromator, and a Photon100 area detector. The instrument was equipped with an Oxford Cryosystems low temperature device and examination and data collection were performed at 150 K. Data were collected, reflections were indexed and processed, and the files scaled and corrected for absorption using APEX3[39] and SADABS[47]. The space groups were assigned and the structures were solved by direct methods using XPREP within the SHELXTL suite of programs[40-41] and refined by full matrix least squares against F^2 with all reflections using Shelxl2018[48-49] using the graphical interface Shelxle.[50] Additional data collection and refinement details, including description of disorder (where present) can be found below. Complete crystallographic data, in CIF format, have been deposited with the Cambridge Crystallographic Data Centre. CCDC 2039087 – 2039090 contain the supplementary crystallographic data for this paper. These data can be obtained free of charge from The Cambridge Crystallographic Data Centre via www.ccdc.cam.ac.uk/data_request/cif.

Refinement details for [2.1]Cl. No disorder or other special details are present in this structure.

Refinement details for [2.2]Cl. A water molecule is present in the structure. Oxygen bound H atoms were located in difference density electron maps and restrained to ride their respective O atom. The H--O distances were restrained to 0.84(2) Å and the H...H distance was restrained to 1.36(2) Å. All carbon bound H atoms were placed in calculated positions and constrained to ride their respective carrier atoms. Each dichloromethane solvate molecule is located on a six-fold improper rotation axis. The molecule containing C23 is disordered over six symmetry equivalent positions but was not further disordered. The molecules containing C24 and C25 were also disordered over six symmetry equivalent positions with additional positional disorder with each other. All dichloromethane moieties were restrained to have similar geometries. The ADPs of atoms within 2.0 Å of each other were restrained to be similar. For all dichloromethane molecules, the Cl--C bond lengths were restrained to 1.77(2) Å and the Cl...Cl bond lengths were restrained

to 2.935(20) Å. Subject to these conditions, the occupancies for the C24 and C25 moieties refined to 0.0745(19) and 0.0922(19), respectively. These occupancies sum to 0.1667, or 1/6, which is accounted for by the six-fold symmetry disorder.

Refinement details for [2.3]PF_6. The C7 *tert*-butyl group is rotationally disordered. It was refined as three moieties. Each minor moiety (B and C) were restrained to be geometrically similar to the major (A) moiety. The U^{ij} components of the ADPs for all atoms within 2.0 Å were restrained to be similar. The sum of the occupancies for each moiety were constrained to be 1. Subject to these conditions, the occupancies for the A, B, and C moieties refined to 0.523(3), 0.321(3), and 0.157(3), respectively. The C37 benzene is located on an inversion center. It was constrained to resemble an ideal hexagon using AFIX 66 and the U^{ij} components of the ADPs for all atoms within 2.0 Å were restrained to be similar.

Refinement details for [2.3]$(PF_6)_{1.5}Cl_{0.5}$. A PF_6^- counterion is disordered in place over two alternative orientations. The moieties were restrained to have similar geometries. A SIMU command was used to restrain the atoms of the disordered PF_6^- counterion to have similar U^{ij} components of their ADPs. Subject to these conditions the occupancy ratio refined to 0.560(3) to 0.439(7). The fluorine atoms of a second PF_6^- counterion, located atop an inversion center, were refined as disordered. The disordered PF_3 units were restrained to have similar geometries. A SIMU command was used to restrain the rotated PF_6^- counterions to have similar U^{ij} components of ADPs. Subject to these conditions the occupancy ratio refined to 0.415(2) to 0.594(8).

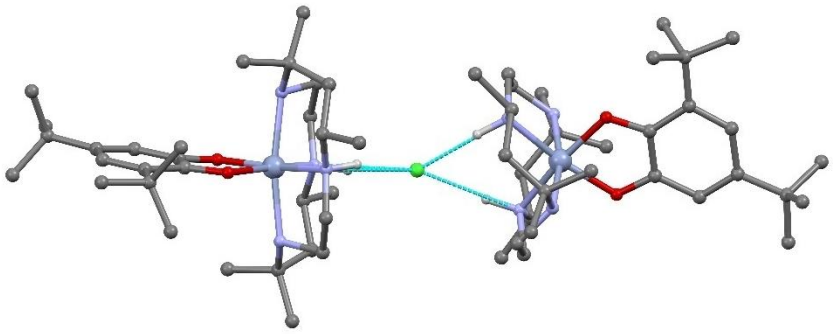

Figure 2.S1. Hydrogen bonding of two [**2.3**]$^{2+}$ cations shown between the Cl^- counteranion and N2–H or N4–H. Other hydrogen atoms and PF_6^- counteranions omitted for clarity.

Table 2.S1. Experimental Details for [**2.1**]Cl, [**2.2**]Cl, [**2.3**]PF_6, and [**2.3**]$(PF_6)_{1.5}Cl_{0.5}$.

Identification code	[**2.1**]Cl	[**2.2**]Cl	[**2.3**]PF_6	[**2.3**]$(PF_6)_{1.5}Cl_{0.5}$
Chemical formula	$C_{22}H_{40}CrN_4O_2\cdot Cl\cdot H_2O$	$C_{22}H_{36}Cl_4CrN_4O_2\cdot 0.333(CH_2Cl_2)\cdot Cl\cdot H_2O$	$C_{30}H_{56}CrN_4O_2\cdot F_6P\cdot 1.5(C_6H_6)$	$2(C_{30}H_{56}CrN_4O_2)\cdot 3(F_6P)\cdot Cl$
Formula weight	498.04	664.12	818.92	1583.93
Temperature/K	150	150	150	150
Crystal system	Orthorhombic	Trigonal	Monoclinic	Monoclinic
Space group	*Pcba*	*R*-3	$P2_1/c$	$C2/c$
a (Å)	16.1043 (12)	24.7614 (11)	22.1973 (8)	23.4506 (17)
b (Å)	9.8190 (7)	24.7614 (11)	9.6379 (3)	15.4226 (12)
c (Å)	31.902 (2)	25.7423 (11)	20.1954 (7)	22.3984 (19)
α (°)	90	90	90	90
β (°)	90	90	96.9617 (15)	110.380 (3)
γ (°)	90	120	90	90
V ($Å^3$)	5044.6 (6)	13668.7 (13)	4288.7 (3)	7593.7 (10)
Z	8	18	4	4
ρ_{calc} (g/cm^3)	1.312	1.452	1.268	1.385
μ (mm^{-1})	0.59	0.91	0.367	0.48
F(000)	2136	6210	1744	0.476
Crystal size (mm)	0.30 × 0.24 × 0.13	0.46 × 0.42 × 0.20	0.55 × 0.41 × 0.05	0.46 × 0.17 × 0.11
Radiation	MoKα (λ = 0.71073)			
Diffractometer	Bruker AXS D8 Quest CMOS diffractometer			
Absorption correction	Multi-scan. *SADABS* 2016/2: Krause, L., Herbst-Irmer, R., Sheldrick G.M. & Stalke D., J. Appl. Cryst. 48 (2015) 3-10			
T_{min}, T_{max}	0.631, 0.746	0.689, 0.747	0.649, 0.747	0.697, 0.747
θ_{min}, θ_{max} (°)	3.094, 28.220	3.305, 33.210	2.932, 33.170	2.261, 35.713
Index ranges	-21 < h < 19, -8 < k < 13, -41 < l < 41	-29 < h < 38, -38 < k < 37, -38 < l < 39	-27 < h < 34, -14 < k < 13, -30 < l < 28	-38 < h < 38, -25 < k < 25, -36 < l < 31
Meas., ind. and obs. [$I > 2\sigma(I)$] reflections	21240, 6166, 4766	101779, 11603, 9269	59843, 15924, 11622	164206, 17595, 12592
R_{int}	0.032	0.028	0.044	0.062
$(\sin\theta/l)_{max}$ ($Å^{-1}$)	0.665	0.771	0.770	0.821
Data, parameters, restraints	6166, 292, 2	11603, 412, 79	15924, 586, 325	17595, 539, 780
$R[F^2 > 2\sigma(F^2)]$, $wR(F^2)$, S	0.045, 0.113, 1.06	0.044, 0.122, 1.08	0.050, 0.141, 1.04	0.821
$\Delta\rangle_{max}$, $\Delta\rangle_{min}$ (e $Å^{-3}$)	0.43, -0.67	0.52, -0.67	0.79, -0.79	1.91, -0.74

2.6.2 Electrochemical Details

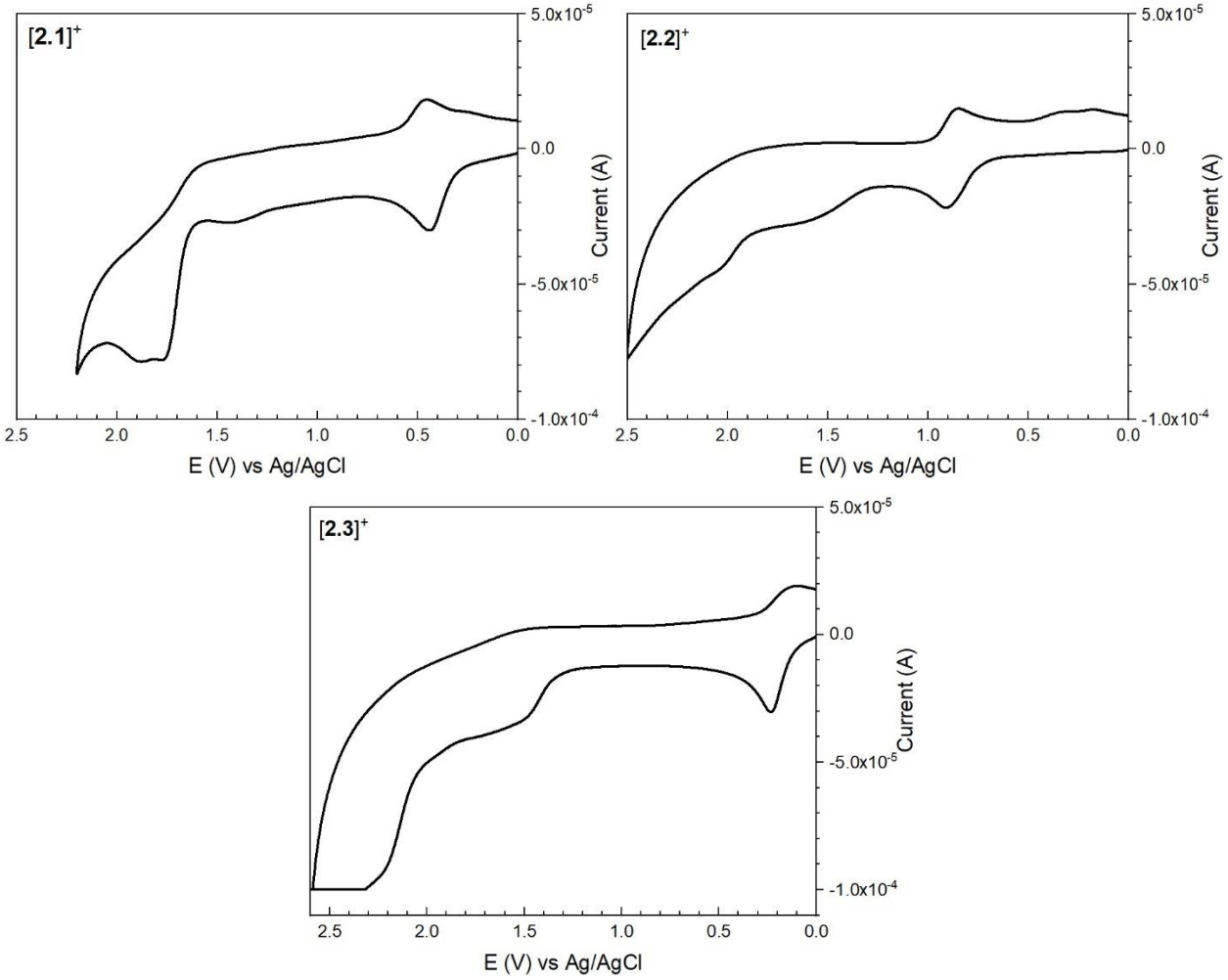

Figure 2.S2. Cyclic voltammograms of [**2.1**]$^+$, [**2.2**]$^+$, and [**2.3**]$^+$ at a scan rate of 0.1 V/s in a 0.1 M MeCN solution of 0.2 M *n*-Bu_4NPF_6.

2.6.3 Absorption Details

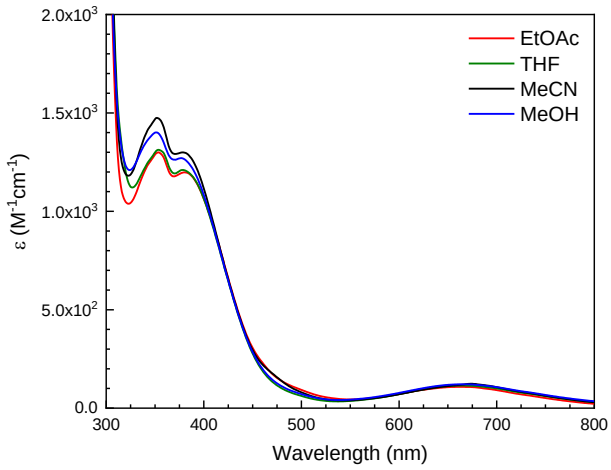

Figure 2.S3. Absorption spectra of [**2.3**]$^{+}$ in THF, EtOAc, MeCN, and MeOH.

Table 2.S2. Absorption data of [**2.3**]$^{+}$ in solvents of varying polarity.

Solvent	**λ_{max} (ε, $M^{-1}cm^{-1}$)**
EtOAc	353 (1300), 380 (1290), 663 (110)
THF	354 (1310), 378 (1210), 664 (114)
MeCN	352 (1480), 378 (1300), 667 (121)
MeOH	351 (1400), 377 (1270), 666 (121)

2.6.4 Spectroelectrochemical Characterization of [2.3]$^{1+/2+}$

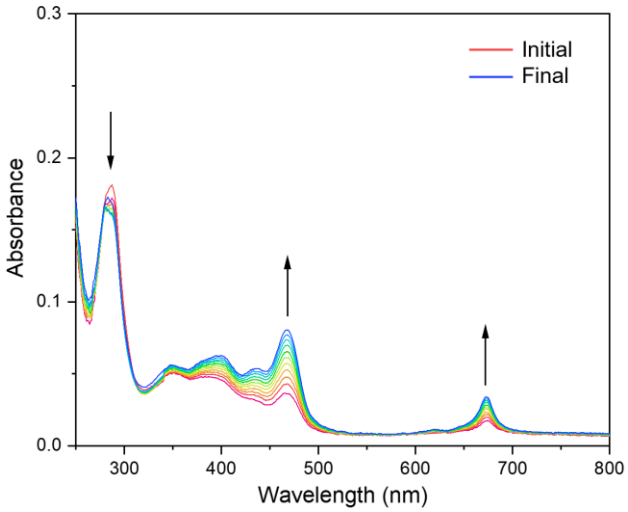

Figure 2.S4. Spectroelectrochemistry of [**2.3**]$^{+}$ in MeCN with (n-Bu)$_4$NPF$_6$ electrolyte.

Spectroelectrochemistry (SEC) was carried out to elucidate whether the observed single electron oxidation is ligand-centered as previously assigned or if Cr(III) is involved in the redox process. Compound [**2.3**]$^{+}$ was selected because it has the lowest redox potential of the series, therefore it is the easiest to oxidize chemically and electrochemically. Figure 2.S3 shows as [**2.3**]$^{+}$ is held at a potential of 0.41 V, rich features arise between 300-500 nm and 675 nm. This is due to an irreversible oxidation of [**2.3**]$^{+}$ to [**2.3**]$^{2+}$. The sharp features in the spectra of [**2.3**]$^{2+}$ are nearly identical to Benelli's [Cr(CTH)(DTBSQ)]$_2$Cl(PF$_6$)$_3$[28] and our spectra of [**2.3**]$^{2+}$ reported in Figure 2.7. No changes in the absorption spectra were observed after the potential was no longer applied, indicating [**2.3**]$^{2+}$ is stable under these conditions.

2.6.5 Temperature Dependent Magnetic Susceptibility

Static direct current (DC) magnetic measurements were performed on polycrystalline samples of [**2.2**]$^{+}$, [**2.3**]$^{+}$ and [**2.3**]$^{2+}$ in the 1.8-300 K temperature range under 1 kOe. As shown in Figure 2.S5, the $\chi_M T$ value at 300 K for [**2.2**]$^{+}$ is 2.37 cm^3 K mol^{-1}, larger than the expected value of 1.875 cm^3 mol^{-1} K for an isolated high spin Cr(III) (S = 3/2 and g = 2.0). With the decreasing temperature, the $\chi_M T$ values first smoothly decrease from room temperature to 50 K, then show a more pronounced decrease, finally reach an ultimate value of 1.97 cm^3 K mol^{-1} at 1.8 K. The field-dependence magnetizations of [**2.2**]$^{+}$ were measured in the fields ranging from 0 to 7 T between

1.8 and 10.0 K (Figure 2.S6). The magnetization at 7 T is also larger than the theoretically saturated value 3 $N\mu_B$. It is suggested that the ground state spin couples with the excited orbitals leading to a larger Landé factor. The magnetic susceptibility of [**2.2**]$^+$ was fitted via *PHI* program[7] to quantify the magnetic parameters using the following spin Hamiltonian (Equation 2.S1):

$$\hat{\mathbf{H}} = D\left[\hat{\mathbf{S}}_z^2 - \frac{S(S+1)}{3}\right] + g\mu_B\hat{\mathbf{S}}H \qquad \text{(Eq. 2.S1)}$$

where D is the axial zero-filed splitting (ZFS) parameter and $\hat{\mathbf{S}}$ is the spin operator. The best fits of the reduced magnetization data gave D = 4.0 × 10^{-5} cm^{-1}, zj = −0.049 cm^{-1}, g = 2.24(1) for [**2.2**]$^+$, where zj is the intermolecular interaction.

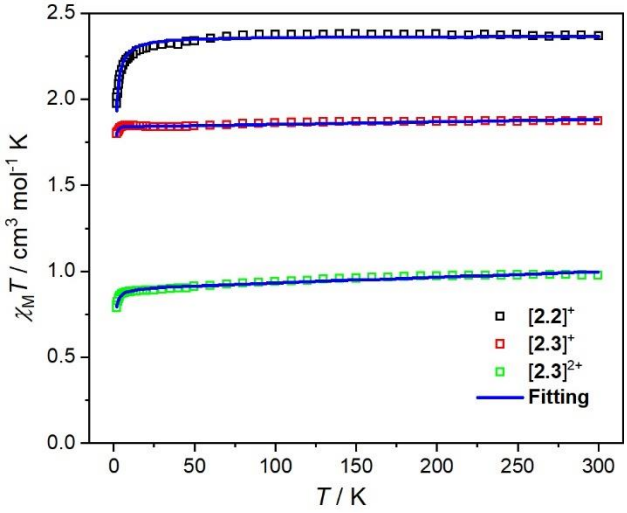

Figure 2.S5. Temperature dependence of $\chi_M T$ under a 1 kOe applied DC field at 1.8–300 K for a polycrystalline sample of complex [**2.2**]$^+$, [**2.3**]$^+$, and [**2.3**]$^{2+}$ by MPMS-XL7 SQUID. The solid lines represent the best fitting result by *PHI*.

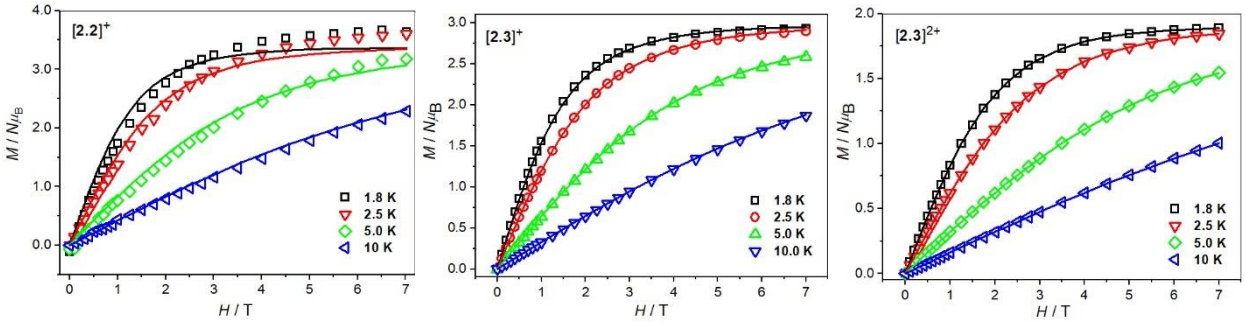

Figure 2.S6. Experimental M vs. H plots at different temperatures for [**2.2**]$^+$, [**2.3**]$^+$, and [**2.3**]$^{2+}$.

For [**2.3**]$^{+}$, the $\chi_M T$ value at 300 K of 1.873 cm^3 mol^{-1} K is very close to the spin-only value of 1.875 cm^3 mol^{-1} K for an isolated high spin Cr(III) (assuming S = 3/2 and g = 2.0). With cooling, $\chi_M T$ almost remains a constant from room temperature to 7 K, and slightly decreases below 7 K, finally reaches ultimate value of 1.80 cm^3 mol^{-1} K at 1.8 K. The field-dependence of the magnetization for [**2.3**]$^{+}$ shows the maximum value being 2.93 $N\mu_B$ at 70 kOe (Figure 2.S5), corresponding to the ground state of S = 3/2. The temperature and field dependent magnetization data of [**2.3**]$^{+}$ were fitted using the *PHI* program to quantify the magnetic parameters by equation (1).[7] The best fits of the reduced magnetization data gave D = −0.666(8) cm^{-1}, zj = 0.0027(2) cm^{-1}, g = 1.98(1) and *TIP* = 1.50 × 10^{-4}.

In [**2.3**]$^{2+}$, a radical couples with Cr(III) ion, but the $\chi_M T$ values are much less than those of [**2.2**]$^{+}$ and [**2.3**]$^{+}$ (Figure 2.S4). The $\chi_M T$ value at 300 K of 0.98 cm^3 mol^{-1} K is far less than the spin-only value of 2.15 cm^3 mol^{-1} K for an isolated high spin Cr(III) (assuming S = 3/2 and g = 2.0) and an free radical (S = 1/2 and g = 2.0) and very close to the theoretical value for S = 1, so it is suggested that a very strong antiferromagnetic coupling between spins further causing an ground state of S = 1 in [**2.3**]$^{+}$. With cooling, the $\chi_M T$ values first gradually decrease from room temperature to 7 K, then show a more pronounced decrease, finally reaching 0.79 cm^3 mol^{-1} K at 1.8 K. The field-dependence of the magnetization shows the maximum magnetization is 1.89 Nμ_B at 70 kOe, consistent with the ground state of S = 1. The temperature and field dependent magnetization data of [**2.3**]$^{2+}$ were fitted using the *PHI* program[7] based on the following spin Hamiltonian.

$$\widehat{\mathbf{H}} = -2J\hat{\mathbf{S}}_{Cr}\hat{\mathbf{S}}_r + D\left[\hat{\mathbf{S}}_z^2 - \frac{S(S+1)}{3}\right] + g\mu_B\hat{\mathbf{S}}H \qquad \text{(Eq. 2.S2)}$$

Equation 2.S2 gave the best fitting results: J = −867.94 cm^{-1}, zj = −0.0722(2) cm^{-1}, g = 1.90(1) and *TIP* = 3.05 × 10^{-4}. The J value indicates the very strong coupling between Cr(III) ion and radical. It is believed that this kind of coupling should belong to direct exchange rather than superexchange due to the radical electron delocalization in ligand.

2.6.6 Computational Details

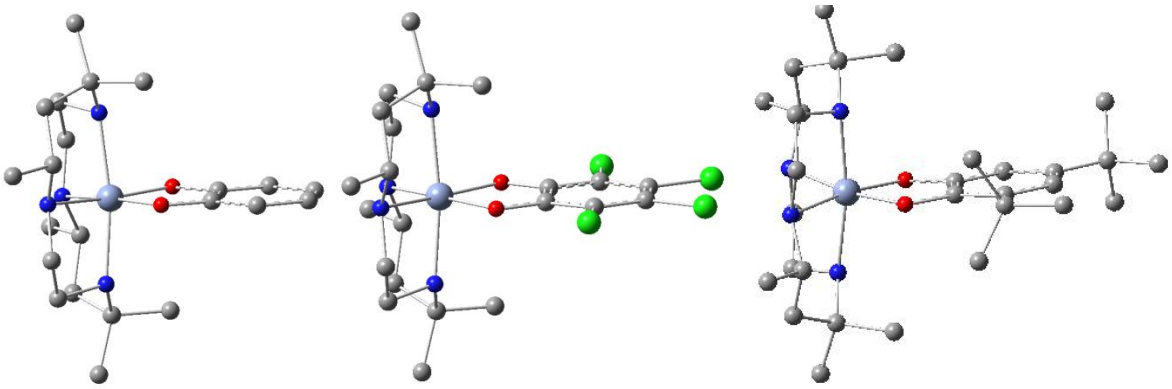

Figure 2.S7. DFT-optimized structures of [**2.1**]$^{+}$ (left), [**2.2**]$^{+}$ (center) and [**2.3**]$^{+}$ (right).

Table 2.S3. Selected DFT-optimized metrical parameters of [**2.1**]$^{+}$, [**2.2**]$^{+}$, [**2.3**]$^{+}$ and [**2.3**]$^{2+}$.

	[2.1]$^{+}$	**[2.2]$^{+}$**	**[2.3]$^{+}$**	**[2.3]$^{2+}$**
Cr–N$_{eq.}$ (avg.)	2.14282	2.132465	2.14746	2.116185
Cr–N$_{ax.}$ (avg.)	2.146695	2.14062	2.14811	2.137185
Cr–O (avg.)	1.928865	1.94100	1.92198	1.95809
C–O (avg.)	1.34323	1.32410	1.34661	1.29158
O–Cr–O	84.74351	83.86241	84.47003	80.39927
N$_{eq.}$–Cr–N$_{eq.}$	99.75322	101.522	100.55489	101.49519
N$_{ax.}$–Cr–N$_{ax.}$	169.91461	171.57844	170.24084	171.48250
C1–C2	1.42242	1.42328	1.42182	1.45876
C2–C3	1.39374	1.39400	1.38983	1.40961
C3–C4	1.40312	1.40768	1.40599	1.37805
C4–C5	1.39239	1.39526	1.39644	1.44346
C5–C6	1.40321	1.40768	1.41169	1.37570
C6–C1	1.39365	1.39400	1.40306	1.43251

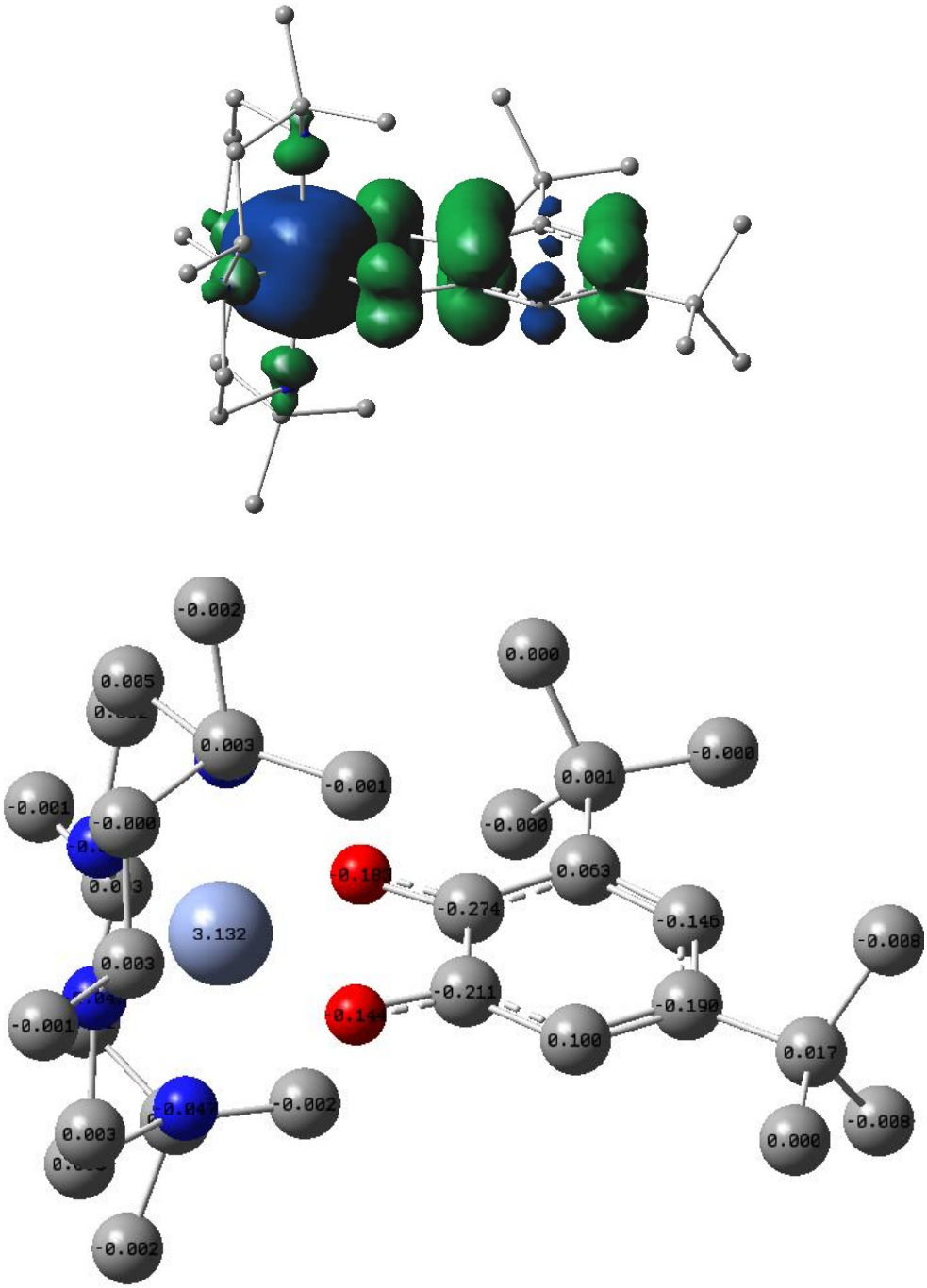

Figure 2.S8. Mulliken spin density plot of [**2.3**]$^{2+}$ at |isovalue| = 0.004 (top) and corresponding Mulliken spin population (bottom).

2.7 References

1. D. L. J. Broere, R. Plessius, J. I. van der Vlugt, *Chem. Soc. Rev.*, 2015, **44**, 6886–6915
2. P. J. Chirik, K. Weighardt, *Science,* 2010, **327**, 794–795
3. C. G. Pierpont and C. W. Lange, *Prog. Inorg. Chem.*, 1994, **41**, 331–442
4. W. Kaim, *Inorg. Chem.* 2011, **50**, 9752–9765
5. C. G. Pierpont and J. K. Kelly, in PATAI'S Chemistry of Functional Groups, John Wiley & Sons, Ltd, 2013.
6. W. Kaim and B. Schwederski, *Coord. Chem. Rev.,* 2010, **254**, 1580–1588
7. P. Kumar, S. V. Lindeman and A. T. Fiedler, *J. Am. Chem. Soc.,* 2019, **141**, 10984–10987
8. S. Sahu, and D. P. Goldberg, *J. Am. Chem. Soc.,* 2016, **138**, 11410–11428
9. M. M. Bittner, S. V. Lindeman and A. T. Fiedler, *J. Am. Chem., Soc.* 2012, **134**, 5460–5463
10. P. Gütlich, and A. Dei, *Angew. Chem. Int. Ed.,* 1997, **36**, 2734–2736
11. T. Tezgerevska, K. G. Alley and C. Boskovic, *Coord. Chem. Rev.*, 2014, **267**, 23–40
12. S. Kitagawa and S. Kawata, *Coord. Chem. Rev.,* 2002, **224**, 11–34
13. S. Demir, I. R. Jeon, J. R. Long and T. D. Harris, *Coord. Chem. Rev.,* 2015, **289**, 149–176
14. J. A. DeGayner, I. R. Jeon, L. Sun, M. Dinca, T. D. Harris, *J. Am. Chem. Soc.,* 2017, **139**, 4175–4184
15. L. J. Liu, L. Li, J. A. DeGayner, P. H. Winegar, Y. Fang and T. D. Harris, *J. Am. Chem. Soc.,* 2018, **140**, 11444–11453
16. A. D. Kirk, *Chem. Rev.,* 1999, **99**, 1607–1640
17. L. S. Forster, *Chem. Rev.,* 1990, **90**, 331–353
18. N. A. P. Kane-Maguire Photochemistry and Photophysics of Coordination Compounds: Chromium, *Photochemistry and Photophysics of Coordination Compounds I*, V. Balzani and S. Campagna, Springer, Berlin, Heidelberg, 2007
19. Y. Pei, Y. Journaux, O. Kahn, A. Dei and D. A. Gatteschi, *J. Chem. Soc., Chem. Commun.,* 1986, **16**, 1300–1301
20. A. Dei, D. Gatteschi, L. Pardi and U. Russo, *Inorg. Chem.*, 1991, **30**, 2589–2594

21. A. Dei, D. Gatteschi and L. Pardi, *Inorg. Chem.*, 1993, **32**, 1389–1395

22. C. Benelli, A. Dei, D. Gatteschi and L. Pardi, *Inorg. Chim. Acta*, 1989, **163**, 99–104

23. A. Caneschi, A. Dei, F. F. de Biani, P. Gutlich, V. Ksenofontov, G. Levchenko, A. Hoefer and F. Renz, *Chem. Eur. J.*, 2001, **7**, 3926–3930

24. C. Benelli, A. Dei, D. Gatteschi and L. Pardi, *Inorg. Chem.*, 1988, **27**, 2831–2836

25. A. Dei and L. Pardi, *Inorg. Chim. Acta*, 1991, **181**, 3–5

26. A. Dei, D. Gatteschi and L. Pardi, *Inorg. Chim. Acta*, 1991, **189**, 125–128

27. A. Bencini, C. Carbonera, A. Dei and M. G. F. Vaz, *Dalton Trans.*, 2003, **9**, 1701–1706

28. C. Benelli, A. Dei, D. Gatteschi, H. U. Gudel and L. Pardi, *Inorg. Chem.*, 1989, **28**, 3089–3091

29. S. N. Brown, *Inorg. Chem.*, 2012, **51**, 1251–1260

30. P. Zanello and M. Corsini, *Coord. Chem. Rev.*, 2006, **250**, 2000–2022

31. S. Kanegawa, Y. Shiota, S. Kang, K. Takahashi, H. Okajima, A. Sakamoto, T. Iwata, H. Kandori, K. Yoshizawa and O. Sato, *J. Am. Chem. Soc.*, 2016, **138**, 14170–14173.

32. A. B. P. Lever, *Inorganic Electronic Spectroscopy*, 2nd ed., Elsevier, Amsterdam, 1984

33. L. S. Forster and O. Moensted, *J. Phys. Chem.*, 1986, **90**, 5131–5134

34. D. E. Wheeler and J. K. McCusker, *Inorg. Chem.*, 1998, **37**, 2296–2307

35. J. D. Rinehart, M. Fang, W. J. Evans and J. R. Long, *J. Am. Chem. Soc.*, 2011, **133**, 14236–14239

36. R. W. Hay, G. A. Lawrance and N. F. Curtis, *J. Chem. Soc., Perkin Trans.*, 1975, **1**, 591–593

37. D. A. House, R. W. Hay and M. A. Ali, *Inorg. Chim. Acta*, 1983, **72**, 239–245

38. H. Lubbecke and P. Boldt, *Tetrahedron*, 1978, **34,** 1577–1579

39. Bruker (2016). Apex3 v2016.9-0, SAINT V8.34A, SAINT V8.37A, Bruker AXS Inc.: Madison (WI), USA, 2013/2014. **2016**.

40. SHELXTL suite of programs Version 6.14. Bruker Advanced X-ray Solutions. Bruker AXS Inc. 2000-2003, Madison, Wisconsin: USA.

41. G. M. Sheldrick, *Acta Cryst. A*, 2008, **64,** 112–122

42. M. J. Frisch, G. W. Trucks, H. B. Schlegel, G. E. Scuseria, M. A. Robb, J. R. Cheeseman, G. Scalmani, V. Barone, G. A. Petersson, H. Nakatsuji, X. Li, M. Caricato, A. V. Marenich, J. Bloino, B. G. Janesko, R. Gomperts, B. Mennucci, H. P. Hratchian, J. V. Ortiz, A. F. Izmaylov, J. L. Sonnenberg, D. Williams-Young, F. Ding, F. Lipparini, F. Egidi, J. Goings, B. Peng, A. Petrone, T. Henderson, D. Ranasinghe, V. G. Zakrzewski, J. Gao, N. Rega, G. Zheng, W. Liang, M. Hada, M. Ehara, K. Toyota, R. Fukuda, J. Hasegawa, M. Ishida, T. Nakajima, Y. Honda, O. Kitao, H. Nakai, T. Vreven, K. Throssell, J. J. A. Montgomery, J. E. Peralta, F. Ogliaro, M. J. Bearpark, J. J. Heyd, E. N. Brothers, K. N. Kudin, V. N. Staroverov, T. A. Keith, R. Kobayashi, J. Normand, K. Raghavachari, A. P. Rendell, J. C. Burant, S. S. Iyengar, J. Tomasi, M. Cossi, J. M. Millam, M. Klene, C. Adamo, R. Cammi, J. W. Ochterski, R. L. Martin, K. Morokuma, O. Farkas, J. B. Foresman and D. J. Fox, *Gaussian 16 Rev. A.03*.

43. Y. Zhao and D. G. Truhlar, *Theor. Chem. Acc.*, 2008, **120**, 215–241

44. F. Weigend and R. Ahlrichs, *Phys. Chem. Chem. Phys.*, 2005, **7**, 3297–3305

45. S. Grimme, J. Antony, S. Ehrlich and H. Krieg, *J. Chem. Phys., 2010*, **132**, 154104

46. M. Cossi, N. Rega, G. Scalmani and V. Barone, *J. Comput. Chem.*, 2003, **24**, 669–681

47. L. Krause, R. Herbst-Irmer, G. M. Sheldrick and D. Stalke, *J. Appl. Cryst.*, 2015, **48**, 3–10

48. G. M. Sheldrick, University of Göttingen, Germany, 2018

49. G. M. Sheldrick, *Acta Cryst. Sect C Struct Chem.*, 2015, **71**, 3–8

50. C. B. Hübschle, G. M. Sheldrick and B. Dittrich, *J. Appl. Crystallogr.*, 2011, **44**, 1281–1284

51. N. F. Chilton, R. P. Anderson, L. Turner, D. A. Soncini and K. S. Murray, *J. Computational Chem.*, 2013, **34**, 1164–1175

CHAPTER 3. A UNIQUE SERIES OF CHROMIUM(III) MONO-ALKYNYL COMPLEXES SUPPORTED BY TETRAAZAMACROCYCLES

Reprinted (adapted) with permission from A. J. Schuman, S. F. T. Robey, E. C. Judkins, M. Zeller and T. Ren, *Dalton Trans.*, 2021, **50**, 4936–4943. Copyright 2021, Royal Society of Chemistry. DOI: 10.1039/D1DT00707F

3.1 Abstract

Described herein is the synthesis and characterization of macrocyclic Cr^{III} mono-alkynyl complexes. By using the *meso*-form of the tetraazamacrocycle HMC (HMC = 5,5,7,12,12,14-hexamethyl-1,4,8,11-tetraazacyclotetradecane), *trans*-[Cr(HMC)(C_2Ph)Cl]OTf (**3.1a**), *trans*-[Cr(HMC)(C_2Np)Cl]OTf (**3.2a**), *trans*-[Cr(HMC)($C_2C_6H_4{}^t$Bu)Cl]OTf (**3.3a**), and *trans*-[Cr(HMC)(C_2(3,5-$Cl_2C_6H_3$))Cl]OTf (**3.4a**) complexes have been realized. These complexes were synthesized in high yield through the reaction of *trans*-[Cr(*meso*-HMC)(C_2Ar)$_2$]OTf (**3.1b** – **3.4b**) with stoichiometric amounts of methanolic HCl. Single crystal X-ray diffraction showed that the *trans*-stereochemistry and pseudo-octahedral geometry is retained in the desired mono-alkynyl complexes. The absorption spectra of complexes **3.1a** – **3.4a** display d–d bands with distinct vibronic progressions that are slightly red shifted from *trans*-[Cr(HMC)(C_2Ar)$_2$]$^+$ with approximately halved molar extinction coefficients. Time-delayed measurements of the emission spectra for complexes **3.1a** – **3.4a** at 77 K revealed phosphorescence with lifetimes ranging between 343 μs (**3.4a**) and 397 μs (**3.1a**). The phosphorescence spectra of **3.1a** – **3.4a** also exhibit more structuring than the bis-alkynyl complexes due to a strengthened vibronic coupling between the Cr^{III} metal center and alkynyl ligands.

3.2 Introduction

Transition-metal alkynyl chemistry is a fascinating topic in the realms of both synthesis and materials applications.[1-3] Weinstein and co-workers have garnered attention for the study of donor–bridge–acceptor (D–B–A) complexes utilizing a *trans*-Pt^{II}-bis-alkynyl bridge, and demonstrated that the evolution of photoinduced electron transfer (PET) excited states, especially the formation of the charge-separated (CS) state, can be attenuated by vibrational excitation of the Pt bound C≡C bonds.[4] Expanding this chemistry to include earth abundant 3d metal complexes and investigating

their PET processes is paramount in creating sustainable materials for optoelectronic applications. To accomplish this, D–B–A type complexes with dissymmetric alkynyl ligands need to be realized.

In the preparation of dissymmetric alkynyl D–B–A complexes, a mono-alkynyl species is first synthesized.[5,6] Using this stepwise approach, it is possible to investigate the properties of each independent unit (D–B, B–A), the dissymmetric complex (D–B–A), and the symmetric complexes (D–B–D, A–B–A). Selective synthesis of mono-alkynyl species of Co^{III}(cyclam) complexes was first reported by Shores,[7] which proceeded under the weak base conditions. Our laboratory has published several examples of dissymmetric alkynyl complexes with Ru_2 and Co^{III}(cyclam) metal centers.[8–11] Femtosecond transient absorption and time-resolved IR spectroscopic studies of $[Co(cyclam)(C_2NAP^{iPr})(C_2D)]^+$ complexes (C_2NAP^{iPr} = 4-ethynyl-*N*-ispropyl-1,8-napthalimide, D = C_6H_4-4-NMe_2, Ph, or C_6H_4-4-N(4-$MeOPh)_2$), revealed the formation of desirable CS states, which were quickly deactivated by the low-lying Co-centered triplet states.[9] This necessitates further investigation of other macrocyclic 3d metal alkynyl bridges that sustain long-lived CS and metal-to-ligand charge transfer states.

Macrocyclic chromium alkynyl chemistry emerged with Taube and coworkers' $[Cr^{III}(phthalocyanine)(C_2Ph)_2]^-$ complex.[12] Following this, Berben and Long reported several $Cr^{III}(Me_3TACN)(C_2R)_3$ type complexes (Me_3TACN = *N*,*N*′,*N*″-trimethyl-1,4,7-triazacyclononane, R = C_2SiMe_3, C_2H, C_4SiMe_3, and C_4H),[13] and Cr^{III}(cyclam) alkynyl complexes, *trans*-$[Cr(cyclam)(C_2R)_2]^+$ (R = C_2SiMe_3, C_2H) and *trans*-$[Cr(cyclam)(1,3\text{-}C_2C_6H_4C_2H)_2]^+$.[14] Additional Cr^{III}(cyclam) alkynyl complexes have been documented by the groups of Wagenknecht,[15] Nishijo,[16–19] and Ren.[20] Recent explorations of macrocyclic chromium alkynyl chemistry in our group include the study of *cis*-/*trans*-$[Cr^{III}(cyclam')(C_2R)_2]^+$ type complexes, where cyclam′ is the *C*-substituted cyclam derivative DMC[21] (DMC = 5,12-dimethyl-1,4,8,11-tetraazacyclotetradecane) or HMC (HMC = 5,5,7,12,12,14-hexamethyl-1,4,8,11-tetraazacyclotetradecane).[22,23] Thus far, all macrocyclic Cr^{III} alkynyl complexes feature symmetric bis-alkynyl ligands, while D–B–A type complexes have yet to be realized.

Examples of Cr mono-alkynyl complexes are known but sparse. Smith's laboratory synthesized several $CpCr^{III}$-[$(ArNCMe)_2CH$](R) complexes, including R = C_2H, in order to study Cr–R bond homolysis (Ar = *ortho*-disubstituted aryl).[24] Earlier work by Smith resulted in $CpCr(NO)(N^iPr_2)(R)$ type complexes (R = C_2CMe_3 and C_2Ph), where the stability of the complexes was attributed to the π-bonding interactions of the $[Cr(NO)(N^iPr_2)]^{2+}$ core.[25] Two (η^5-

$C_5H_4R)Cr(NO)_2$-C_2Ph complexes (R = H or $COOCH_3$) were synthesized (*via* CuI catalyzed coupling) and characterized.[26] Berben discovered a unique dinuclear complex *trans*-$[(Me_3SiCC)(dmpe)_2Cr]_2(\mu\text{-}N_2)$ (dmpe = 1,2-bis(dimethylphosphino)ethane) from the reaction between *trans*-$Cr(dmpe)_2Cl_2$ and $LiCCSiMe_3$ under N_2,[27] and analogous compounds were further investigated by Shores.[28] Also based on $Cr^{II}(dmpe)_2$, Berke and coworkers synthesized a series of mono-alkynyl $Cr^{II}(dmpe)_2$ complexes using trimethylstannyl and sodium alkynyl reagents.[29,30] Macrocyclic chromium mono-alkynyl complexes have thus far remained elusive. Reported herein are the syntheses and characterizations of a unique series of Cr^{III}(HMC) mono-alkynyl complexes **3.1a** – **3.4a**, and new bis-alkynyl complexes **3.3b** and **3.4b**.

3.3 Results and Discussion

3.3.1 Synthesis

As shown in Scheme 3.1, the reaction between *trans*-[Cr(*meso*-HMC)Cl_2]OTf and three equivalents of the appropriate lithium arylalkynyl produced the bis-alkynyl complexes *trans*-[Cr(HMC)$(C_2Ph)_2$]OTf (**3.1b**),[23] *trans*-[Cr(HMC)$(C_2Np)_2$]OTf (**3.2b**),[22] *trans*-[Cr(HMC)$(C_2C_6H_4{}^tBu)_2$]OTf (**3.3b**), and *trans*-[Cr(HMC)$(C_2(3,5\text{-}Cl_2C_6H_3))_2$]OTf (**3.4b**). The bis-alkynyl complexes were filtered through Celite and further purified over silica, with yields between 41–73% depending on the nature of arylalkynyl ligand. Mono-alkynyl complexes *trans*-[Cr(HMC)(C_2Ph)Cl]OTf (**3.1a**), *trans*-[Cr(HMC)(C_2Np)Cl]OTf (**3.2a**), *trans*-[Cr(HMC)$(C_2C_6H_4{}^tBu)$Cl]OTf (**3.3a**), and *trans*-[Cr(HMC)$(C_2(3,5\text{-}Cl_2C_6H_3))$Cl]OTf (**3.4a**) were then synthesized by the reaction of the appropriate *trans*-[Cr(HMC)$(C_2Ar)_2$]OTf with a stoichiometric amount of HCl in CH_3OH. Purification over silica resulted in yields of *trans*-[Cr(HMC)(C_2Ar)Cl]OTf ranging between 85–93%. A one-step synthesis of *trans*-[Cr(HMC)(C_2Ph)Cl]Cl was attempted by combining a substoichiometric amount of LiC_2Ph with *trans*-[Cr(HMC)Cl_2]Cl, however, the yield of *trans*-[Cr(HMC)(C_2Ph)Cl]Cl was <12% based on Cr (see Section 3.6.1). The improved two-step synthesis of **3.1a** resulted in an overall percent yield of 48% (based on Cr in *trans*-[Cr(HMC)Cl_2]OTf), while other arylalkynyl ligands saw overall yields of up to 67%.

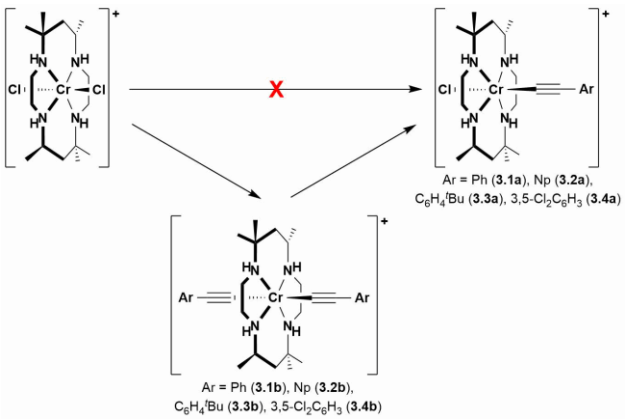

Scheme 3.1. General synthesis of Cr^{III}(HMC) mono-alkynyl complexes through acid degradation of Cr^{III}(HMC) bis-alkynyl complexes.

Previous studies on the alkynylation of the *cis*/*trans* isomers of $[Cr(HMC)Cl_2]^+$ have revealed the $[Cr(HMC)(C_2R)_2]^+$ products retain their *cis*/*trans* stereochemistry (R = Ph, C_2SiMe_3, and Np).[22,23] This is in contrast to the alkynylation of Cr(cyclam) and Cr(DMC) complexes, which produced a mixture of *cis*/*trans* products when *cis*-$[Cr(cyclam/DMC)Cl_2]^+$ starting material was employed.[15,21] We attempted to synthesize both *cis*- and *trans*-$[Cr(HMC)(C_2Ar)Cl]^+$ complexes, however, the *cis*-complexes were much less stable and often fully degraded to *cis*-$[Cr(HMC)Cl_2]Cl$ in acidified solution. At present, our focus is on the more robust *trans*-$[Cr(HMC)(C_2Ar)Cl]OTf$ complexes.

Like the corresponding bis-alkynyl complexes, mono-alkynyl species **3.1a** – **3.4a** are paramagnetic with room temperature effective magnetic moments (Evans method) corresponding to $S = 3/2$. While well resolved ^1H NMR spectra for complexes **3.1a** – **3.4a** are unattainable, their compositions were analyzed with ESI-MS and elemental analysis.

3.3.2 Molecular Structures

Mono-alkynyl complexes **3.1a** – **3.4a** have been characterized with single crystal X-ray diffraction. The cations were crystallized as the chloride (**3.1a**) or triflate (**3.2a**, **3.3a**, and **3.4a**) salts, and the molecular structures are shown in Figures 3.1 – 3.4. Selected bond lengths and bond angles are provided in Table 3.1. Molecular structures for **3.3b** and **3.4b** are presented in Figure 3.S2 and 3.S3 along with select bond lengths and angles in Table 3.S2. All complexes have pseudo-octahedral geometry and retain *trans* stereochemistry.

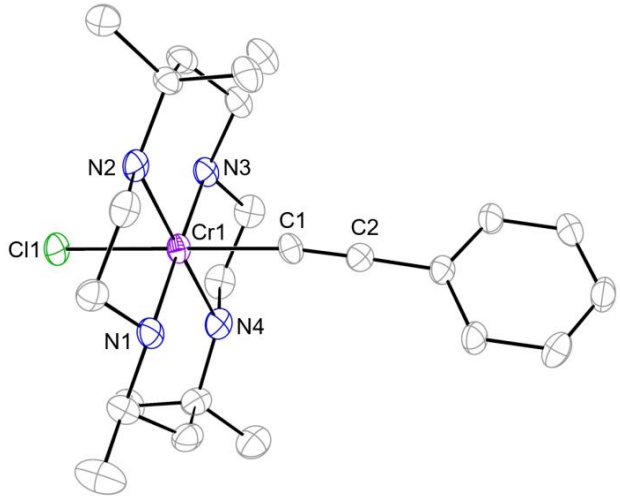

Figure 3.1. ORTEP plot of [**3.1a**]$^{+}$ at 30% probability level. H atoms and the Cl^{-} counterion were omitted for clarity.

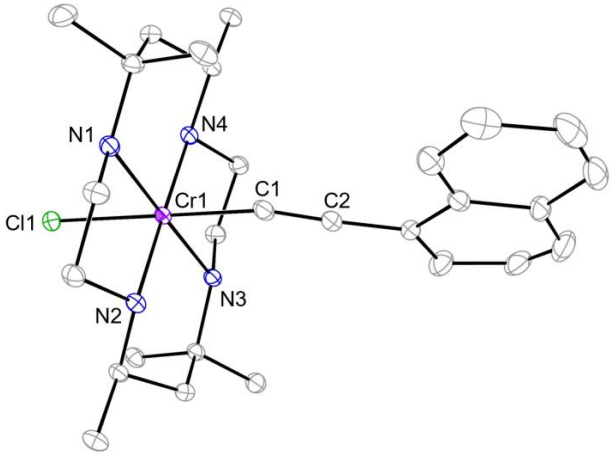

Figure 3.2. ORTEP plot of [**3.2a**]$^{+}$ at 30% probability level. H atoms, $^{-}$OTf counterion, and disorder were omitted for clarity.

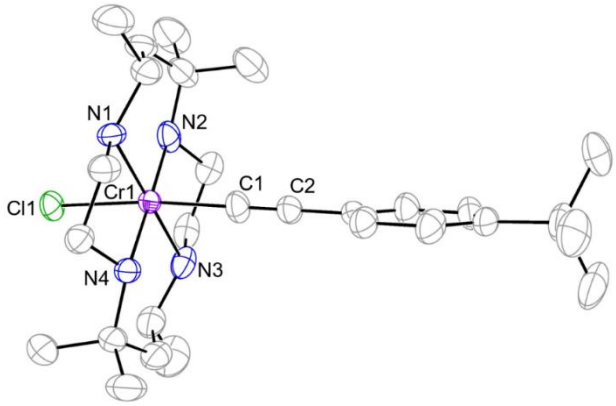

Figure 3.3. ORTEP plot of [**3.3a**]$^{+}$ at 30% probability level. H atoms, $^{-}$OTf counterion, and disorder were omitted for clarity.

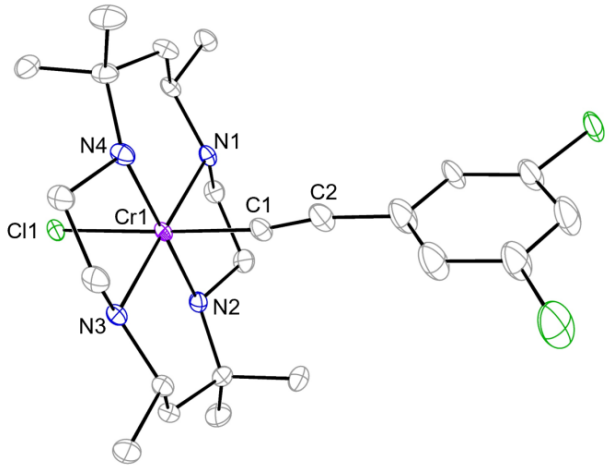

Figure 3.4. ORTEP plot of [**3.4a**]$^{+}$ at 30% probability level. H atoms, $^{-}$OTf counterion, and disorder were omitted for clarity.

The Cr–C bond length of 2.049(4) Å in [**3.1a**]Cl is comparable to those observed for *trans*-[Cr(cyclam)(C_2Ph)$_2$]$^{+}$ (avg. 2.073 Å) and **3.1b** (avg. 2.085 Å), but slightly shortened by *ca.* 0.024/0.036 Å, respectively.[23,37] The shorter Cr–C bond distance is not unexpected, as acetylides are stronger donors than chloro ligands, and in both *trans*-[Cr(cyclam)(C_2Ph)$_2$]$^{+}$ and *trans*-[Cr(HMC)(C_2Ph)$_2$]Cl there is a distinct *trans*-influence by the two alkynyl ligands.[23,37] A similar trend is observed for **3.2a** with a Cr–C bond length of 2.035(2) Å, while the average of those for *trans*-[Cr(HMC)(C_2Np)$_2$]Cl is 2.078 Å;[21] and for **3.4a** with a Cr–C bond length of 2.028(2) Å (*ca.* 0.047 Å shorter than those of **3.4b**). A more significant contrast in the Cr–C bond length is observed between **3.3a** and **3.3b** (*ca.* 0.091 Å). This is attributed to the fact that *tert*-

butylphenylacetylide is the strongest σ-donor in the series and forms the strongest Cr–C bond in its mono-alkynyl complex but exhibits the highest *trans*-influence in the bis-alkynyl complex.

Table 3.1. Selected bond lengths (Å) and bond angles (°) for **3.1a** – **3.4a**.

	[**3.1a**]Cl	**3.2a**	**3.3a**	**3.4a**
Cr1–N1	2.074(4)	2.077(1)	2.092(8)	2.077(2)
Cr1–N2	2.090(4)	2.096(1)	2.092(8)	2.092(2)
Cr1–N3	2.080(4)	2.074(1)	2.064(9)	2.075(2)
Cr1–N4	2.113(4)	2.088(1)	2.086(9)	2.107(2)
Cr1–C1	2.049(4)	2.035(2)	2.014(7)	2.028(2)
Cr1–Cl1	2.3678(13)	2.3704(4)	2.372(6)	2.3615(5)
C1–C2	1.205(7)	1.251(3)	1.192(4)	1.210(3)
C1–Cr1–Cl1	176.93(14)	179.81(5)	173.9(3)	178.11(7)
Cr1–C1–C2	168.1(5)	159.0(2)	174.2(4)	170.9(2)
N1–Cr1–N3	178.70(15)	171.19(5)	179.6(4)	179.11(7)
N2–Cr1–N4	179.55(16)	179.23(4)	178.3(4)	178.99(6)
N1–Cr1–N2	85.27(17)	85.15(6)	93.8(3)	84.38(4)
N1–Cr1–N4	94.85(18)	95.49(6)	84.6(4)	95.12(4)
N2–Cr1–N3	94.92(17)	94.50(7)	86.5(4)	95.28(4)
N3–Cr1–N4	84.95(18)	84.87(7)	95.2(4)	85.22(4)

The C≡C bond lengths of **3.1a**, **3.3a**, **3.4a** are comparable to one another, as well as to the corresponding bis-alkynyl complexes **3.1b**, **3.3b**, and **3.4b**. The C≡C bond length of **3.2a** is 1.251(3) Å, which is notably longer than the observed range (1.150–1.225 Å, esd ≤ 0.010 Å) for C≡C bonds in complexes containing MC≡CR (R = C, Si) bonds.[38] The ethynylnapthalene ligand in the crystal structure of **3.2a** is disordered (Figure 3.S1) and was refined to have an occupancy ratio of 0.576(3) to 0.424(3). The disordered moiety has a C≡C bond length of 1.221(4) Å, which falls within the well-established range of metal-alkynyl bonds. The disordered moiety also possesses a Cr1–C1–C2 bond angle that is in better agreement with **3.1a**, **3.3a**, and **3.4a**, at 167.7(2)° compared to 159.0(2)° reported for **3.2a**.

3.3.3 UV-vis Spectroscopic Analysis

The UV-vis absorption spectra of mono-alkynyl complexes **3.1a** – **3.4a** compared to their bis-alkynyl counterparts, **3.1b** – **3.4b**, are shown in Figures 3.5–3.8. The absorption is assigned to the $^4A_{2g} \rightarrow {}^4T_{1g}/{}^4T_{2g}$ (O_h) transition. Similar to the Cr bis-alkynyl complexes, all mono-alkynyl complexes display structured d–d bands between 300 and 450 nm for **3.1a**, **3.3a**, and **3.4a**, and between 400–550 nm for complex **3.2a**. The bathochromic shift of the metal-based absorption of **3.2a** is a result of increased ligand aromaticity and has been previously observed.[15,22] The d–d bands of mono-alkynyl complexes are slightly red shifted from their bis-alkynyl analogues (<5 nm) due to the chloro substituent being a weaker field ligand than the arylalkynyl ligand. The intensities of these d–d bands are rather high in comparison to those seen for halide complexes *trans*-$[Cr(HMC)X_2]^+$, which reinforces the previous presumption of a partial charge-transfer character due to strong dπ–π(C≡C) mixing.[23] As shown in Figures 3.5–3.8, the molar extinction coefficients of the d–d bands in **3.1a** – **3.4a** are approximately half of those for their corresponding *trans*-$[Cr(HMC)(C_2Ar)_2]$OTf complexes, corroborating the presumption of significant contributions from dπ–π(C≡C) mixing.

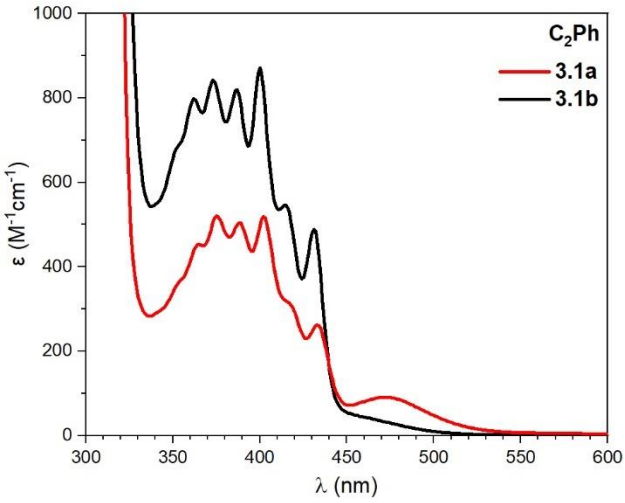

Figure 3.5. UV-vis absorption spectra of complexes **3.1a** and **3.1b** as CH_2Cl_2 solutions.

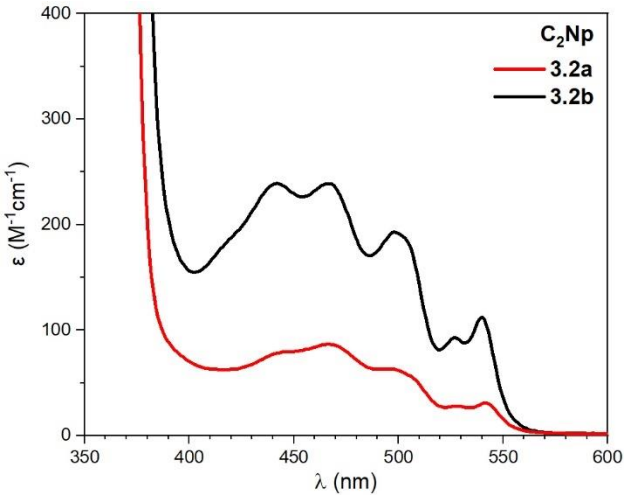

Figure 3.6. UV-vis absorption spectra of complexes **3.2a** and **3.2b** as CH_2Cl_2 solutions.

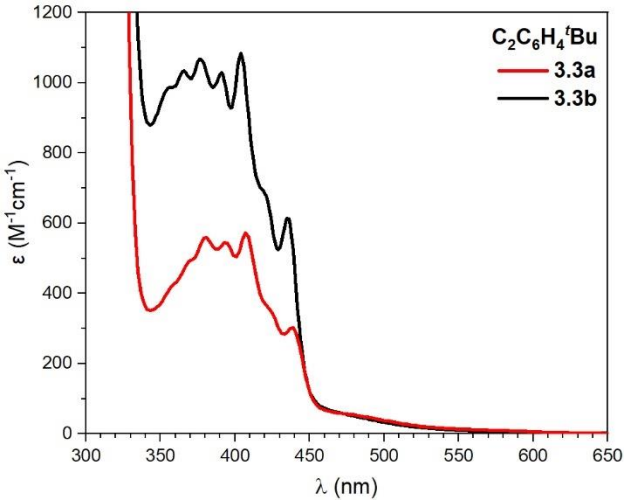

Figure 3.7. UV-vis absorption spectra of complexes **3.3a** and **3.3b** as CH_2Cl_2 solutions.

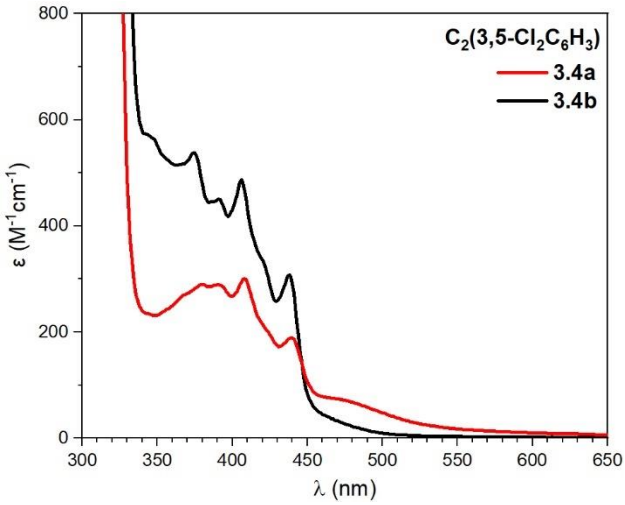

Figure 3.8. UV-vis absorption spectra of complexes **3.4a** and **3.4b** as CH_2Cl_2 solutions.

Similar to the bis-alkynyl complexes, the mono-alkynyl complexes also exhibit intense absorptions below 330 nm (not shown) that are associated with charge transfer and intraligand π–π* transitions. Also like the bis-alkynyl complexes, replacement of one of the halide ligands leads to a stronger ligand field, thus the $^4T_{1g}$ term seen for halide $[Cr(HMC)X_2]^+$ complexes is likely beyond the UV-vis window or hidden beneath the charge transfer bands.[23]

The highly-structured nature of the d–d bands is still the most prominent feature of the spectra, and ideally, the origin of the vibronic progressions may be determined from the FT-IR of the complexes. The vibronic progressions have been calculated for **3.1a** – **3.4a** (see Figure 3.S7 and Table 3.S4). For **3.1a**, **3.3a**, and **3.4a**, the progressions average between 860–980 cm^{-1}, similar to the *trans*-$[Cr(HMC)(C_2Ar)_2]Cl$ complexes. It is difficult to determine the vibrational mode(s) responsible for the vibronic progressions due to the possible occurrence of aromatic C–H bending, N–H bending and methylene vibrations within the same region.[23] The irregularly spaced progressions for **3.2a** average a spacing of around 1043 cm^{-1}, which aligns more closely with aromatic C≡C stretching modes or phenyl ring deformations in the Np ligand, as previously suggested for **3.2b**.[22]

3.3.4 Emission Studies

Complexes **3.1a** – **3.4a** exhibit Cr^{III} emission centered around 725 nm, as shown in Figures 3.9–3.12. Phosphorescence in octahedral Cr^{III} complexes occurs as a result of intersystem crossing from the $^4T_{1g}$ or $^4T_{2g}$ excited states to two possible lower-lying doublet states, $^2T_{1g}$ and ^2E_g.[39] The

emission of complexes **3.1a** – **3.4a** is attributed to a $^2T_{1g} \rightarrow {}^4A_{2g}$ transition, which is consistent with the previous report of emissions by bis-alkynyl complexes **3.1b** and **3.2b**. This assignment is partially based on the red shift from where ^2E_g emission is usually observed.[40] The phosphorescence spectra of complexes **3.1a** – **3.4a** exhibit fine-structuring at 77 K, which is believed to be vibronic in origin.[41] Stronger vibronic coupling between the alkynyl ligand and the Cr metal center results in more defined structuring of complexes **3.1a** – **3.4a** in comparison to complexes **3.1b** – **3.4b**. This interpretation is supported by the shorter Cr–C bond lengths observed in the mono-alkynyl species. For complexes **3.1a** – **3.4a**, a blue shift of approximately 20 nm is observed compared to **3.1b** – **3.4b** (Table 3.2). This can be attributed to the nephelauxetic effect as the electron cloud is more localized between the Cr metal center and the alkynyl ligand in complexes **3.1a** – **3.4a**, resulting in higher energy emission. While the new mono-alkynyl complexes **3.1a** – **3.4a** display a single $^2T_{1g} \rightarrow {}^4A_{2g}$ emission, a weaker secondary emission of $^2E_g \rightarrow {}^4A_{2g}$ origin was previously noted for bis-alkynyl complex **3.2b** at 77 K.[22] A secondary emission is also identified for the new bis-alkynyl complex **3.3b** at 726 nm.

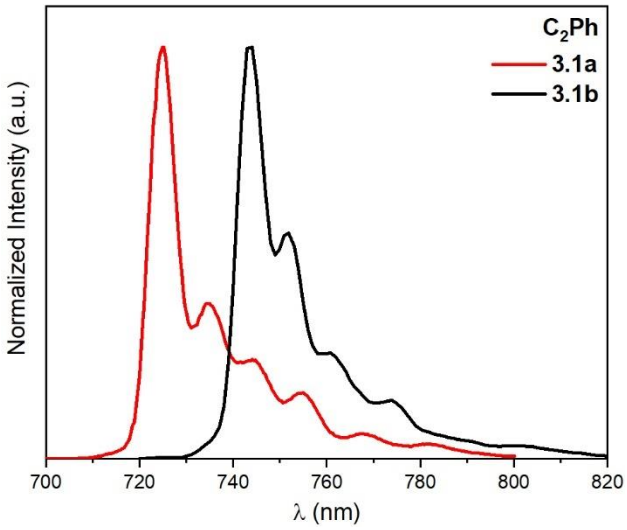

Figure 3.9. Normalized emission spectra of complexes **3.1a** and **3.1b** in a 4:1 EtOH/MeOH glass measured at 77 K.

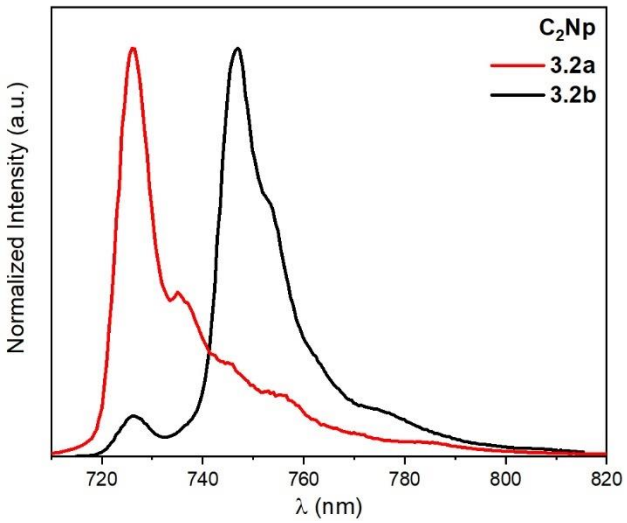

Figure 3.10. Normalized emission spectra of complexes **3.2a** and **3.2b** in a 4:1 EtOH/MeOH glass measured at 77 K.

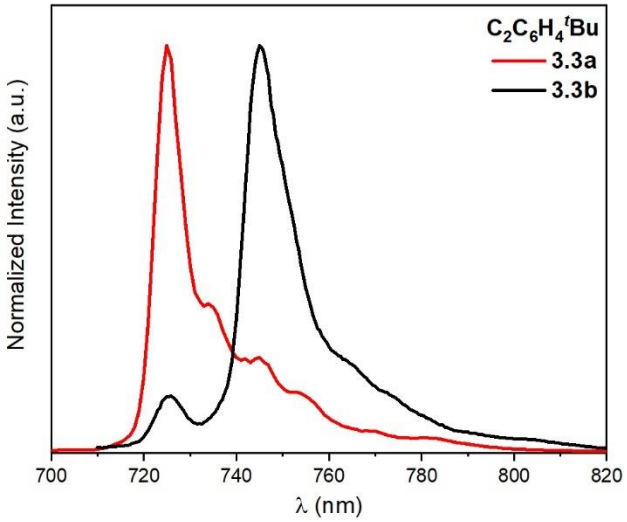

Figure 3.11. Normalized emission spectra of complexes **3.3a** and **3.3b** in a 4:1 EtOH/MeOH glass measured at 77 K.

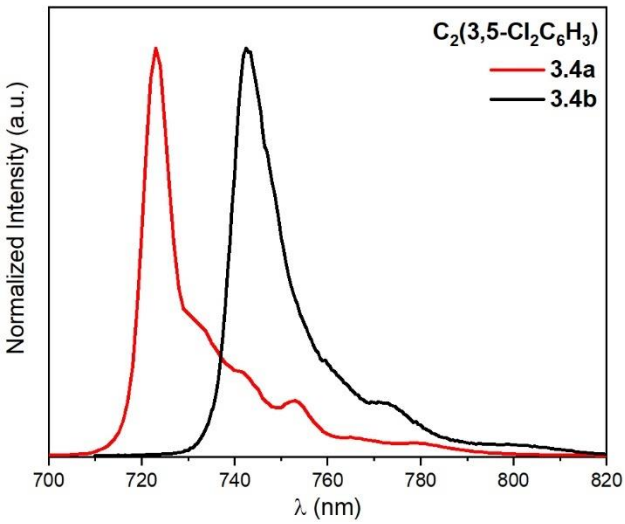

Figure 3.12. Normalized emission spectra of complexes **3.4a** and **3.4b** in a 4:1 EtOH/MeOH glass measured at 77 K.

Table 3.2. Photophysical data for mono-alkynyl complexes **3.1a** – **3.4a** and bis-alkynyl complexes **3.1b** – **3.4b**.

	***Frozen Glass*[a]**			***Room Temperature*[b]**		
	λ_{ex} (nm)	**λ_{em} (nm)**	**τ (μs)**	**λ_{ex} (nm)**	**λ_{em} (nm)**	**τ (μs)**
3.1a	400	725	397	400	725	123
3.2a	466	735	367	466	728	78
3.3a	406	725	383	406	728	87
3.4a	408	723	343	408	725	22
3.1b	425	744	469	425	746	164
3.2b	445	747	447	445	747	218
		727 [c]	362			
3.3b	403	745	479	403	748	117
		726 [c]	345			
3.4b	406	743	354	406	747	51

[a] Measured at 77 K in a 4:1 EtOH/MeOH glass
[b] Measured at room temperature in degassed MeCN
[c] $^2E_g \rightarrow {}^4A_{2g}$ emission

Relevant parameters for the emissions of **3.1a** – **3.4a** and **3.1b** – **3.4b** are compiled in Table 3.2. Complexes **3.1a** – **3.4a** have fairly long lifetimes, ranging between 343 μs to 397 μs. The

lifetimes of **3.1b**, **3.2b**, and **3.3b** are between 70–89 μs longer than those of **3.1a**, **3.2a**, and **3.3a**, respectively. In the case of **3.4b**, the lifetime is only 11 μs longer than that of **3.4a**, which can likely be attributed to the presence of two heavy chloride atoms leading to increased non-radiative decay. All four *trans* mono-alkynyl complexes have longer lifetimes than *cis*-[Cr(HMC)(C_2Ph)$_2$]Cl and *cis*-[Cr(HMC)(C_2Np)$_2$]Cl, which is unsurprising when considering that the distortions in the CN_2R_2 plane of *cis*-complexes often result in larger non-radiative decay rates, and thus shorter lifetimes.[42]

3.4 Conclusion

Cr^{III} mono-alkynyl complexes supported by the HMC macrocycle have been realized with the synthesis of complexes **3.1a** – **3.4a**, thus expanding the repertoire of Cr^{III} alkynyl chemistry. All complexes display structured d–d bands like the bis-alkynyl complexes, with approximately halved molar absorptivity values. As with the bis-alkynyl complexes, complexes **3.1a** – **3.4a** exhibit long-lived phosphorescence at 77 K. The emission spectra of **3.1a** – **3.4a** are more structured than their bis-alkynyl counterparts as a result of stronger vibronic coupling between the Cr^{III} metal center and the alkynyl ligand, which is supported by the mono-alkynyl complexes displaying shorter Cr–C bond lengths than their bis-alkynyl counterparts. With these mono-alkynyl complexes of Cr(HMC) being realized, synthetic efforts can be made toward dissymmetric bis-alkynyl complexes based on Cr(HMC).

3.5 Experimental Section

General Methods. Phenylacetylene was purchased from Oakwood Chemical and used without further purification. HMC,[31] *trans*-[Cr(HMC)Cl_2]Cl/OTf,[32] *trans*-[Cr(HMC)(C_2Ph)$_2$]Cl/OTf,[23] *trans*-[Cr(HMC)(C_2Np)$_2$]Cl/OTf,[22] TMS-C_2Np,[33] TMS-$C_2C_6H_4{}^t$Bu,[34] and TMS-C_2(3,5-$Cl_2C_6H_3$)[35] were prepared according to literature procedures. THF was freshly distilled over Na/benzophenone. The preparation of bis-alkynyl complexes **3.1b** and **3.2b** was performed under a dry N_2 atmosphere using standard Schlenk procedures,[21,23] and new complexes **3.3b** and **3.4b** were synthesized similarly. Preparation of mono-alkynyl complexes **3.1a** – **3.4a** was carried out under ambient conditions. Unless specified, the counter anion is always triflate ($^-$OTf; $CF_3SO_3^-$) in this study.

Physical Methods. Elemental analysis was performed by Atlantic Microlab, Inc. in Norcross, GA. UV-vis spectra were obtained with a JASCO V-670 spectrophotometer in CH_2Cl_2 solutions. Emission data were recorded on a Varian Cary Eclipse fluorescence spectrophotometer. FT-IR spectra were measured as neat samples with a JASCO FT/IR-6300 spectrometer equipped with an ATR accessory. ESI-MS were analyzed on an Advion Mass Spectrometer. Magnetic susceptibility was calculated *via* the Evans method[36] using ^{1}H NMR spectra that were recorded on a Varian Inova 300 spectrometer operating at 300 MHz. Single crystal X-ray diffraction data were collected on Nonius Kappa CCD and Bruker Quest instruments as detailed in Section 3.6.2.

***trans*-[Cr(HMC)(C_2Ph)Cl]OTf (3.1a).** The reaction between 0.070 g (0.11 mmol) of *trans*-[Cr(HMC)(C_2Ph)$_2$]OTf and 1 equiv of 0.12 M HCl in MeOH yielded a yellow solution, which was stirred for 20 mins under ambient conditions. Solvent was removed by rotary evaporation, and a yellow solid (0.059 g, 93% based on Cr) was obtained after purification through a silica plug with **3.1a** eluted in 9:1 CH_2Cl_2:CH_3OH. An analogous procedure was used to obtain [**3.1a**]Cl from *trans*-[Cr(HMC)(C_2Ph)$_2$]Cl, from which a crystal was grown by slow diffusion of Et_2O into MeOH. Elem. Anal. Found (Calcd) for *trans*-[Cr(HMC)(C_2Ph)Cl]OTf·3H_2O: C, 44.8 (44.5); H, 6.6 (6.7); N, 8.5 (8.3). UV-vis, λ_{max}/nm (ε/M^{-1} cm^{-1}): 365 (450), 375 (520), 388 (500), 402 (520), 417 (sh), 433 (260), 472 (90). FT-IR ν(C≡C)/cm^{-1}: 2088w. ESI-MS [M^+]: 472 *m*/*z* for the cationic species [**3.1a**]$^+$. Magnetic susceptibility, μ_{eff}/μ_B: 3.85.

***trans*-[Cr(HMC)(C_2Np)Cl]OTf (3.2a).** The reaction between *trans*-[Cr(HMC)(C_2Np)$_2$]OTf (0.050 g, 0.063 mmol) and 1 equiv of 0.12 M HCl in 10 mL CH_3OH yielded an orange solution, which was stirred for 20 mins under ambient conditions. Solvent was removed by rotary evaporation and an orange solid (0.039 g, 92% based on Cr) was obtained after purification through a silica gel plug, eluted with 9:1 CH_2Cl_2:MeOH. Single crystals suitable for X-ray diffraction were grown from vapor diffusion of Et_2O into MeCN. Elem. Anal. Found (Calcd) for *trans*-[Cr(HMC)(C_2Np)Cl]OTf·0.5MeCN·0.5H_2O: C, 51.5 (51.4); H, 6.6 (6.4); N, 8.9 (9.0). UV-vis, λ_{max}/nm (ε/M^{-1} cm^{-1}): 442 (78), 467 (87), 498 (63), 528 (28), 542 (31). FT-IR ν(C≡C)/cm^{-1}: 2080w. ESI-MS [M^+]: 522 *m*/*z* for the cationic species [**3.2a**]$^+$. Magnetic susceptibility, μ_{eff}/μ_B: 3.86.

***trans*-[Cr(HMC)($C_2C_6H_4$^{t}Bu)Cl]OTf (3.3a).** The reaction between 0.050 g (0.074 mmol) of *trans*-[Cr(HMC)($C_2C_6H_4$^{t}Bu)$_2$]OTf and 1 equiv of 0.12 M HCl in MeOH yielded a yellow solution, which was stirred for 20 mins under ambient conditions. Solvent was removed by rotary evaporation and a yellow solid (0.037 g, 88% based on Cr) was obtained after purification through

a silica plug, with **3.3a** eluted with 9:1 CH_2Cl_2:MeOH. Single crystals suitable for X-ray diffraction were grown from slow diffusion of Et_2O into MeOH. Elem. Anal. Found (Calcd) for *trans*-[Cr(HMC)($C_2C_6H_4{}^tBu$)Cl]OTf: C, 51.1 (51.4); H, 7.4 (7.3); N, 8.1 (8.3). UV-vis, λ_{max}/nm (ε/M^{-1} cm^{-1}): 379 (560), 393 (550), 407 (570), 423 (360), 438 (300). FT-IR ν(C≡C)/cm^{-1}: 2083w. ESI-MS [M^+]: 528 *m*/*z* for the cationic species [**3.3a**]$^+$. Magnetic susceptibility, μ_{eff}/μ_B: 3.86.

***trans*-[Cr(HMC)(C_2(3,5-$Cl_2C_6H_3$))Cl]OTf (3.4a).** The reaction between 0.080 g (0.12 mmol) of *trans*-[Cr(HMC)(C_2(3,5-$Cl_2C_6H_3$))$_2$]OTf and 1 equivalent of 0.12 M HCl in MeOH yielded a golden yellow solution, which was stirred for 20 mins under ambient conditions. Solvent was removed by rotary evaporation and a golden yellow solid (0.057 g, 85% based on Cr) was obtained after purification through a silica gel plug, with **3.4a** eluting in 9:1 CH_2Cl_2:CH_3OH. Single crystals suitable for X-ray diffraction were grown from slow diffusion of Et_2O into MeCN. Elem. Anal. Found (Calcd) for *trans*-[Cr(HMC)(C_2(3,5-$Cl_2C_6H_3$))Cl]OTf·1MeOH·0.5H_2O: C, 42.85 (42.7); H, 5.9 (6.1); N, 7.8 (7.6). UV-vis, λ_{max}/nm (ε/M^{-1} cm^{-1}): 380 (290), 391 (290), 408 (300), 422 (sh), 439 (190). FT-IR ν(C≡C)/cm^{-1}: 2085w. ESI-MS [M^+]: 543 *m*/*z* for the cationic species [**3.4a**]$^+$. Magnetic susceptibility, μ_{eff}/μ_B: 3.86.

***trans*-[Cr(HMC)($C_2C_6H_4{}^tBu$)$_2$]OTf (3.3b).** A suspension of *trans*-[Cr(HMC)Cl_2]OTf (0.100 g, 0.180 mmol) in 15 mL THF was combined with 3 equiv of $LiC_2C_6H_4{}^tBu$ (prepared from 0.543 mmol TMS-$C_2C_6H_4{}^tBu$ in THF and 0.75 mmol *n*-BuLi), and the reaction mixture was stirred for 2 h at room temperature. After quenching the reaction in air, solvent was removed *via* rotary evaporation. A silica gel plug was used for purification and **3.3b** was eluted with 9:1 CH_2Cl_2:MeOH to yield (0.083 g, 58% yield based on Cr). Single crystals suitable for X-ray diffraction were grown from slow diffusion of hexanes into CH_2Cl_2. Elem. Anal. Found (Calcd) for *trans*-[Cr(HMC)($C_2C_6H_4{}^tBu$)$_2$]OTf·1.5H_2O·0.5MeCN: C, 57.3 (57.1); H, 7.6 (7.6); N, 7.2 (7.1). UV-vis, λ_{max}/nm (ε/M^{-1} cm^{-1}): 366 (1030), 377 (1070), 391 (1030), 404 (1080), 418 (700), 435 (620). FT-IR ν(C≡C)/cm^{-1}: 2082w. ESI-MS [M^+]: 650 *m*/*z* for the cationic species [**3.3b**]$^+$. Magnetic susceptibility, μ_{eff}/μ_B: 3.89.

***trans*-[Cr(HMC)(C_2(3,5-$Cl_2C_6H_3$))$_2$]OTf (3.4b).** A suspension of *trans*-[Cr(HMC)Cl_2]OTf (0.35 g, 0.63 mmol) and HC_2(3,5-$Cl_2C_6H_3$) (0.32 g, 1.9 mmol) in 25 mL THF was combined with 3.8 mL of 0.5 M LDA (1.9 mmol, prepared from the reaction of 0.6 mL diisopropylamine with 1.6 mL *n*-BuLi in 5.8 mL THF at 77 K), and the reaction mixture was stirred for 2 h at room temperature. After quenching the reaction in air, solvent was removed *via* rotary evaporation. A

silica gel plug was used for purification and **3.4b** was eluted with 9:1 CH_2Cl_2:MeOH (0.213 g, 41% yield based on Cr). Single crystals suitable for X-ray diffraction were grown from slow diffusion of Et_2O into MeCN. Elem. Anal. Found (Calcd) for *trans*-[Cr(HMC)(C_2(3,5-$Cl_2C_6H_3$))$_2$]OTf: C, 48.0 (48.0); H, 5.1 (5.1); N, 6.8 (6.8). UV-vis, λ_{max}/nm (ε/M^{-1} cm^{-1}): 374 (540), 391 (450), 406 (490), 419 (sh), 438 (310). FT-IR ν(C≡C)/cm^{-1}: 2079w. ESI-MS [M^+]: 679 *m*/*z* for the cationic species [**3.4b**]$^+$. Magnetic susceptibility, μ_{eff}/μ_B: 3.76.

3.6 Supporting Information

3.6.1 Synthetic Details

trans-[Cr(meso-*HMC*)(C_2Ph)Cl]Cl via lithiation ([1a]Cl). The reaction between 0.336 g of *trans*-[Cr(*meso*-HMC)Cl_2]Cl (0.76 mmol) and 1.2 equiv of LiC_2Ph yielded 0.0407 g of [**3.1a**]Cl (0.08 mmol, 11% based on Cr) after recrystallization from CH_2Cl_2/MeOH and Et_2O.

cis-[Cr(rac-*HMC*)(C_2Ph)Cl]Cl via lithiation. The reaction between 0.500 g of *cis*-[Cr(*rac*-HMC)Cl_2]Cl (1.13 mmol) and 0.95 equivalents of LiC_2Ph yielded 0.0013 g of *cis*-[Cr(rac-HMC)(C_2Ph)Cl]Cl after recrystallization from CH_2Cl_2/Et_2O (0.003 mmol, 0.23% based on Cr) and 0.1682 g of *cis*-[Cr(*rac*-HMC)Cl_2]Cl were recovered.

cis-[Cr(rac-*HMC*)(C_2Ph)Cl]Cl via acid degradation. 0.100 g of *cis*-[Cr(*rac*-HMC)(C_2Ph)$_2$]Cl (0.174 mmol) were dissolved in CH_3OH and 1.0 mL of a 0.12 M HCl methanol solution (0.127 mmol, 0.7 equiv) were added. The solution immediately became more purple in color. The reaction was left to stir for approximately 30 mins, upon which there appeared to be no solid formation. ESI-MS showed complete conversion to the desired product. The solvent was removed *via* rotary evaporation and the residue was dissolved in CH_2Cl_2. A purple-gray solid was precipitated with the addition of Et_2O, yielding 0.0787 g (0.15 mmol, 89% based on Cr). Recrystallization was attempted from MeOH/Et_2O and CH_2Cl_2/Et_2O, however, a teal blue solid gradually appeared, indicating the formation of *cis*-[Cr(HMC)Cl_2]Cl.

Table 3.S1. Total percent yield of **3.1a** – **3.4a** based on Cr in *trans*-[Cr(HMC)Cl_2]OTf.

Complex	Aryl	Total Yield
3.1a	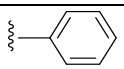	48%
3.2a	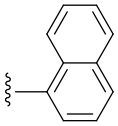	67%
3.3a	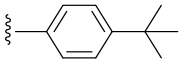	51%
3.4a	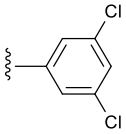	35%

3.6.2 X-ray Crystallographic Details

Single crystals of [**3.1a**]Cl and **3.3a** were grown *via* slow diffusion of Et_2O into a concentrated MeOH solution. Single crystals of **3.2a**, **3.4a**, and **3.4b** were grown *via* vapor diffusion (**3.2a**) or slow diffusion (**3.4a** and **3.4b**) of Et_2O into a concentrated solution of MeCN. Single crystals of **3.3b** were grown *via* slow diffusion of hexanes into a concentrated solution of CH_2Cl_2. X-ray diffraction data for [**3.1a**]Cl were collected on a Nonius KappaCCD diffractometer using Mo Kα (λ = 0.71073 Å) at 200 K. Data were collected using the Nonius Collect software[43], processed using HKL3000[2] and data were corrected for absorption and scaled using Scalepack.[44] The structure of [**3.1a**]Cl was solved using the structure solution program PATTY in DIRDIF99[45]. Data for **3.2a**, **3.4a**, and **3.4b** were collected at 150 K on a Bruker Quest diffractometer with a fixed chi angle, a sealed tube fine focus X-ray tube with Mo Kα radiation (λ = 0.71073 Å), single crystal curved graphite incident beam monochromator, a Photon II area detector, and an Oxford Cryosystems low temperature device. Data for **3.3a** and **3.3b** were collected at 150 K on a Bruker Quest diffractometer with kappa geometry, an I-μ-S microsource X-ray tube, laterally graded multilayer (Goebel) mirror for monochromatization, a Photon-II (**3.3b**) or Photon-III (**3.3a**) area detector and an Oxford Cryosystems low temperature device. with Cu Kα radiation (λ = 1.54178 Å). Data for **3.2a**, **3.3a**, **3.4a**, **3.3b**, and **3.4b** were collected and processed using APEX3[46] and reduced using SAINT, space groups were assigned using XPREP within the SHELXTL[47,48] suite of programs, solved using ShelXS[48] (**3.2a**, **3.3a**, **3.3b**, **3.4a**) or ShelXM[48] (**3.4b**). All structures were refined using Shelxl2018 and the graphical interface Shelxle.[49-51] If not specified otherwise,

H atoms attached to carbon and nitrogen atoms, as well as hydroxyl hydrogens, were positioned geometrically and constrained to ride on their parent atoms. C–H bond distances were constrained to 0.95 Å for aromatic, and to 1.00, 0.99 and 0.98 Å for aliphatic C–H, CH_2 and CH_3 moieties, respectively. O–H distances of alcohols were constrained to 0.84 Å. Methyl CH_3 hydroxyl H atoms were allowed to rotate but not to tip to best fit the experimental electron density. U_{iso}(H) values were set to a multiple of U_{eq}(C) with 1.5 for CH_3 and OH, and 1.2 for C–H, CH_2 and N–H units, respectively.

If not specified otherwise, H atoms attached to carbon and nitrogen atoms, as well as hydroxyl hydrogens, were positioned geometrically and constrained to ride on their parent atoms. C–H bond distances were constrained to 0.95 Å for aromatic, and to 1.00, 0.99 and 0.98 Å for aliphatic C–H, CH_2 and CH_3 moieties, respectively. O–H distances of alcohols were constrained to 0.84 Å. Ammonium N-H distances were either constrained to 1.00 Å (**3.1a**, **3.3a**, **3.3b**, **3.4a**), or the H atom positions were freely refined (**3.2a**, **3.4b**). Methyl CH_3 and hydroxyl H atoms were allowed to rotate but not to tip to best fit the experimental electron density. U_{iso}(H) values were set to a multiple of U_{eq}(C/N/O) with 1.5 for CH_3 and OH, and 1.2 for C–H, CH_2 and N–H units, respectively, with the exception of U_{iso}(H) values for ammonium H atoms of **3.4b**, which were freely refined.

Complete crystallographic data, in CIF format, have been deposited with the Cambridge Crystallographic Data Centre. CCDC 2067384 – 2067389 contain the supplementary crystallographic data for this paper. These data can be obtained free of charge from The Cambridge Crystallographic Data Centre via www.ccdc.cam.ac.uk/data_request/cif.

Special refinement details of [3.1a]Cl. In complex [**3.1a**]Cl, an OMIT command was used to remove reflections with high error. The methanol solvate molecule is disordered and refined to occupy two positions. U^{ij} components of their ADPs were restrained to be similar (SIMU command). The C-O bond distances were restrained to a target value of 1.43 Å (DFIX). The positions of the H1A and H1B atoms of the O–H group were restrained to a target value of 2.1 and 2.5 Å from the Cl2 counteranion, respectively. Subject to these conditions the occupancy rates refined to be 0.49(1) and 0.51(1).

Special refinement details of 3.2a. In complex **3.2a**, the ethynylnapthalene ligand is disordered and is refined to occupy two positions. The two disordered moieties were restrained to have similar bond angles and lengths (SAME command). U^{ij} components of their ADPs were

restrained to be similar (SIMU command). Subject to these conditions, the occupancy rates refined to be 0.576(3) and 0.424(3). A hydrogen bond exists between O3 of the triflate counteranion and N1 of the macrocyclic ligand. An OMIT command was used to remove a reflection with high error.

Special refinement details of 3.3a. In complex **3.3a**, the Cr, HMC macrocycle, and Cl are disordered and is refined to occupy three positions. The three disordered moieties were restrained to have similar bond angles and lengths (SAME command). U^{ij} components of their ADPs were restrained to be similar (SIMU command). A SUMP command was used to constrain the occupancies of the three components to unity. Subject to these conditions the occupancy rates refined to be 0.406(1), 0.361(3), and 0.233(3).

The tert-butyl group on the tert-butylphenylacetylene ligand is disordered and is refined to occupy two positions. The two disordered moieties were restrained to have similar bond angles and lengths (SAME command). U^{ij} components of their ADPs were restrained to be similar (SIMU command). Subject to these conditions the occupancy rates refined to be 0.548(9) and 0.452(9). The triflate counteranion is disordered and is refined to occupy three positions with the SO_3 unit always pointing towards the N–H groups of the macrocycle and the methanol solvate molecules. The three disordered moieties were restrained to have the same S–O, C–F, and C–O bond distances (SADI command). U^{ij} components of their ADPs were restrained to be similar (SIMU command). A hydrogen bond exists between O1B of the triflate counteranion and N1C of the macrocyclic ligand. Subject to these conditions the occupancy rates refined to be 0.541(3), 0.250(3), and 0.209(3).

The methanol solvent molecule is disordered and is refined to occupy three positions. The C-O bond distances were restrained to a target value (DFIX). The O-H groups are restrained to be H-bonded to the SO_3 groups of the triflate counteranion. The methyl H atoms were first refined with HFIX 137 (rotating) and then with AFIX 3 (pure riding). Subject to these conditions the occupancy rates refined to be 0.406(1), 0.406(1), and 0.188(3).

Special refinement details of 3.4a. In complex **3.4a**, the dichlorophenyl phenyl moiety of the dichlorophenylacetylene substituent is disordered extensively. Disorder over four orientations, differing mostly by rotation around the acetylene axis, was refined. A SUMP command was used to constrain the occupancies of the four components of the ligand to unity. The four disordered moieties were restrained to have similar bond angles and lengths (SAME command). A SADI command was used to restrain the C2–C3 bond lengths to be similar within the four disordered

ligand parts. The phenyl rings were restrained to be planar (FLAT command). U^{ij} components of their ADPs were restrained to be similar (SIMU command). Subject to these conditions the occupancy rates refined to be 0.310(3), 0.333(3), 0.0634(16), and 0.294(3).

A diethyl ether solvent molecule, adjacent to the disordered dichlorophenyl phenyl moiety, was refined as disordered over two mutually exclusive positions. A DFIX command was used to restrain equivalent C–O and C–C bond lengths within the molecule to target values. A SAME command was used to restrain the bond angles and lengths of the two disordered component to be similar to each other. U^{ij} components of ADPs were restrained to be similar for all disordered atoms. Subject to these conditions the occupancy ratios refined to 0.652(5) and 0.348(5).

The triflate counteranion was refined as disordered over two orientations by a "wiggle" movement of the SO_3 unit. A SAME command was used to restrain the bond angles and lengths of the two disordered component to be similar to each other. U^{ij} components of their ADPs were restrained to be similar (SIMU command). Subject to these conditions the occupancy ratios refined to 0.618(9) and 0.382(9).

Special refinement details of 3.3b. In complex **3.3b**, one tert-butyl alkynyl substituent in the structure is *ca*. 1:1 disordered. The substituent is disordered by a rotation of the tert-butyl group and an upwards bend of the phenylene ring.

The two parts of the disordered ligand were restrained to have similar bond angles and lengths as observed in the non-disordered ligand (SAME command). U^{ij} components of their ADPs were restrained to be similar (SIMU command). The atoms C3 and C3B were constrained to have identical positions (EXYZ) and same anisotropic displacement parameters (EADP). Subject to these conditions the occupancy ratio refined to 0.546(7) to 0.454(7).

Special refinement details of 3.4b. In complex **3.4b**, an OMIT command was used to omit reflections with high error.

Table 3.S2. Crystal data for mono-alkynyl complexes **3.1a**, **3.2a**, **3.3a**, and **3.4a** and bis-alkynyl complexes **3.3b** and **3.4b**.

	[**3.1a**]Cl	**3.2a**	**3.3a**	**3.4a**	**3.3b**	**3.4b**
chemical formula	$C_{25}H_{45}Cl_2CrN_4O$	$C_{31}H_{46}ClCrF_3N_5O_3S$	$C_{30}H_{53}ClCrF_3N_4O_4S$	$C_{89}H_{150}Cl_9Cr_3F_9N_{13}O_{12}S_3$	$C_{41}H_{62}CrF_3N_4O_3S$	$C_{35}H_{45}Cl_4CrF_3N_5O_3S$
fw, g/mol	540.55	713.24	710.27	2336.44	800.00	866.62
space group	*C*2/c (No. 15)	$P2_1$/c (No. 14)	$P\bar{1}$ (No. 2)	$P\bar{3}$ (No. 147)	$P2_1$/n (No. 14)	$P\bar{1}$ (No. 2)
a, Å	29.5012(5)	16.7207(8)	11.3221(5)	24.2698(6)	15.3929(15)	9.838(2)
b, Å	11.5356(2)	12.2764(6)	13.1665(6)	24.2698(6)	13.5965(12)	13.224(4)
c, Å	16.5203(4)	17.8968(8)	14.2387(7)	11.2278(4)	22.0346(16)	17.386(4)
α °	90	90	64.220(2)	90	90	93.298(16)
β °	91.120(1)	110.330	69.482(3)	90	109.307	105.918(16)
γ °	90	90	72.759(3)	120	90	107.430(16)
V, Å^3	5621.02(19)	3444.8(3)	1763.81(15)	5727.4(3)	4352.3(7)	2051.0(9)
Z	8	4	2	2	4	2
T, K	200	150	150	150	150	150
λ, Å	0.71073	0.71073	1.54178	0.71073	1.54178	0.71073
ρ_{calcd}, g/cm^3	1.278	1.375	1.337	1.355	1.221	1.403
R	0.075	0.040	0.069	0.055	0.075	0.042
$R_w(F^2)$	0.246	0.113	0.220	0.155	0.233	0.125

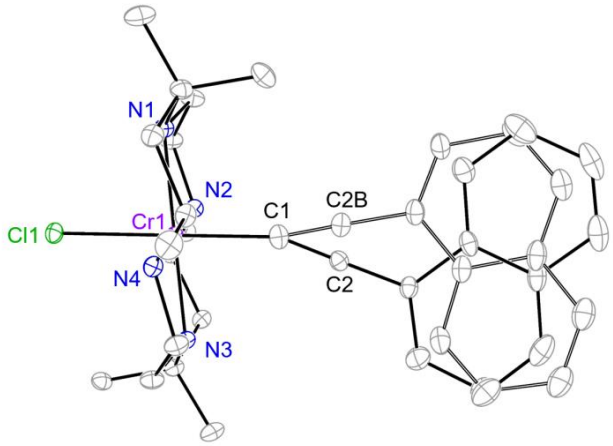

Figure 3.S1. ORTEP plot of **3.2a** at 30% probability level with both disordered C_2Np fragments. H atoms and the $^{-}$OTf counteranion were omitted for clarity.

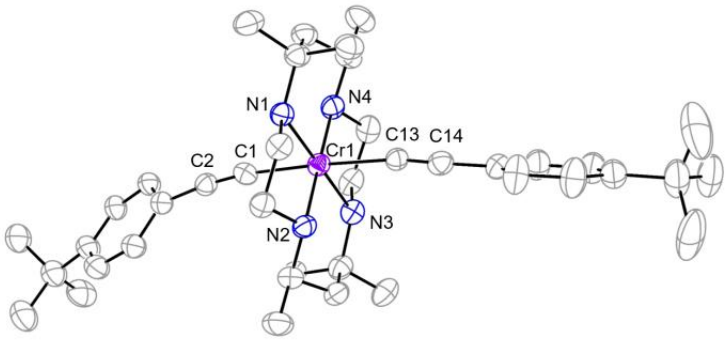

Figure 3.S2. ORTEP plot of **3.3b** at 30% probability level. H atoms and the $^{-}$OTf counteranion were omitted for clarity.

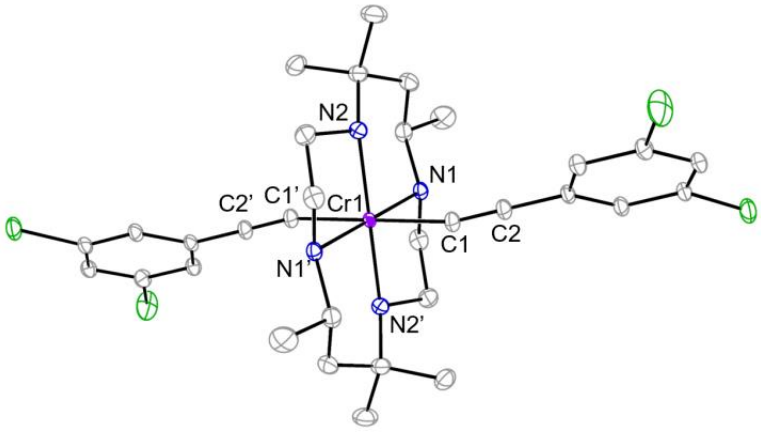

Figure 3.S3. ORTEP plot of **3.4b** at 30% probability level. H atoms and the $^{-}$OTf counteranion were omitted for clarity.

Table 3.S3. Selected bond lengths (Å) and bond angles (°) for **3.3b** and **3.4b**.

	3.3b	**3.4b**[a]
Cr1–N1	2.065(3)	2.0815(12)
Cr1–N2	2.097(4)	2.0910(13)
Cr1–N3	2.074(3)	-
Cr1–N4	2.093(3)	-
Cr1–C1	2.085(7)	2.0745(13)
Cr1–C13	2.123(5)	-
C1–C2	1.17(1)	1.2223(16)
C13–C14	1.137(8)	-
C1–Cr1–C1	-	180.00(6)
C1–Cr1–C13	177.1(2)	-
Cr1–C1–C2	172.4(5)	166.12(2)
Cr1–C13–C14	170.6(4)	-
N1–Cr1–N3	179.4(1)	-
N2–Cr1–N4	179.5(2)	-
N1–Cr1–N2	84.8(2)	84.68(5)
N1–Cr1–N2'	-	95.32(5)
N1–Cr1–N4	95.3(1)	-
N2–Cr1–N3	94.6(2)	-
N3–Cr1–N4	85.3(1)	-

[a]The unit cell revealed two crystallographically independent molecules; geometric parameters for only one of them are listed here.

3.6.3 Absorption Details

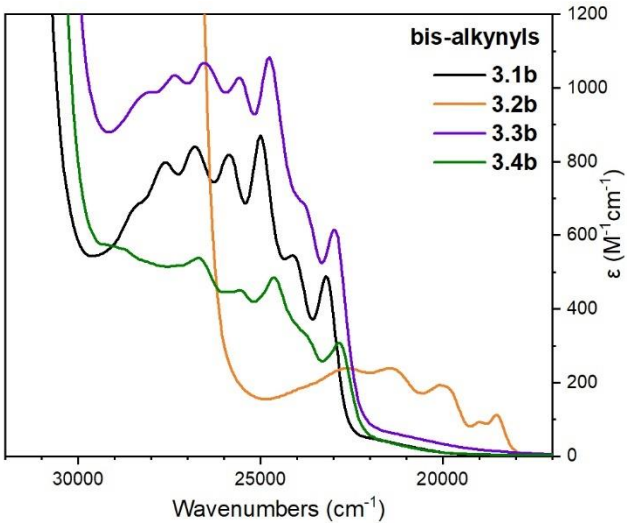

Figure 3.S4. UV-vis absorption spectra of *trans*-[Cr(HMC)(C_2Ar)$_2$]OTf complexes as CH_2Cl_2 solutions, where Ar = Ph (black), Np (orange), $C_6H_4{}^tBu$ (purple), and 3,5-$Cl_2C_6H_3$ (green).

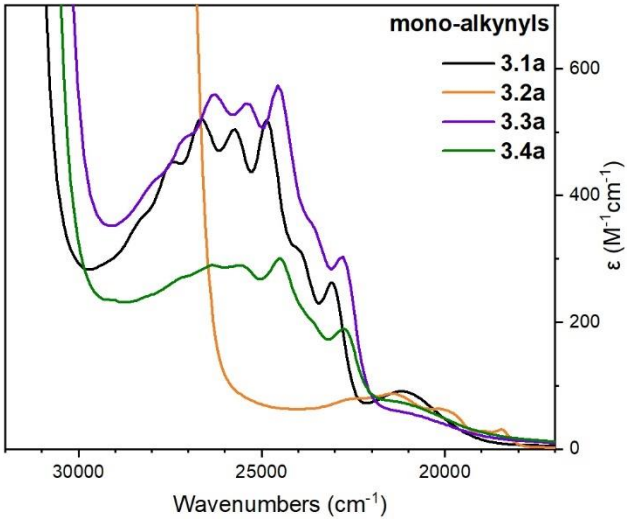

Figure 3.S5. UV-vis absorption spectra of *trans*-[Cr(HMC)(C_2Ar)Cl]OTf complexes as CH_2Cl_2 solutions, where Ar = Ph (black), Np (orange), $C_6H_4{}^tBu$ (purple), and 3,5-$Cl_2C_6H_3$ (green).

Table 3.S4. Vibronic progression analysis of **3.1a** – **3.4a**, **3.3b**, and **3.4b**.

	Peaks Considered, cm^{-1}	**Vibronic Progression, cm^{-1}**
3.1a	27397.26 26666.67 25773.19 24875.62 23980.81 23094.69	730.59 893.48 897.57 894.81 886.12
3.2a	22624.43 21413.27 20080.32 18939.39 18450.18	1211.16 1332.95 1140.93 489.21
3.3a	27173.91 26385.22 25445.29 24570.02 23640.66 22831.05	788.69 939.93 875.27 929.36 809.61
3.4a	26315.79 25575.45 24509.80 23696.68 22779.04	740.34 1065.65 813.12 917.64
3.3b	27322.40 26525.20 25575.45 24752.48 23923.44 22988.51	797.20 949.75 822.97 829.04 934.93
3.4b	26737.97 25575.45 24630.54 23866.35 22831.05	1162.52 944.91 764.19 1035.3

3.6.4 IR Characterization

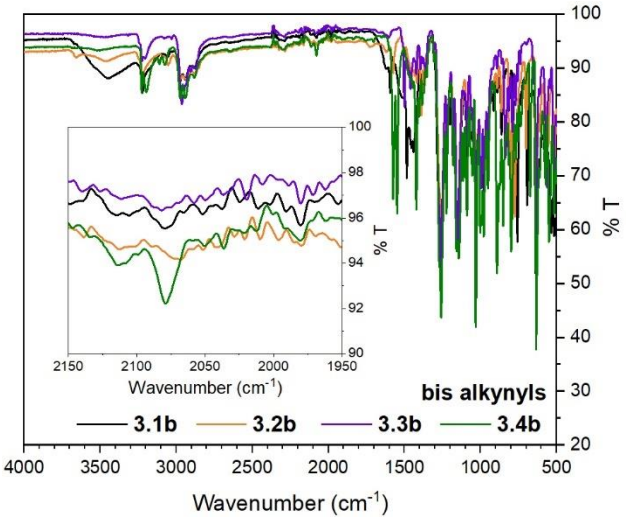

Figure 3.S6. FTIR of *trans*-[Cr(HMC)(C_2Ar)$_2$]OTf complexes, where Ar = Ph (black), Np (orange), $C_6H_4{}^t$Bu (purple), and 3,5-$Cl_2C_6H_3$ (green).

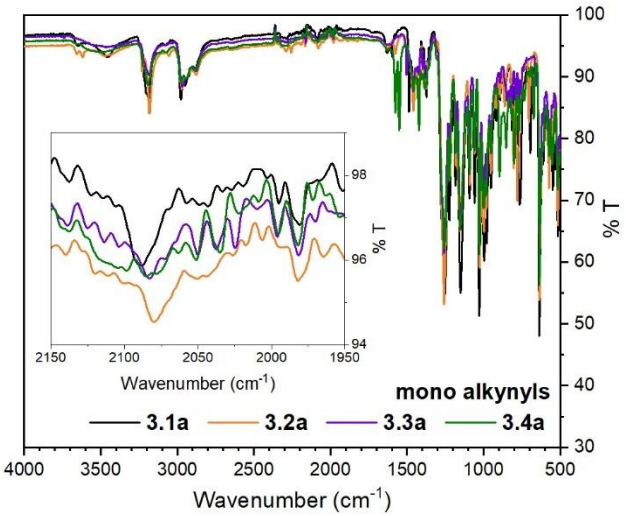

Figure 3.S7. FTIR of *trans*-[Cr(HMC)(C_2Ar)Cl]OTf complexes, where Ar = Ph (black), Np (orange), $C_6H_4{}^t$Bu (purple), and 3,5-$Cl_2C_6H_3$ (green).

3.6.5 Emission Details

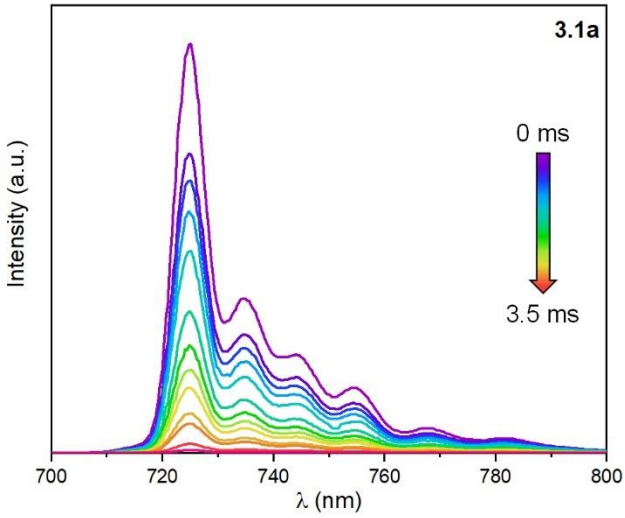

Figure 3.S8. Time-delayed phosphorescence spectrum for **3.1a** in 4:1 EtOH:MeOH glass at 77 K and varying delay times.

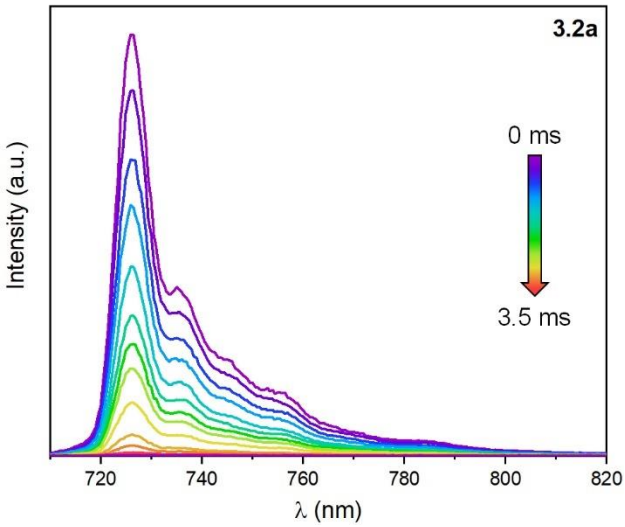

Figure 3.S9. Time-delayed phosphorescence spectrum for **3.2a** in 4:1 EtOH:MeOH glass at 77 K and varying delay times.

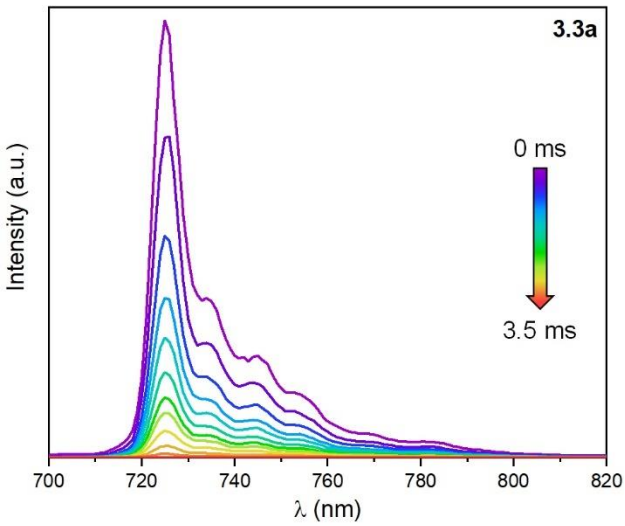

Figure 3.S10. Time-delayed phosphorescence spectrum for **3.3a** in 4:1 EtOH:MeOH glass at 77 K and varying delay times.

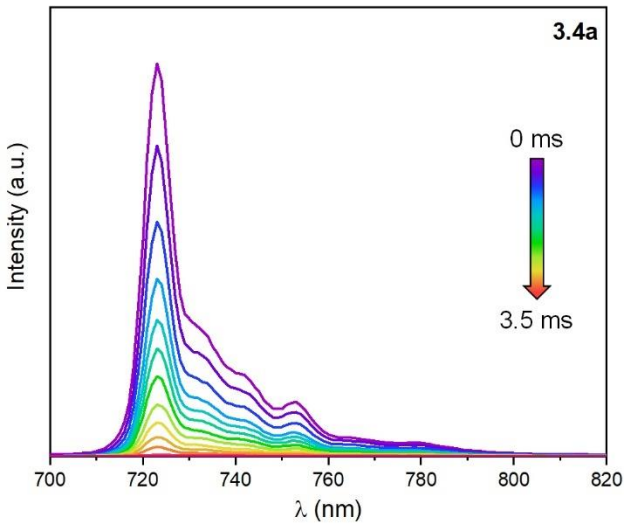

Figure 3.S11. Time-delayed phosphorescence spectrum for **3.4a** in 4:1 EtOH:MeOH glass at 77 K and varying delay times.

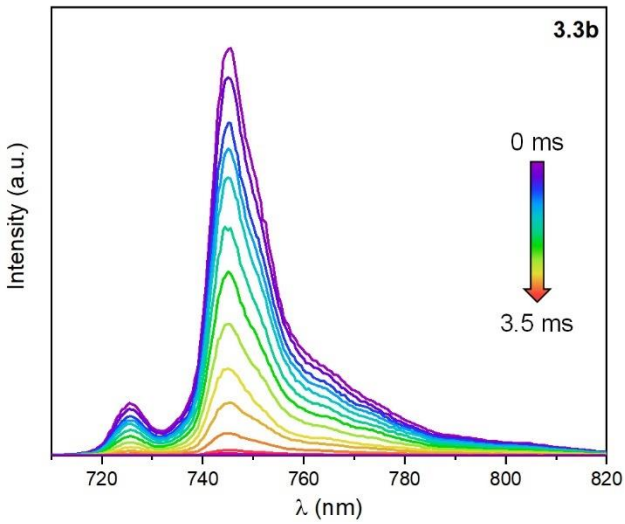

Figure 3.S12. Time-delayed phosphorescence spectrum for **3.3b** in 4:1 EtOH:MeOH glass at 77 K and varying delay times.

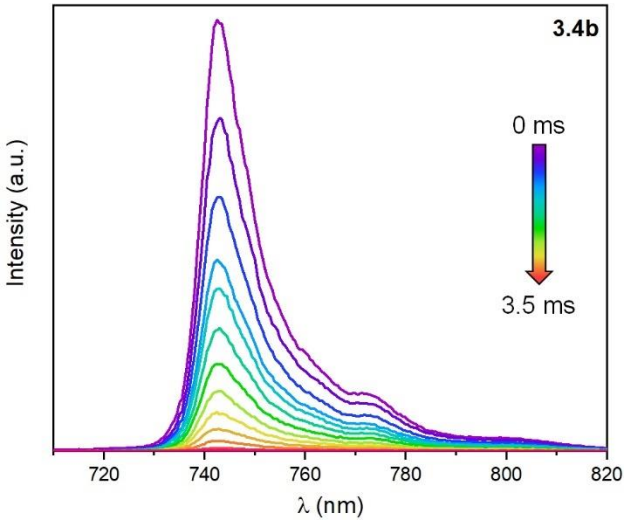

Figure 3.S13. Time-delayed phosphorescence spectrum for **3.4b** in 4:1 EtOH:MeOH glass at 77 K and varying delay times.

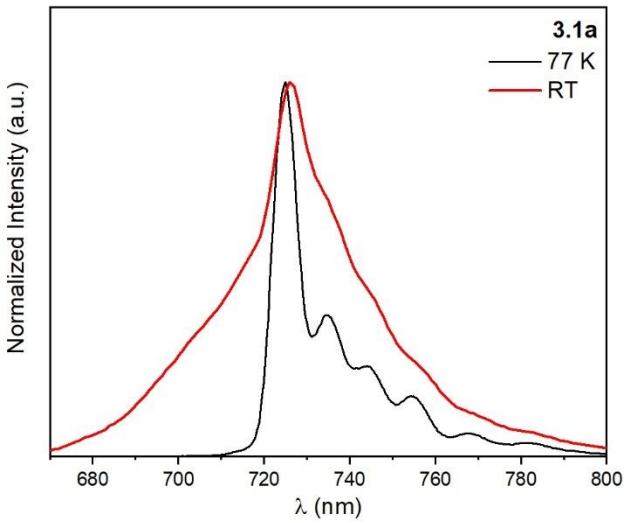

Figure 3.S14. Emission spectra of **3.1a** at RT in degassed MeCN and 77 K in 4:1 EtOH:MeOH glass.

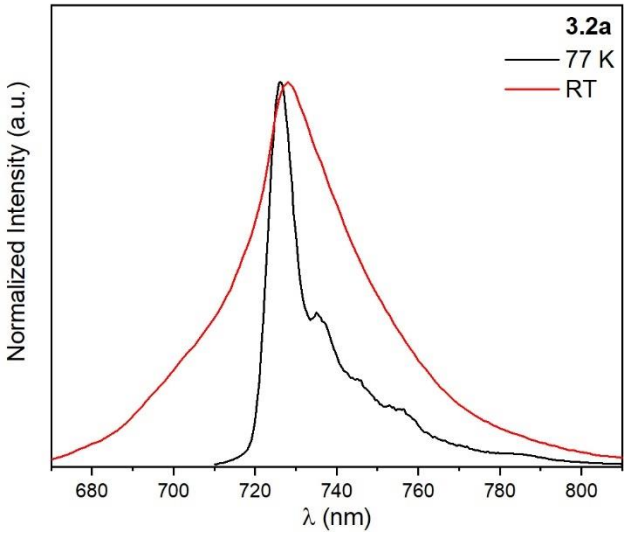

Figure 3.S15. Emission spectra of **3.2a** at RT in degassed MeCN and 77 K in 4:1 EtOH:MeOH glass.

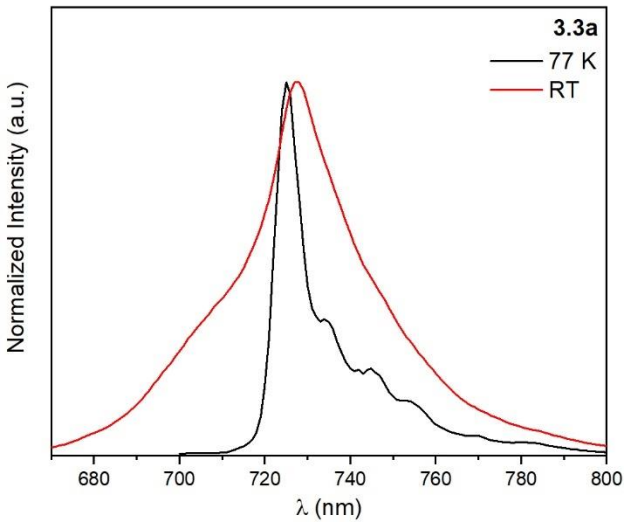

Figure 3.S16. Emission spectra of **3.3a** at RT in degassed MeCN and 77 K in 4:1 EtOH:MeOH glass.

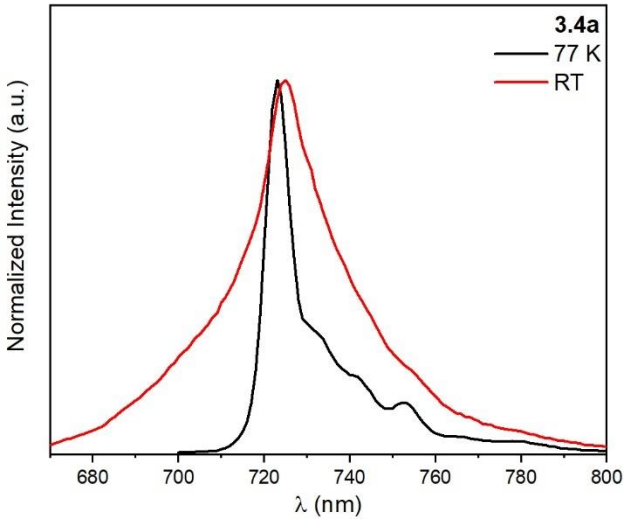

Figure 3.S17. Emission spectra of **3.4a** at RT in degassed MeCN and 77 K in 4:1 EtOH:MeOH glass.

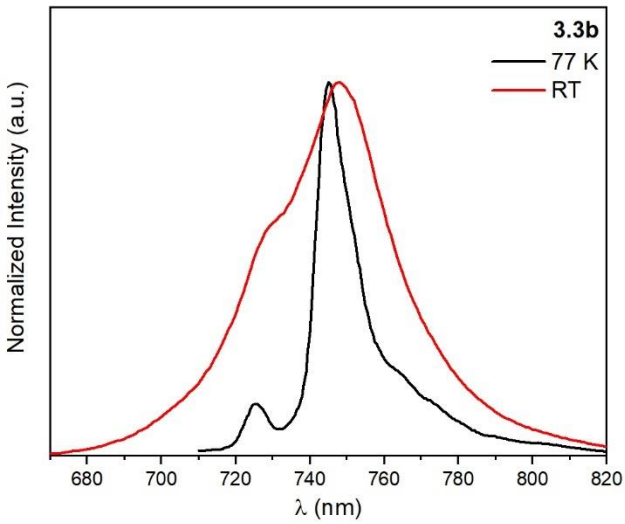

Figure 3.S18. Emission spectra of **3.3b** at RT in degassed MeCN and 77 K in 4:1 EtOH:MeOH glass.

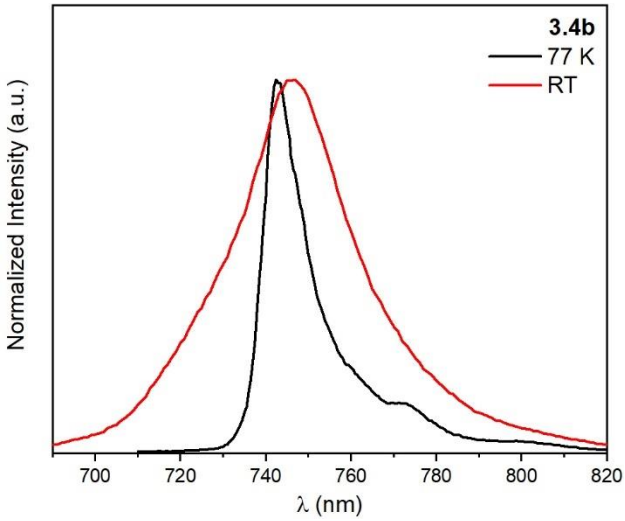

Figure 3.S19. Emission spectra of **3.4b** at RT in degassed MeCN and 77 K in 4:1 EtOH:MeOH glass.

3.7 References

1. N. J. Long and C. K. Williams, *Angew. Chem., Int. Ed.*, 2003, **42**, 2586–2617
2. M. I. Bruce and P. J. Low, *Adv. Organomet. Chem.*, 2004, **50**, 179–444
3. A. Haque, R. A. Al-Balushi, I. J. Al-Busaidi, M. S. Khan and P. R. Raithby, *Chem. Rev.*, 2018, **118**, 8474–8597
4. M. Delor, P. A. Scattergood, I. V. Sazanovich, A. W. Parker, G. M. Greetham, A. J. H. M. Meijer, M. Towrie and J. A. Weinstein, *Science*, 2014, **346**, 1492–1495
5. S. D. Banziger and T. Ren, *J. Organomet. Chem.*, 2019, **885**, 39–48
6. T. Ren, *Chem. Commun.*, 2016, **52**, 3271–3279
7. W. A. Hoffert, M. K. Kabir, E. A. Hill, S. M. Mueller and M. P. Shores, *Inorg. Chim. Acta*, 2012, **380**, 174–180
8. S. N. Natoli, M. Zeller and T. Ren, *Inorg. Chem.*, 2016, **55**, 5756–5758
9. S. D. Banziger, X. Li, J. Valdiviezo, M. Zeller, P. Zhang, D. N. Beratan, I. V. Rubtsov and T. Ren, *Inorg. Chem.*, 2019, **58**, 15487–15497
10. S. D. Banziger, M. Zeller and T. Ren, *Eur. J. Inorg. Chem.*, 2019, 4766–4772
11. J.-W. Ying, A. Cordova, T. Y. Ren, G.-L. Xu and T. Ren, *Chem. – Eur. J.*, 2007, **13**, 6874–6882
12. R. Taube, H. Drevs and G. Marx, *Z. Anorg. Allg. Chem.*, 1977, **436**, 5–19
13. L. A. Berben and J. R. Long, *J. Am. Chem. Soc.*, 2002, **124**, 11588–11589
14. L. A. Berben, Ph.D. Dissertation, University of California, Berkeley, 2005
15. C. Sun, C. R. Turlington, W. W. Thomas, J. H. Wade, W. M. Stout, D. L. Grisenti, W. P. Forrest, D. G. VanDerveer and P. S. Wagenknecht, *Inorg. Chem.*, 2011, **50**, 9354–9364
16. J. Nishijo, Y. Shima and M. Enomoto, *Polyhedron*, 2017, **136**, 35–41
17. J. Nishijo and M. Enomoto, *Inorg. Chim. Acta*, 2015, **437**, 59–63
18. J. Nishijo and M. Enomoto, *Inorg. Chem.*, 2013, **52**, 13263–13268
19. J. Nishijo, K. Judai, S. Numao and N. Nishi, *Inorg. Chem.*, 2009, **48**, 9402–9408
20. W. P. Forrest, Z. Cao, R. Hambrick, B. M. Prentice, P. E. Fanwick, P. S. Wagenknecht and T. Ren, *Eur. J. Inorg. Chem.*, 2012, **2012**, 5616–5620

21. E. C. Judkins, S. F. Tyler, M. Zeller, P. E. Fanwick and T. Ren, *Eur. J. Inorg. Chem.*, 2017, **2017**, 4068–4076

22. E. C. Judkins, M. Zeller and T. Ren, *Inorg. Chem.*, 2018, **57**, 2249–2259

23. S. F. Tyler, E. C. Judkins, Y. Song, F. Cao, D. R. McMillin, P. E. Fanwick and T. Ren, *Inorg. Chem.*, 2016, **55**, 8736–8743

24. K. C. MacLeod, J. L. Conway, B. O. Patrick and K. M. Smith, *J. Am. Chem. Soc.*, 2010, **132**, 17325–17334

25. E. W. Jandciu, J. Kuzelka, P. Legzdins, S. J. Rettig and K. M. Smith, *Organometallics*, 1999, **18**, 1994–2004

26. Y.-P. Wang, H.-L. Leu, H.-Y. Cheng, T.-S. Lin, Y. Wang and G.-H. Lee, *J. Organomet. Chem.*, 2008, **693**, 2615–2623

27. L. A. Berben and S. A. Kozimor, *Inorg. Chem.*, 2008, **47**, 4639–4647

28. W. A. Hoffert, A. K. Rappe and M. P. Shores, *Inorg. Chem.*, 2010, **49**, 9497–9507

29. C. Egler-Lucas, O. Blacque, K. Venkatesan, A. López-Hernández and H. Berke, *Eur. J. Inorg. Chem.*, 2012, **2012**, 1536–1545

30. A. López-Hernández, K. Venkatesan, H. W. Schmalle and H. Berke, *Monatsh. Chem.*, 2009, **140**, 845–857

31. R. W. Hay, N. F. Curtis and G. A. Lawrance, *J. Chem. Soc., Perkin Trans. 1*, 1975, 591–593

32. D. A. House, R. W. Hay and M. A. Ali, *Inorg. Chim. Acta*, 1983, **72**, 239–245

33. N.-H. Chang, H. Mori, X.-C. Chen, Y. Okuda, T. Okamoto and Y. Nishihara, *Chem. Lett.*, 2013, **42**, 1257–1259

34. G. Brizius and U. H. F. Bunz, *Org. Lett.*, 2002, **4**, 2829–2831

35. D. Lehnherr, J. M. Alzola, E. B. Lobkovsky and W. R. Dichtel, *Chem. – Eur. J.*, 2015, **21**, 18122–18127

36. D. F. Evans, *J. Chem. Soc.*, 1959, 2003–2005

37. D. L. Grisenti, W. W. Thomas, C. R. Turlington, M. D. Newsom, C. J. Priedemann, D. G. VanDerveer and P. S. Wagenknecht, *Inorg. Chem.*, 2008, **47**, 11452–11454

38. J. Manna, K. D. John and M. D. Hopkins, *Adv. Organomet. Chem.*, 1995, **38**, 79–154

39. N. A. P. Kane-Maguire Photochemistry and Photophysics of Coordination Compounds: Chromium, *Photochemistry and Photophysics of Coordination Compounds I*, V. Balzani and S. Campagna, Springer, Berlin, Heidelberg, 2007

40. A. F. Fucaloro, L. S. Forster, S. G. Glover and A. D. Kirk, *Inorg. Chem.*, 1985, **24**, 4242–4246

41. R. B. Lessard, M. J. Heeg, T. Buranda, M. W. Perkovic, C. L. Schwarz, R. Yang and J. F. Endicott, *Inorg. Chem.*, 1992, **31**, 3091–3103

42. L. S. Forster *Chem. Rev.*, 1990, **90**, 331–353

43. Nonius (1998). Collect Users Manual, Nonius Delft, The Netherlands

44. Z. Otwinowski and W. Minor, *Methods Enzymol.*, 1997, **276**, 307–326

45. P. T. Beurskens, G. Beurskens, R. deGelder, S. Garcia-Granda, R. O. Gould, J. M. M. Smits, *The DIRDIF2008 Program System*, Crystallography Laboratory, University of Nijmegen, The Netherlands: 2008

46. Bruker (2016). Apex3 v2018.7-2, v2019.1-0, SAINT V8.38A, Bruker AXS Inc.: Madison (WI), USA, 2013/2014

47. SHELXTL suite of programs Version 6.14. Bruker Advanced X-ray Solutions. Bruker AXS Inc. 2000-2003, Madison, Wisconsin: USA

48. G. M. Sheldrick, *Acta Cryst. A.*, 2008, **64**, 112–122

49. C. B. Hübschle, G. M. Sheldrick and B. Dittrich, *J. Appl. Crystallogr.*, 2011, **44**, 1281–1284

50. G. M. Sheldrick, *University of Göttingen, Germany*, 2016

51. G. M. Sheldrick, *Crystallogr. Sect. C Struct. Chem.*, 2015, **71**, 3–8

CHAPTER 4. CHROMIUM(III) BIS-ALKYNYL COMPLEXES SUPPORTED BY *C*-SUBSTITUTED CYCLAM MPC

Submitted to Journal of Organometallic Chemistry. A. J. Schuman, M. M. Mills, L. A. Miller-Clark and T. Ren.

4.1 Abstract

Macrocyclic Cr^{III} bis-alkynyl complexes have recently been used as a precursor in the synthesis of mono-alkynyl complexes, which can serve as synthetic intermediates towards the formation of dissymmetric bis-alkynyl complexes. The *trans* stereochemistry is essential to generate stable macrocyclic Cr^{III} mono-alkynyl complexes, however, previously explored cyclam (1,4,8,11-tetraazacyclotetradecane) and its derivatives heavily favor the *cis* isomer after Cr insertion. The *C*-substituted cyclam MPC (5,12-dimethyl-7,14-diphenyl-1,4,8,11-tetraazacyclotetradecane) has shown a noteworthy preference towards the *trans* isomer upon insertion of Cr, making it desirable for the pursuit of dissymmetric bis-alkynyl complexes in significant quantity. Reported herein are the synthesis and characterization of *trans*-$[Cr(MPC)(C_2Ar)_2]^+$ complexes, where Ar is Ph (**4.1**), Np (**4.2**), or $C_6H_4{}^tBu$ (**4.3**). Complexes **4.1** – **4.3** have structural and optical properties similar to previous Cr^{III} bis-alkynyl complexes based on single-crystal X-ray diffraction, UV-vis and phosphorescence spectroscopical characterizations.

4.2 Introduction

Transition-metal alkynyl complexes have attracted interest for applications as molecular wires, molecular memory devices, and optoelectronic materials due to their π-delocalization, redox activity of the metal center, and ease of synthesis.[1-4] Based on donor-bridge-acceptor (D–B–A) complexes containing a *trans*-Pt^{II}-bis-alkynyl bridge, it has been demonstrated recently that the evolution of photo-induced electron transfer (PET) states, notably the formation of the charge-separated (CS) state, can be attenuated by vibrational excitation of the Pt bound C≡C bonds.[5,6] In an effort to expand D–B–A alkynyl chemistry to include more sustainable 3d metals, our group has investigated the PET properties of *trans*-$[Co(cyclam)(C_2NAP^{iPr})(C_2D)]^+$ complexes (cyclam = 1,4,8,11-tetraazacyclotetradecane; D = C_6H_4-4-NMe_2, Ph, or C_6H_4-4-N(4-MeOPh)$_2$).[7,8] Femtosecond transient absorption and time-resolved IR spectroscopic studies revealed the

formation of desirable CS states; however, they were quickly deactivated by the low-lying Co-centered triplet state. Thus, there is a need to further investigate other D–B–A dyads with macrocyclic 3d metal bridges that could potentially sustain long-lived CS and metal-to-ligand charge transfer states.

Macrocyclic chromium alkynyl chemistry emerged with Taube and co-workers' $[Cr^{III}(phthalocyanine)(C_2Ph)_2]^-$ complex[9] in the late 70's and has gained traction over the past few decades. Several $Cr^{III}(Me_3TACN)(C_2R)_3$ complexes (Me_3TACN = *N,N',N''*-trimethyl-1-4-7-triazacyclononane; R = C_2SiMe_3, C_2H, C_4SiMe_3, C_4H) and Cr^{III}(cyclam) bis-alkynyl complexes *trans*-$[Cr(cyclam)(C_2R)_2]^+$ (R = C_2SiMe_3, C_2H, 1,3-$C_2C_6H_4C_2H$) were reported by Berben and Long.[10,11] The groups of Wagenknecht,[12-14] Nishijo,[15-18] and Ren[19] have documented additional Cr^{III}(cyclam) bis-alkynyl complexes. To date, all examples of macrocyclic Cr^{III} alkynyl complexes feature symmetric alkynyl ligands, while D–B–A type complexes remain elusive. D–B–A complexes may be accessed in a stepwise manner, as shown in Scheme 4.1: a mono-alkynyl intermediate is generated, followed by subsequent addition of a different alkynyl ligand. There are limited literature examples of Cr mono-alkynyl complexes that can undergo further alkynylation. Berke and co-workers' Cr^{II} and Cr^{III} *trans*-$[Cr(dmpe)_2(C_2R)_2]^n$ complexes (R = C_2Ph, $SiMe_3$, $SiEt_3$, and C_2SiMe_3; n = 0, 1)[20] and our *trans*-$[Cr^{III}(HMC)(C_2Ar)Cl]^+$ complexes (HMC = 5,5,7,12,12,14-hexamethyl-1,4,8,11-tetraazacyclotetradecane; Ar = Ph, Np (naphthalene), $C_6H_4{}^tBu$, and 3,5-$Cl_2C_6H_3$)[21] are both viable candidates. Although the analogous *cis*-Cr(HMC) mono-alkynyl complexes can be prepared,[22] they are less robust in solution than the *trans* isomer, demonstrating the need for isomeric control of the reactions in the pursuit of D–B–A complexes. The supporting macrocyclic ligand plays an essential role in determining the stereochemistry of these complexes and further fine-tuning should be pursued.

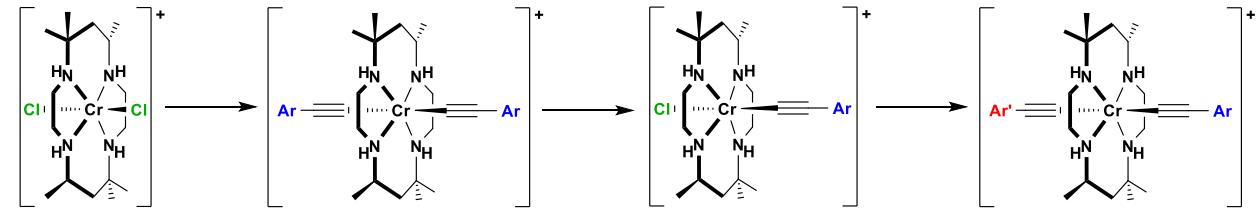

Scheme 4.1. Synthetic pathway for macrocyclic Cr^{III} alkynyl complexes.

The synthesis of *C*-substituted tetraazamacrocycles has been discussed in-depth in the work of Curtis,[23-25] Lloyd,[26,27] and Hay.[28] Our group has previously explored Cr^{III}(cyclam') alkynyl complexes, where cyclam' is the *C*-substituted cyclam derivative HMC or DMC (5,12-dimethyl-1,4,8,11-tetraazacyclotetradecane).[29-31] In contrast to cyclam, HMC and DMC are inexpensive to synthesize and allow for the facile separation of *cis/trans*-[Cr(cyclam')Cl_2]Cl starting materials. HMC and DMC heavily favor the generation of *cis*-[Cr(cyclam')Cl_2]Cl upon Cr insertion, with DMC producing a 9:1 ratio of *cis/trans* isomers.[30] Although the *trans* stereochemistry of *trans*-[Cr(HMC)Cl_2]$^+$ is retained throughout the synthesis of *trans*-[Cr(HMC)(C_2Ar)$_2$]$^+$ and *trans*-[Cr(HMC)(C_2Ar)Cl]$^+$,[21,29] the low yield of *trans* starting material limits its potential to produce D–B–A complexes in practical quantities. Initial interest in the MPC (5,12-dimethyl-7,14-diphenyl-1,4,8,11-tetraazacyclotetradecane) ligand in our laboratory stems from the use of its Ni(II) complex as a electrocatalyst for CO_2 reduction.[32] Subsequently, alkynyl complexes based on Co^{III}(MPC) were investigated and the MPC ligand was noted for enabling an energy order of $d_{x^2-y^2} < d_{z^2}$, which led to (quasi)reversible Co(III/II) reduction.[33,34] Ford and co-workers reported the synthesis of *cis/trans*-[Cr(MPC)Cl_2]Cl.[35] The aforementioned starting material has a significant preference for the *trans* isomer after Cr insertion (7:1), making Cr(MPC) a worthwhile ligand framework to pursue in the synthesis of D–B–A complexes. Herein, we report the alkynylation of *trans*-[Cr(MPC)Cl_2]$^+$ (Scheme 4.2) to generate the novel bis-alkynyl complexes *trans*-[Cr(MPC)(C_2Ar)$_2$]$^+$, where Ar = Ph (**4.1**), Np (**4.2**), and $C_6H_4{}^t$Bu (**4.3**).

4.3 Results and Discussion

4.3.1 Synthesis

Complexes **4.1** – **4.3** were synthesized as depicted in Scheme 4.2. *trans*-[Cr(MPC)Cl_2]X (X = Cl^- or PF_6^-) was dried in vacuo and reacted with 5 equivalents of the appropriate lithiated arylalkynyl ligand, LiC_2Ar, in THF. After 2 hours, the reaction was quenched in air and purified over a silica gel plug. In general, the desired product band was collected and a solid was obtained upon trituration with Et_2O. Recrystallization from minimal CH_2Cl_2 and Et_2O afforded yellow crystals of *trans*-[Cr(MPC)(C_2Ph)$_2$]Cl (**4.1**) and *trans*-[Cr(MPC)($C_2C_6H_4{}^t$Bu)$_2$]PF_6 (**4.3**), and orange crystals of *trans*-[Cr(MPC)(C_2Np)$_2$]Cl (**4.2**), with yields ranging between 41-57%. The characteristic ν(C≡C) peak observed in the FTIR spectra indicated the successful incorporation of

the alkynyl ligands. The identity and purity of complexes **4.1** – **4.3** were verified by ESI-MS and elemental analysis.

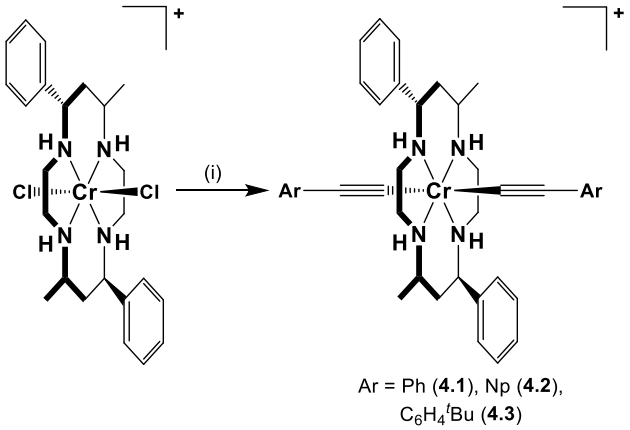

Scheme 4.2. Synthesis of trans-[Cr(MPC)(C_2Ar)$_2$]$^+$ complexes. Conditions: (i) 5 equiv LiC_2Ar in THF, 2 h.

4.3.2 Molecular Structures

Complexes **4.1** – **4.3** have been characterized with single crystal X-ray diffraction. The cations were crystallized as the chloride [**4.1**]$^+$, chloride/nitrate [**4.2**]$^+$, and hexafluorophosphate [**4.3**]$^+$ salts. Selected bond lengths and angles are provided in Table 4.1 and the molecular structures are shown in Figures 4.1–4.3. All complexes have pseudo-octahedral geometry and the bis-alkynyl products retain the *trans* stereochemistry of the starting material. The MPC macrocycle adopts the C-*meso* configuration, while the macrocyclic N centers adopt a *trans-III* configuration (*R,R,S,S*), as depicted in Figures 4.S1–4.S3. Complexes **4.1** – **4.3** all contain a crystallographic inversion center.

The obtained crystal structure for **4.2** contained 50:50 counteranion disorder between Cl^- and NO_3^-. The origin of the NO_3^- is unclear and its inclusion likely became more pronounced during crystal growth. Elemental analysis of **4.2** after initial recrystallization did not indicate a significant nitrate impurity. Because the counteranion has minimal to no observed effect on the resulting optical properties, we proceeded with characterization. To minimize the chance of future counteranion impurities, a PF_6^- counteranion exchange was performed on the *trans*-[Cr(MPC)Cl_2]Cl starting material before the synthesis of complex **4.3**.

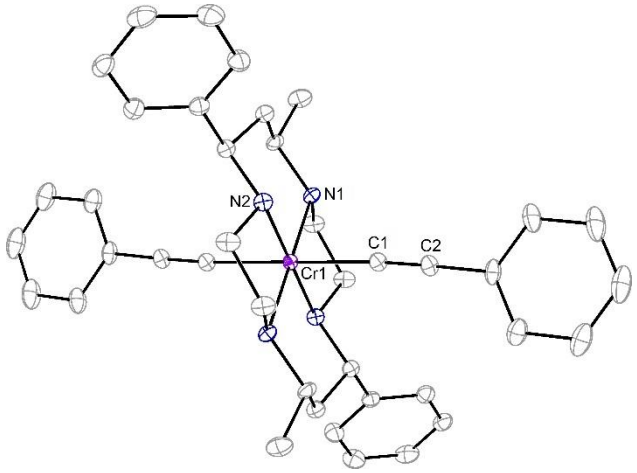

Figure 4.1. ORTEP plot of [**4.1**]$^{+}$ at 30% probability level. H atoms and the Cl^{-} counterion were omitted for clarity.

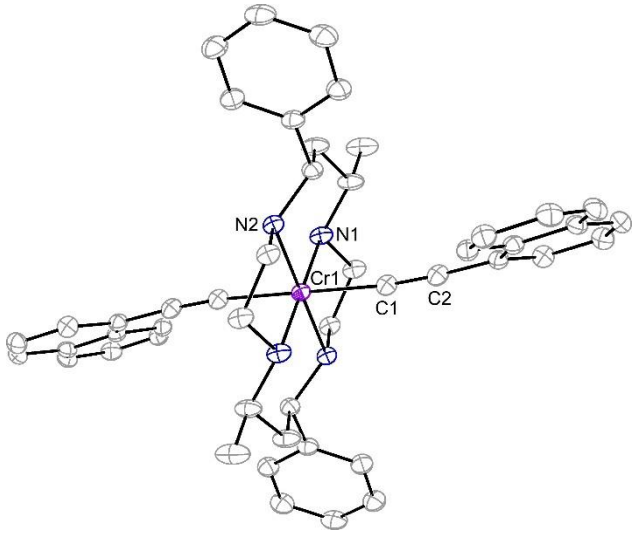

Figure 4.2. ORTEP plot of [**4.2**]$^{+}$ at 30% probability level. H atoms and disordered counterions (Cl^{-} and NO_3^{-}) were omitted for clarity.

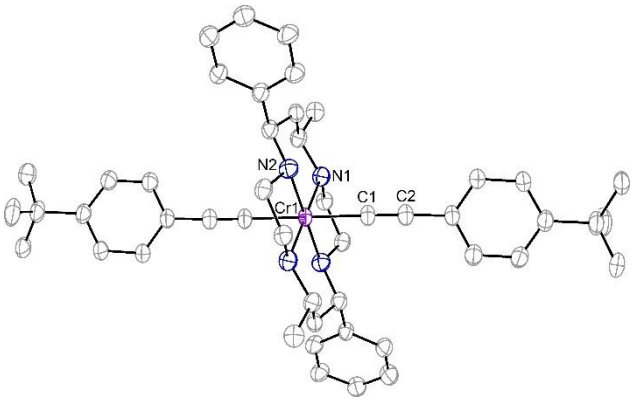

Figure 4.3 ORTEP plot of [**4.3**]$^+$ at 30% probability level. H atoms, PF_6^- counterion, and disorder were omitted for clarity.

The Cr–C bond length of 2.079(2) Å in **4.1** is comparable to those observed for *trans*-[Cr(cyclam)($C_2Ph)_2$]$^+$ (*avg.* 2.073 Å),[12] *trans*-[Cr(HMC)($C_2Ph)_2$]Cl (*avg*. 2.085 Å),[29] and *trans*-[Cr(DMC)($C_2Ph)_2$]$^+$ (2.089(2) Å).[30] This trend is expected, as there is a distinct *trans*-influence experienced by the two alkynyl ligands.[12,29] A similar trend is observed for **4.2** with a Cr–C bond length of 2.067(3) Å, while the average of those for *trans*-[Cr(HMC)($C_2Np)_2$]Cl is 2.078 Å.[31] The Cr–C bond length of 2.059(3) Å in **4.3** is significantly shorter than *trans*-[Cr(HMC)($C_2C_6H_4{}^tBu)_2$]OTf (*avg*. 2.104 Å),[21] and slightly shorter than complexes **4.1** and **4.2**, despite the arylalkynyl ligand bearing an electron donating group. This is likely attributed to variation in the positions of the para-*tert*-butylphenylacetylide ligands. In **3**, the Cr1–C1–C2 bond angle is close to linearity at 177.4(3)°, while the HMC analogue has more distorted Cr–C–C angles of 172.4(5)° and 170.6(4)°.[21] Complex **4.3** is also more linear than **4.1** and **4.2**, with respective Cr–C–C bond angles of 173.9(2)° and 174.1(3)°.

For complexes **4.1** – **4.3**, the C≡C bonds fall within the observed range (1.150 – 1.225 Å, esd ≤ 0.010 Å) for complexes containing MC≡CR (R = C, Si) bonds.[36] The C≡C bond lengths of **4.1** – **4.3** are comparable to one another, as well as to the corresponding bis-alkynyl complexes with cyclam, DMC, and HMC macrocycles.[12,21,29–31]

Table 4.1. Selected bond lengths (Å) and bond angles (°) for **4.1** – **4.3**.

	4.1[a]	**4.2**	**4.3**[a]
Cr1–N1	2.079(2)	2.080(2)	2.085(4)
Cr1–N2	2.080(2)	2.096(2)	2.081(3)
Cr1–C1	2.076(2)	2.067(3)	2.059(3)
C1–C2	1.214(3)	1.215(4)	1.202(5)
Cr1–C1–C2	173.9(2)	174.1(3)	177.4(3)
N1–Cr1–N1'	180.0	180.0	180.0
N2–Cr1–N2'	180.0	180.0	180.0
N1–Cr1–N2	94.24(9)	86.36(8)	95.02(14)
N1–Cr1–N2'	85.76(9)	93.64(8)	84.98(14)

[a]The unit cell revealed two (4.1) or four (4.3) crystallographically independent moities; geometric parameters for only one of them are listed here.

4.3.3 UV-vis Spectroscopic Analysis

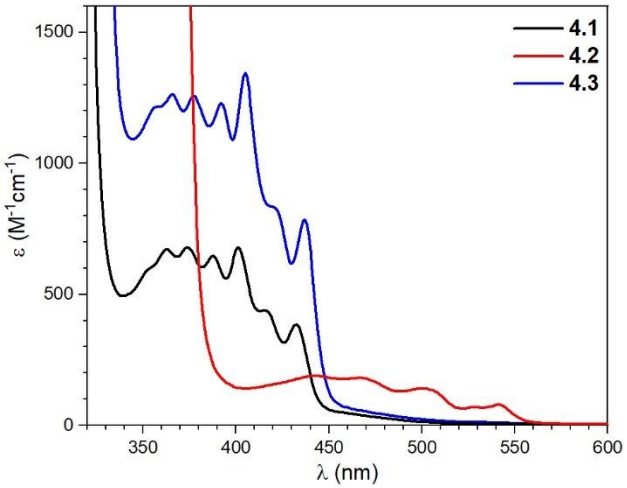

Figure 4.4. UV-vis absorption spectra of **4.1** – **4.3** as CH_2Cl_2 solutions.

The UV-vis absorption spectra of **4.1** – **4.3** are shown in Figure 4.4. Structured d–d bands are observed between 350–450 nm for **4.1** and **4.3**, and between 400–560 nm for **4.2**. A bathochromic shift of **4.2** is observed due to increased aromaticity of the ethynylnapthalene ligand, which was previously noted for the analogous cyclam and HMC complexes.[13,31] The absorption has been assigned to the $^4A_{2g} \rightarrow {}^4T_{1g}/{}^4T_{2g}$ (O_h) transition. The extinction coefficients for the d–d

bands of complexes **4.1** – **4.3** are high in comparison to *trans*-[Cr(MPC)Cl_2]Cl,[35] supporting the presumption of partial charge-transfer character due to dπ-π(C≡C) mixing.[29] Intense absorptions below 330 nm (not shown) are associated with intraligand π-π* and charge transfer transitions. The $^4T_{1g}$ term typically observed in *trans*-[Cr(cyclam')Cl_2]$^+$ complexes is likely hidden beneath the charge transfer bands or beyond the UV-vis window[29] because the replacement of a halide with an alkynyl ligand leads to a stronger ligand field.

The origin of the highly-structured d–d bands may be determined from the vibronic spacing of the absorption spectra. The calculated vibronic progressions of complexes **4.1** – **4.3** are found in Table 4.S2. The average spacing of **4.1** and **4.3** are 872 and 841 cm^{-1}, respectively, which are consistent with aromatic out-of-plane C–H bending.[14] The irregularly spaced vibronic progressions of **4.2** have an average spacing of 1090 cm^{-1}, which closely aligns with phenyl ring deformations of the Np ligand or aromatic C=C stretching modes.[31]

4.3.4 Emission Studies

The emissive nature of Cr^{III} complexes is well established.[37] For the pseudo-octahedral Cr^{III} complexes **4.1** – **4.3**, phosphorescence can occur as a result of intersystem crossing from the $^4T_{1g}$ or $^4T_{2g}$ excited states to two possible lower-lying doublet states, $^2T_{1g}$ and ^2E_g.[38] Emission spectra of **4.1** – **4.3** are displayed in Figure 4.5 and relevant parameters are compiled in Table 4.2. The spectra exhibit fine structuring at 77 K with emission centered around 750 nm, which is red-shifted from the 650–710 nm range observed for traditional $^2E_g \rightarrow {}^4A_{2g}$ emitters.[39] The room temperature emission spectra are broad and structureless, which is indicative of $^2T_{1g}$ (O_h) emission. Based on these findings, the observed emission has been assigned as $^2T_{1g} \rightarrow {}^4A_{2g}$ (O_h). A secondary transition is observed in the spectra of **4.2** and **4.3** at 77 K, which has been previously observed for *trans*-[Cr(HMC)(C_2Np)$_2$]$^+$ and *trans*-[Cr(HMC)($C_2C_6H_4{}^t$Bu)$_2$]$^+$ and has been assigned to a $^2E_g \rightarrow {}^4A_{2g}$ (O_h) transition. The room temperature spectra do not exhibit ^2E_g (O_h) emission. Although a strong 0–0 transition should be forbidden for a centrosymmetric complex,[37] it is likely that rotation of the ethynylnapthalene and para-*tert*-butylphenylacetylide ligands induce enough asymmetry to make the transition more allowed.[14,30] The fine structuring observed in the phosphorescence spectra of **4.1** – **4.3** at 77 K is believed to be of vibronic origin.[40] Because the *trans* influence results in elongated Cr–C bonds, bis-alkynyl complexes exhibit less structured

emission spectra than mono-alkynyl *trans*-[Cr(HMC)(C_2Ar)Cl]$^+$ type complexes due to weaker vibronic coupling.[21]

At 77 K, complexes **4.1** – **4.3** exhibit phosphorescence lifetimes of 369 μs, 333 μs, and 372 μs, respectively. The lifetimes were calculated from decay curves generated by measuring the emission intensity at increasing delay times (Figures 4.S4 – 4.S9). The room temperature lifetimes are significantly reduced, with lifetimes of 130 μs, 60 μs, and 56 μs for **4.1** – **4.3**, respectively. The phosphorescence lifetimes at 77 K and room temperature of complexes **4.1** – **4.3** are of similar magnitude to previously reported HMC and DMC Cr^{III} bis-alkynyl complexes.[21,29-31]

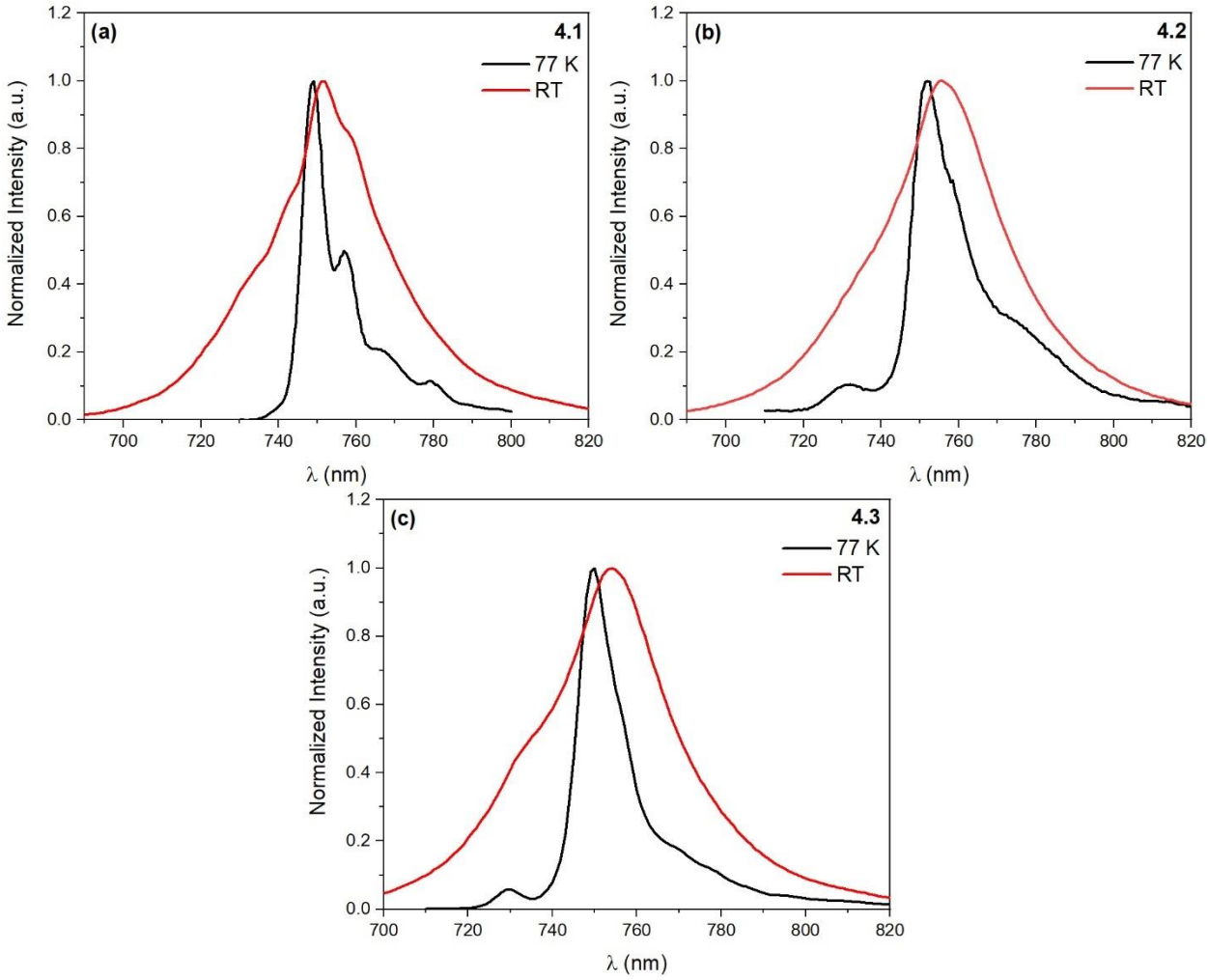

Figure 4.5. Emission spectra of (a) **4.1**, (b) **4.2**, and (c) **4.3** at 77 K in 4:1 EtOH:MeOH and room temperature in degassed MeCN.

Table 4.2. Photophysical data for complexes **4.1** – **4.3**.

	Frozen Glass [a]			*Room Temperature* [b]		
	λ_{ex} (nm)	λ_{em} (nm)	τ (μs)	λ_{ex} (nm)	λ_{em} (nm)	τ (μs)
4.1	405	749	369	405	752	130
4.2	466	752	333	466	755	60
		732[c]	206			
4.3	406	750	372	406	754	56
		730 [c]	316			

[a] Measured at 77 K in a 4:1 EtOH/MeOH glass
[b] Measured at room temperature in degassed MeCN
[c] $^2E_g \rightarrow {}^4A_{2g}$ emission

4.4 Conclusion

An advantage of MPC over previously employed tetraazamacrocycles is that it favors the *trans* isomer upon insertion of Cr^{III}, resulting in higher yields of *trans*-$[Cr(MPC)Cl_2]^+$ starting material, and thus higher quantities of *trans*-$[Cr(MPC)(C_2Ar)_2]^+$ after alkynylation. Tuning the macrocyclic ligand framework afforded bis-alkynyl complexes with similar properties to the previously reported Cr^{III} cyclam and cyclam' analogues, but in larger quantity. The increased amount of *trans*-$[Cr(MPC)(C_2Ar)^2]^+$ will aid the further pursuit of a dissymmetric Cr^{III} bis-alkynyl complex, which will allow for further study of PET processes in 3d metal alkynyl complexes.

4.5 Experimental Section

Materials. Phenylacetylene was purchased from Oakwood Chemical and used without further purification. MPC,[27] TMS-C_2Np,[41] and TMS-$C_2C_6H_4{}^t$Bu,[42] were prepared according to literature procedures. An adapted literature procedure[43] was used to generate *trans*-$[Cr(MPC)Cl_2]Cl$[35] as further described in Section 4.6.1. The *trans*-$[Cr(MPC)Cl_2]PF_6$ analogue was synthesized from *trans*-$[Cr(MPC)Cl_2]Cl$ via anion exchange with aqueous KPF_6 followed by an extraction into CH_2Cl_2. Tetrahydrofuran was freshly distilled over Na/benzophenone. The

preparation of **4.1** – **4.3** was performed under a dry N_2 atmosphere using standard Schlenk procedures and the resulting complexes were purified under ambient conditions.

Physical Measurements. ESI-MS were analyzed on an Advion Mass Spectrometer. Elemental analysis was performed by Atlantic Microlab, Inc. in Norcross, GA. UV-vis spectra were obtained with a JASCO V-670 spectrophotometer as CH_2Cl_2 solutions. Emission data were recorded on a Varian Cary Eclipse fluorescence spectrophotometer. FT-IR spectra were measured as neat samples with a JASCO FT/IR-6300 spectrometer equipped with an ATR accessory.

Synthesis of *trans*-[Cr(MPC)(C_2Ph)$_2$]Cl (4.1). A suspension of *trans*-[Cr(MPC)Cl_2]Cl (0.20 g, 0.37 mmol) in 30 mL THF was combined with 5 equiv of LiC_2Ph (prepared from 1.9 mmol HC_2Ph in THF and 2.5 mmol *n*-BuLi). The reaction mixture was stirred for 2 h at room temperature. After quenching the reaction in air, solvent was removed via rotary evaporation. A silica gel plug was used for purification and **4.1** was eluted with 9:1 CH_2Cl_2:MeOH to afford 0.14 g of a yellow solid (57% yield based on Cr). Single crystals suitable for X-ray diffraction were grown from slow diffusion of Et_2O into MeCN. Elem. Anal. Found (Calcd) for *trans*-[Cr(MPC)(C_2Ph)$_2$]Cl·2H_2O: C, 67.85 (68.02); H, 6.85 (7.13); N, 7.86 (7.93). UV-vis, λ_{max} / nm (ε / $M^{-1}cm^{-1}$): 353 (600), 362 (670), 374 (680), 388 (650), 402 (670), 416 (440), 433 (380). FT-IR ν(C≡C) / cm^{-1}: 2082*w*. ESI-MS [M^+]: 634 *m/z* for the cationic species [**4.1**]$^+$.

Synthesis of *trans*-[Cr(MPC)(C_2Np)$_2$]Cl (4.2). A suspension of *trans*-[Cr(MPC)Cl_2]Cl (0.25 g, 0.46 mmol) in 30 mL THF was combined with 5 equiv of LiC_2Np (prepared from 2.32 mmol TMS-C_2Np in THF and 3.0 mmol *n*-BuLi). The reaction mixture was stirred for 2 h at room temperature. After quenching the reaction in air, solvent was removed via rotary evaporation. A silica gel plug was used for purification and **4.2** was eluted with 9:1 CH_2Cl_2:MeOH to afford 0.15 g of an orange solid (41% yield based on Cr). Complex **4.2** was further purified by recrystallization from minimal CH_2Cl_2 and Et_2O. Single crystals suitable for X-ray diffraction were grown from vapor diffusion of Et_2O into MeOH. Elem. Anal. Found (Calcd) for *trans*-[Cr(MPC)(C_2Np)$_2$]Cl·1.5CH_2Cl_2·1Et_2O: C, 62.82 (62.62); H, 6.56 (6.93); N, 6.42 (6.42). UV-vis, λ_{max} / nm (ε / $M^{-1}cm^{-1}$): 439 (190), 468 (180), 502 (140), 528 (70), 543 (80). FT-IR ν(C≡C) / cm^{-1}: 2071*w*. ESI-MS [M^+]: 734 *m/z* for the cationic species [**4.2**]$^+$.

Synthesis of *trans*-[Cr(MPC)($C_2C_6H_4{}^tBu$)$_2$]PF_6 (4.3). A suspension of *trans*-[Cr(MPC)Cl_2]PF_6 (0.250 g, 0.39 mmol) was generated upon the addition of 25 mL THF and 5 equiv of H$C_2C_6H_4{}^t$Bu (0.34 g, 1.93 mmol). A dry ice-acetone bath was used to cool the flask, and

then 1.0 mL (2.5 mmol) 2.5 M *n*-BuLi was added. The reaction mixture was stirred for 2 h at room temperature. After quenching the reaction in air, solvent was removed via rotary evaporation. A silica gel plug was used for purification and **4.3** was eluted with 9:1 CH_2Cl_2:MeOH to afford 0.18 g of a yellow solid (53% yield based on Cr). Single crystals suitable for X-ray diffraction were grown from slow diffusion of Et_2O into MeOH. Elem. Anal. Found (Calcd) for *trans*-[Cr(MPC)($C_2C_6H_4{}^tBu)_2$]PF_6: C, 62.31 (62.12); H, 7.08 (7.06); N, 5.76 (6.04). UV-vis, λ_{max} / nm (ε / $M^{-1}cm^{-1}$): 358 (1210), 366 (1260), 377 (1260), 392 (1240), 405 (1340), 419 (830), 437 (780). FT-IR ν(C≡C) / cm^{-1}: 2082*w*. ESI-MS [M^+]: 746 *m/z* for the cationic species [**4.3**]$^+$.

X-ray crystallographic analysis. Single crystal X-ray data were collected at 150 K on a Bruker Quest diffractometer with kappa geometry, an I-μ-S microsource X-ray tube, laterally graded Goebel mirror for monochromatization, a Photon-II (**4.1** and **4.2**) or Photon-III (**4.3**) area detector and an Oxford Cryosystems low temperature device with CuKα (λ = 1.54178 Å) radiation. Data for **4.1**, **4.2**, and **4.3** were collected and processed using APEX3[44] and reduced using SAINT[44], space groups were assigned using XPREP within the SHELXTL[45] suite of programs and solved using ShelXS.[46] All structures were refined using Shelx2018 and the graphical interface Shelxle.[47,48] Further refinement details and crystal data are provided in Section 4.6.2.

Crystallographic data for the structural analysis have been deposited with the Cambridge Crystallographic Data Center, CCDC 2083346 – 2083348 for complexes **4.1** – **4.3**, respectively. Copies of this information may be obtained free of charge from, The Director, CCDC, 12 Union Road, Cambridge CB2 1EZ, UK, (Fax: þ44-1233-336033; email: deposit@ccdc.cam.ac.uk or www: http://ccdc.cam.ac.uk).

4.6 Supporting Information

4.6.1 Synthetic Details

***trans*-[Cr(MPC)Cl_2]Cl.** A modified procedure was used to synthesize *cis/trans*-[Cr(MPC)Cl_2]Cl,[35] adapted from the synthesis of *cis/trans*-[Cr(HMC)Cl_2]Cl.[43] Because the Cr insertion into MPC would not proceed in open atmosphere, the reaction occurred under N_2 with mossy Zn employed as reducing agent. The resulting complex was oxidized upon exposure to air. A solution of $CrCl_3$·3DMF was generated by refluxing 0.70 g $CrCl_3$·$6H_2O$ (2.6 mmol) in 20 mL DMF in open atmosphere until the volume was reduced to ~10 mL. During the reflux, a color

change from green to purple was observed, indicating loss of H_2O. The flask was placed under N_2 with gentle heating for 30 minutes.

A suspension of MPC was created by combining 1.0 g (2.6 mmol) MPC with 20 mL DMF (previously dried over molecular sieves) in a 3-neck round bottom flask. A piece of mossy Zn (~0.5 g) was added. The flask was purged with N_2 for 30 minutes and brought to a reflux.

The warm solution of $CrCl_3 \cdot 3DMF$ was transferred into the refluxing solution of MPC and stirred under N_2 for 12 hours until a purple solution formed. The solution was filtered over celite and a reddish-purple filtrate was obtained. The filtrate was heated to remove excess DMF. Upon the addition of DCM, puce colored microcrystals began to form. After filtering, 793 mg of *trans*-$[Cr(MPC)Cl_2]Cl$ was obtained (56% yield based on Cr). The identity of the crystals was confirmed to be $[Cr(MPC)Cl_2]^+$ using mass spec (M^+, 502 m/z) and the *trans* isomer was confirmed via UV-vis spectroscopy.

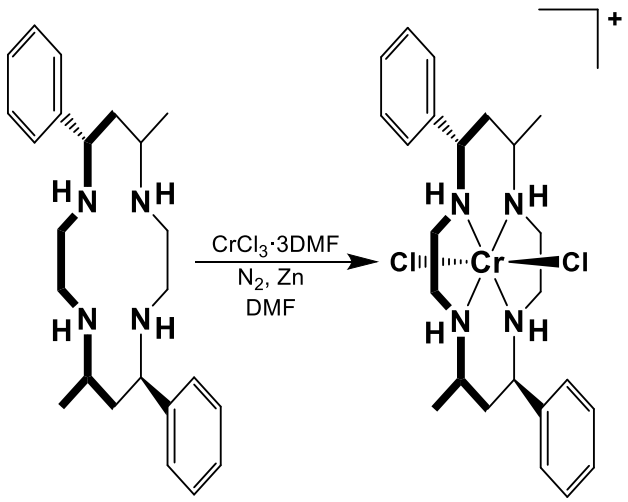

Scheme 4.S1. Synthesis of *trans*-$[Cr(MPC)Cl_2]Cl$.

4.6.2 X-ray Crystallographic Details

If not specified otherwise, H atoms attached to carbon and nitrogen atoms, as well as hydroxyl hydrogens, were positioned geometrically and constrained to ride on their parent atoms. C–H bond distances were constrained to 0.95 Å for aromatic, and to 1.00, 0.99 and 0.98 Å for aliphatic C–H, CH_2 and CH_3 moieties, respectively. O–H distances of alcohols were constrained to 0.84 Å. Ammonium N–H distances were freely refined. Methyl CH_3 and hydroxyl H atoms

were allowed to rotate but not to tip to best fit the experimental electron density. U_{iso}(H) values were set to a multiple of U_{eq}(C/N/O) with 1.5 for CH_3 and OH, and 1.2 for C–H, CH_2 and N–H units, respectively.

Special refinement details of [1]Cl. The crystal of **4.1** was found to be pseudo-merohedrally twinned with the monoclinic primitive lattice metrically fitting a larger orthorhombic C-centered lattice with parameters a = 15.569, b = 47.719, c = 10.526. The structure was found to be twinned by one of the symmetry elements of the larger orthorhombic setting, which was identified to be a 180° rotation around the a-axis (in both the actual monoclinic setting and the larger orthorhombic setting) using the program Rotax as implemented in the WinGX suite. The twin transformation matrix obtained was:

[1.000 0.000 0.000]
[0.000 -1.000 0.000]
[-0.998 0.000 -1.000]

Refinement as a pseudo-merohedric twin resulted in a close to 1:1 twin ratio (BASF value of 0.398(7).) The twinning is related to partial whole molecule disorder (see below for details). Two cation complexes and two chloride anions are present in the asymmetric part of the Unit cell. Each cation-anion pair is accompanied by each two methanol molecules, and by one water molecule. The water molecule and the chloride anion are 1:1 disordered around inversion centers. Half of each unique complex cation is generated through an inversion center present at the chromium atom.

In addition to the chloride-water disorder the entire structure is also disordered by application of a symmetry element of the larger metrically fitting orthorhombic cell, which transposes the center of the complex cations (the Cr atoms) to alternative centers of inversion (those located between the disordered chloride ions), emulating apparent additional disorder of the chloride ions, requiring refinement of whole molecule disorder. All cation complex C and N atoms were resolved in difference density maps, but geometry restraints as well as restraints for thermal parameters were required for a meaningful and stable refinement of the minor moiety. The positions of the minor moiety water molecules as well as the water H atoms of the major moiety were too ill-defined for meaningful refinement and were omitted.

Major and minor moieties of both cationic complexes were restrained to have similar geometries (SAME command). A SIMU command was used to restrain the U^{ij} components of the

ADPs of all the atoms to be similar. For the minor moiety atoms were also restrained to be close to isotropic (ISOR commands). An EADP command was used to make the ADPs of two disordered chlorines identical. A SADI command was used to restrain distances between the disordered chlorines and disordered water molecules. Subject to these conditions the occupancy ratios refined to 0.912(5) to 0.088(5) (molecule of Cr1 and Cr1B) and 0.913(1) to 0.089(1) (molecule of Cr2 and Cr2B).

Pseudosymmetry was observed related to disorder and twinning. In a hypothetical structure with 1:1 whole molecule disorder, the two molecules of the lattice would have become equivalent, resulting in a 1:1 disordered structure with orthorhombic symmetry in Pbcn with half the volume of the actual monoclinic structure (a = 23.862, b = 7.783, c = 10.526).

Special refinement details of [4.2]Cl/NO_3. The cation [**4.2**]$^+$ is positioned on an inversion center, resulting in a half occupancy of the chromium atom and half of the molecule being generated through symmetry. One methanol solvent species is also observed for each half of the cation.

There is a close to 1:1 anion disorder between a chloride and a nitrate ion, with the Cl and N atom occupying identical positions exactly on an inversion center. The ADPs of the chloride and nitrogen atom in the nitrate were constrained to be identical (EADP command). Inversion symmetry causes disorder by symmetry for the nitrate oxygen atoms. All N-O bonds and all of the distances between O atoms were restrained to be each similar (SADI commands). A SIMU command was used to restrain the U^{ij} components of ADPs of the nitrate atoms to be similar to each other. Subject to these conditions, the occupancy rates refined to 0.525(7) for the Cl ion and to two times 0.237(4) for the two nitrate ion moieties.

Multiple H-bonds were observed using the HTAB command between the nitrate anion and the N–H bonds in the macrocycle, between the nitrate anion and the methanol solvent, and between the methanol solvent and the N-H bonds in the macrocycle.

Special refinement details of [4.3]PF_6. Complex **4.3** was found to be non-merohedrally twinned. The orientation matrices for the two components were identified using the program Cell_Now, with the two components being related by a 90° rotation around the reciprocal a-axis. The two components were integrated using SAINT[44] and corrected for absorption using TWINABS[9], resulting in the following statistics:

36053 data (13321 unique) involve domain 1 only, mean I/sigma 7.9

35995 data (13214 unique) involve domain 2 only, mean I/sigma 3.2

35358 data (14069 unique) involve 2 domains, mean I/sigma 8.8

The exact twin matrix identified by the integration program was found to be:

0.99945 0.29539 0.06283

0.00125 0.00118 0.99442

0.00228 -1.00557 -0.00099

The structure was solved using direct methods with only the non-overlapping reflections of component 1. The structure was refined using the hklf 5 routine with all reflections of component 1 (including the overlapping ones), resulting in a BASF value of 0.238(2).

The R_{int} value given is for all reflections and is based on agreement between observed single and composite intensities and those calculated from refined unique intensities and twin fractions. Four half-molecules of $[Cr(MPC)(C_2Ph^tBu)_2]PF_6$ occupy the unit cell, with Cr1 to Cr4 residing on inversion centers. One of two PF_6^- anions is disordered. The MPC macrocycles of all four cations are disordered, in addition to the ^{t}Bu groups of the Ph^{t}Bu ligands.

Major and minor disordered moieties of the MPC macrocycles (including the phenyl rings) and of the disordered tert-butyl groups were each restrained to have similar geometries. U^{ij} components of the ADPs of disordered atoms were restrained to be similar for atoms closer to each other than 2 Å (SIMU command). The nitrogen atoms were excluded from the disorder (constrained to have identical positions and ADPs using EXYZ and EADP commands). For the first and fourth cation moiety, the minor moiety phenyl groups were constrained to resemble ideal hexagons with C-C bond distances of 1.39 Å (AFIX 66).

In the first moiety, the ^{t}Bu group occupancy ratio refined to be 0.754(7) to 0.246(7). The MPC macrocycle the occupancy ratio refined to 0.743(5) to 0.257(5). In the second moiety, the ^{t}Bu group disorder extends to the phenylene ring. The occupancy ratio refined to be 0.627(12) to 0.373(12). The MPC macrocycle occupancy ratio refined to 0.837(6) to 0.163(6). In the third moiety, the ^{t}Bu group occupancy ratio refined to be 0.45(4) to 0.55(4). The MPC macrocycle occupancy ratio refined to 0.786(6) to 0.214(6). In the fourth moiety, the ^{t}Bu group occupancy ratio refined to be 0.825(7) to 0.175(7). The MPC macrocycle occupancy ratio refined to 0.815(5) to 0.185(5).

The disordered PF_6^- anion was refined to occupy three possible positions. The geometries of the three moieties were restrained to be similar to each other. U^{ij} components of their ADPs

were restrained to be similar (SIMU command). A SUMP command was used to constrain the occupancies of the three components of the ligand to unity. A diethyl ether solvent molecule is located near the disordered PF_6^- anion and is disordered with the least prevalent of the three moieties. A DFIX command was used to restrain equivalent C–O and C–C bond lengths within the molecule to target values of 1.43(2) and 1.53(2) Å, respectively. Subject to these conditions the occupancy rates for the PF_6^- moieties refined to be 0.652(3), 0.1462(19), and 0.202(3).

The structure contains 3 solvent accessible voids of 825 $Å^3$ combined. No substantial electron density peaks were found in the solvent accessible voids (less than 1.7 electron per $Å^3$) and the residual electron density peaks are not arranged in an interpretable pattern. The cif and fcf files were thus corrected for using reverse Fourier transform methods using the SQUEEZE routine[50] as implemented in the program Platon. The resultant files were used in the further refinement. (The FAB file with details of the Squeeze results is appended to the cif file). The Squeeze procedure corrected for 164 electrons within the solvent accessible voids.

Table 4.S1. Crystal data for mono-alkynyl complexes **4.1** – **4.3**.

	4.1	**4.2**	**4.3**
chemical formula	$C_{42}H_{54}ClCrN_4O_{2.91}$	$C_{50}H_{58}Cl_{0.52}CrN_{4.47}O_{3.43}$	$C_{198.83}H_{264.65}Cr_4F_{24}N_{16}O_{1.71}P_4$
fw, g/mol	748.95	847.07	3694.14
space group	$P2_1/n$	$P2_1/c$	$P\bar{1}$
a, Å	15.5664(6)	9.3837(5)	16.574(3)
b, Å	10.5262(4)	11.3301(6)	18.457(3)
c, Å	25.0959(10)	20.3655(11)	18.565(4)
α °	90	90	90.070(7)
β °	108.038(2)	98.104(3)	101.484(6)
γ °	90	90	97.339(8)
V, $Å^3$	3910.0(3)	2143.6(2)	5517.8(17)
Z	4	2	1
T, K	150	150	150
λ, Å	1.54178	1.54178	1.54178
ρ_{calcd}, g/cm^3	1.272	1.312	1.112
R	0.0442	0.0570	0.0721
$R_w(F^2)$	0.1256	0.1401	0.2385

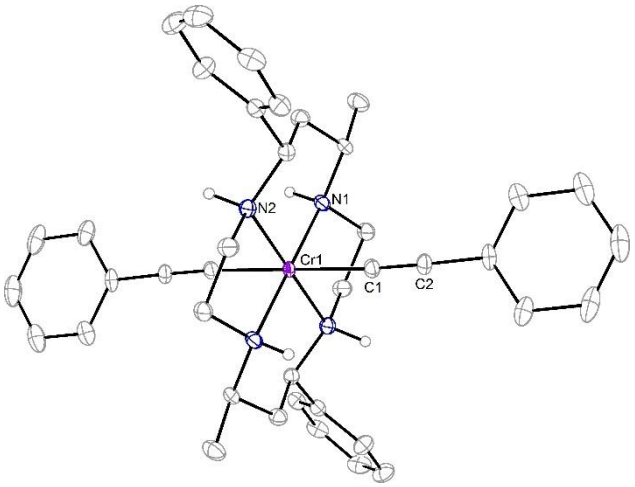

Figure 4.S1. ORTEP plot of [**4.1**]$^{+}$ depicting *trans-III* stereochemistry.

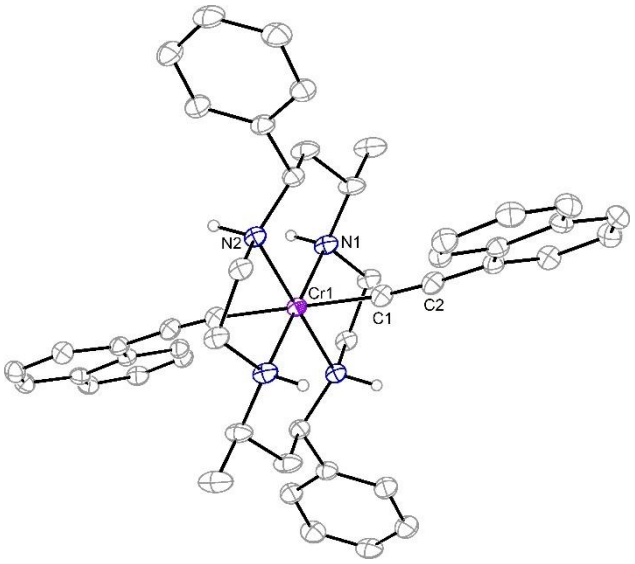

Figure 4.S2. ORTEP plot of [**4.2**]$^{+}$ depicting *trans-III* stereochemistry.

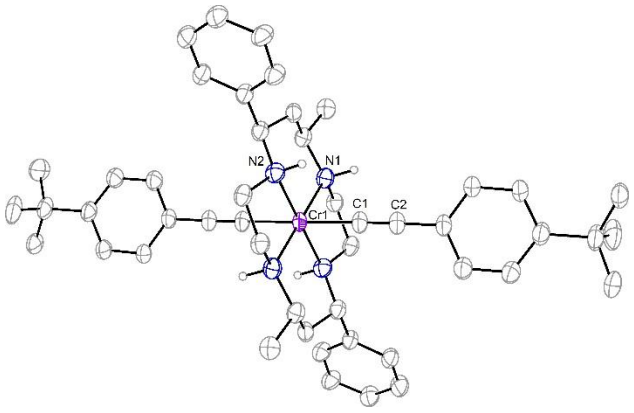

Figure 4.S3. ORTEP plot of [**4.3**]$^{+}$ depicting *trans-III* stereochemistry.

4.6.3 Absorption Details

Table 4.S2. Vibronic progression analysis of **4.1** – **4.3**.

	Peaks Considered, cm^{-1}	**Vibronic Progression, cm^{-1}**
4.1	28328.61 27624.31 26737.97 25773.19 24875.62 24038.46 23094.69	704.30 886.34 964.78 897.57 837.16 943.77
4.2	22779.04 21367.52 19920.32 18939.39 18416.21	1411.52 1447.20 980.93 523.18
4.3	27932.96 27322.40 26525.20 25510.20 24691.36 23866.35 22883.29	610.56 797.20 1015.00 818.84 825.01 983.06

4.6.4 Emission Details

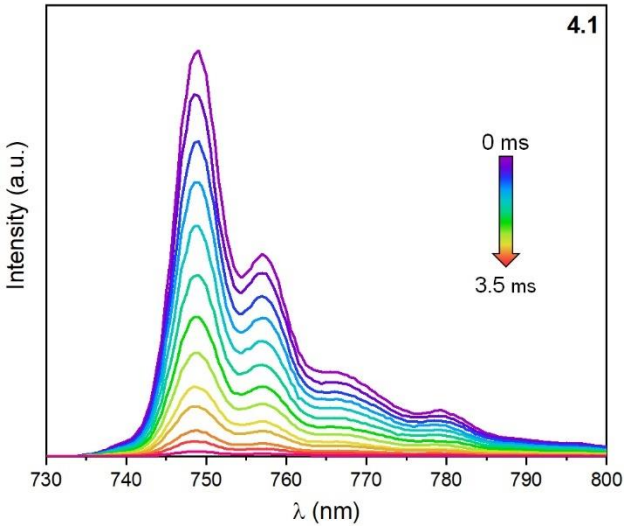

Figure 4.S4. Time-delayed phosphorescence spectrum for **4.1** in 4:1 EtOH:MeOH glass at 77 K and varying delay times.

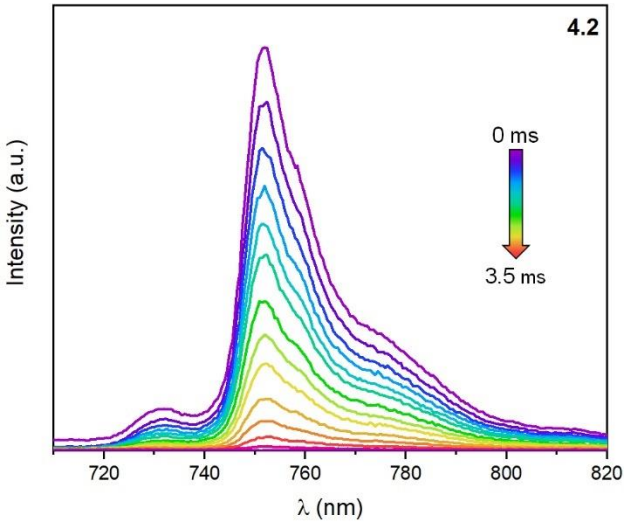

Figure 4.S5. Time-delayed phosphorescence spectrum for **4.2** in 4:1 EtOH:MeOH glass at 77 K and varying delay times.

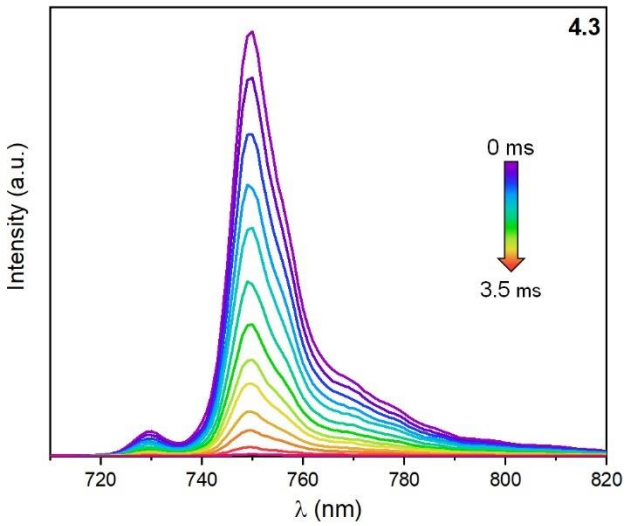

Figure 4.S6. Time-delayed phosphorescence spectrum for **4.3** in 4:1 EtOH:MeOH glass at 77 K and varying delay times.

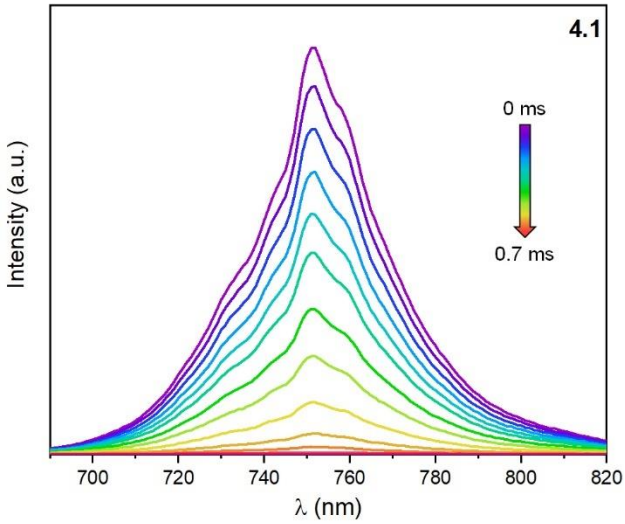

Figure 4.S7. Time-delayed phosphorescence spectrum for **4.1** in 4:1 EtOH:MeOH glass at room temperature and varying delay times.

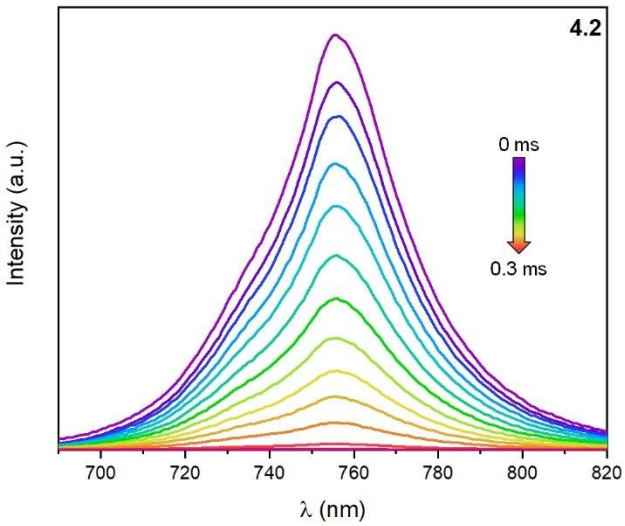

Figure 4.S8. Time-delayed phosphorescence spectrum for **4.2** in 4:1 EtOH:MeOH glass at room temperature and varying delay times.

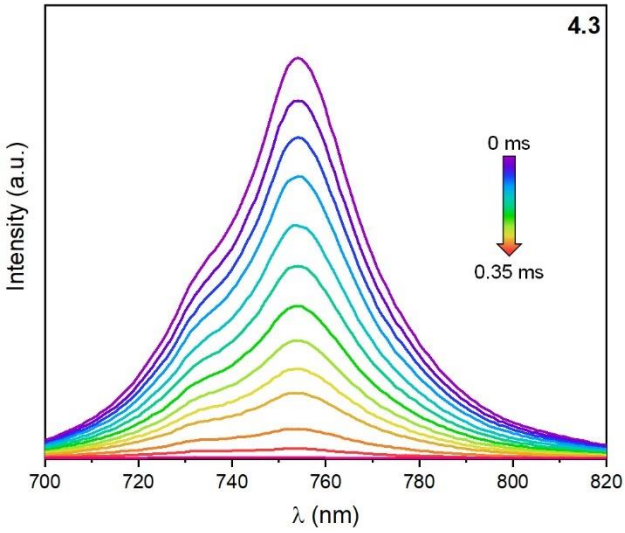

Figure 4.S9. Time-delayed phosphorescence spectrum for **4.3** in 4:1 EtOH:MeOH glass at room temperature and varying delay times.

4.7 References

1. A. Haque, R. A. Al-Balushi, I. J. Al-Busaidi, Md. S. Khan and P. R. Raithby, *Chem. Rev.*, 2018, **118**, 8474–8597

2. J. P. Launay, *Eur. J. Inorg. Chem.*, 2020, **2020**, 329–341

3. C.-L. Ho, Z.-Q. Yu and W.-Y. Wong, *Chem. Soc. Rev.*, 2016, **45**, 5264–5295

4. M. R. Bryce, *J. Mater. Chem. C.*, 2021, in press

5. M. Delor, T. Keane, P. A. Scattergood, I. V. Sazanovich, G. M. Greetham, M. Towrie, A. J. H. M. Meijer and J. A. Weinstein, *Nature Chem*., 2015, **7**, 689–695

6. I. V. Rubtsov, *Nature Chem.*, 2015, **7**, 683–684

7. S. D. Banziger, M. Zeller and T. Ren, *Eur. J. Inorg. Chem.*, 2019, **2019**, 4766–4772

8. S. D. Banziger, X. Li, J. Valdiviezo, M. Zeller, P. Zhang, D. N. Beratan, I. V. Rubtsov and T. Ren, *Inorg. Chem.*, 2019, **58**, 15487–15497

9. R. Taube, H. Drevs and G. Marx, Z. *Anorg. Allg. Chem.*, 1977, **436**, 5–19

10. L. A. Berben and J. R. Long, *J. Am. Chem. Soc.*, 2002, **124**, 11588–11589

11. L. A. Berben, Ph.D. Dissertation, University of California, Berkeley, 2005

12. D. L. Grisenti, W. W. Thomas, C. R. Turlington, M. D. Newsom, C. J. Priedemann, D. G. VanDerveer and P. S. Wagenknecht, *Inorg. Chem*., 2008, **47**, 11452–11454

13. C. Sun, C. R. Turlington, W. W. Thomas, J. H. Wade, W. M. Stout, D. L. Grisenti, W. P. Forrest, D. G. VanDerveer and P. S. Wagenknecht, *Inorg. Chem*., 2011, **50**, 9354–9364

14. L. E. Eddy, P. U. Thakker, C. D. McMillen, J. A. Pienkos, J. J. Cordoba, C. E. Edmunds and P. S. Wagenknecht, *Inorg. Chim. Acta*., 2019, **486**, 141–149

15. J. Nishijo, K. Judai, S. Numao and N. Nishi, *Inorg. Chem*., 2009, **48**, 9402–9408

16. J. Nishijo and M. Enomoto, *Inorg. Chem*., 2013, **52**, 13263–13268

17. J. Nishijo and M. Enomoto, *Inorg. Chim. Acta*., 2015, **437**, 59–63

18. J. Nishijo, Y. Shima and M. Enomoto, *Polyhedron*, 2017, **136**, 35–41

19. W. P. Forrest, Z. Cao, R. Hambrick, B. M. Prentice, P. E. Fanwick, P. S. Wagenknecht and T. Ren, *Eur. J. Inorg. Chem.*, 2012, **2012**, 5616–5620

20. A. López-Hernández, K. Venkatesan, H. W. Schmalle and H. Berke, *Monatsh Chem.*, 2009, **140**, 845–857

21. A. J. Schuman, S. F. T. Robey, E. C. Judkins, M. Zeller, and T. Ren, *Dalton Trans.*, 2021, **50**, 4936–4943

22. S. F. T. Robey, Ph.D. Dissertation, Purdue University, 2017

23. N. F. Curtis and R. W. Hay, *Chem. Commun*., 1966, 524–525

24. N. F. Curtis, *Coordination Chemistry of Macrocyclic Compounds*; G. A. Melson, Ed.; Springer US: Boston, MA, 1979; pp 219–344

25. N. F. Curtis, *Coord. Chem. Rev*., 2018, **366**, 109–134

26. K. Hideg and D. Lloyd, *J. Chem. Soc. D.*, 1970, 929–930

27. K. Hideg and D. Lloyd, *J. Chem. Soc. C*.,1971, 3441–3445

28. R. W. Hay, N. F. Curtis and G. A. Lawrance, *J. Chem. Soc., Perkin Trans. I*. 1975, 591–593

29. S. F. Tyler, E. C. Judkins, Y. Song, F. Cao, D. R. McMillin, P. E. Fanwick and T. Ren, *Inorg. Chem.*, 2016, **55**, 8736–8743

30. E. C. Judkins, S. F. Tyler, M. Zeller, P. E. Fanwick, and T. Ren, *Eur. J. Inorg. Chem*., 2017, **2017**, 4068–4076

31. E. C. Judkins, M. Zeller and T. Ren, *Inorg. Chem*., 2018, **57**, 2249–2259

32. T. D. Cook, S. F. Tyler, C. M. McGuire, M. Zeller, P. E. Fanwick, D. H. Evans, D. G. Peters, and T. Ren, *ACS Omega*, 2017, **2**, 3966–3976

33. B. L. Mash, T. Ren, *J. Organomet. Chem*., 2019, **880**, 143–149

34. B. L. Mash, Y. Yang and T. Ren, *Organometallics*, 2020, **39**, 2019–2025

35. P.-J. Huang, J. V. Garcia, A. Fenwick, G. Wu and P. C. Ford, *ACS Omega*, 2019, **4**, 9181–9187

36. J. Manna, K. D. John and M. D. Hopkins, *Adv. Organomet. Chem*., 1995, **38**, 79–154

37. L. S. Forster, *Chem. Rev*., 1990, **90**, 331–353

38. N. A. P. Kane-Maguire, Photochemistry and Photophysics of Coordination Compounds: Chromium, *Photochemistry and Photophysics of Coordination Compounds I*, V. Balzani and S. Campagna, Springer, Berlin, Heidelberg, 2007

39. A. F. Fucaloro, L. S. Forster, S. G. Glover and A. D. Kirk, *Inorg. Chem*., 1985, **24**, 4242–4246

40. R. B. Lessard, M. J. Heeg, T. Buranda, M. W. Perkovic, C. L. Schwarz, R. Yang and J. F. Endicott, *Inorg. Chem.*, 1992, **31**, 3091–3103

41. N.-H. Chang, H. Mori, X.-C. Chen, Y. Okuda, T. Okamoto and Y. Nishihara, *Chem. Lett.*, 2013, **42**, 1257–1259

42. G. Brizius and U. H. F. Bunz, *Org. Lett.*, 2002, **4**, 2829–2831

43. D. A. House, R. W. Hay and M. A. Ali, *Inorg. Chim. Acta.*, 1983, **72**, 239–245

44. Bruker (2016). Apex3 v2018.7-2, v2019.1-0, SAINT V8.38A, Bruker AXS Inc.: Madison (WI), USA, 2013/2014

45. SHELXTL suite of programs Version 6.14. Bruker Advanced X-ray Solutions. Bruker AXS Inc. 2000-2003, Madison, Wisconsin: USA

46. G. M. Sheldrick, *Acta Cryst. A.*, 2008, **64**, 112–122

47. C. B. Hübschle, G. M. Sheldrick and B. Dittrich, *J. Appl. Crystallogr.*, 2011, **44**, 1281–1284

48. G. M. Sheldrick, *Crystallogr. Sect. C Struct. Chem.*, 2015, **71**, 3–8

49. G. M. Sheldrick (2012). TWINABS. Ver. 2012/1

50. P. van der Sluis and A. L. Spek, *Acta Cryst. A.*, 1990, **46**, 194–201

VITA

Ashley Schuman is a Michigander who grew up near the shores of Lake Huron. She obtained her B.S. in Chemistry from Michigan Technological University and is the first in her family to attend college. While at Michigan Tech, Ashley worked multiple on-campus jobs that involved taking care of plants and helping others learn chemistry. Working as a Chemistry Learning Center (CLC) coach inspired her to pursue a PhD in Chemistry Education.

Ashley began graduate school at Purdue in Fall 2016, where she joined Dr. Roy Tasker's research group. She planned to design guided inquiry organic chemistry laboratory experiments and research laboratory safety. After Dr. Tasker's departure, she took a leap of faith and switched into the Inorganic Division. Ashley joined Dr. Tong Ren's research group in November 2017, where she remained until the completion of her PhD. Throughout her career, Ashley aspires to share her love of chemistry and teaching with others.

LIST OF PUBLICATIONS

1. T. Chi, P. Somers, D. A. Wilcox, A. J. Schuman, V. Iyer, R. Le, J. Gengler, M. Ferdinandus, C, Leibig, L. Pan, X. Xu, and B. W. Boudouris, *J. Polym. Sci., Part B: Polym. Phys*., 2019, **57**, 1462–1475

2. T. Chi, P. Somer, D. A. Wilcox, A. J. Schuman, J. E. Johnson, Z. Liang, X. Xu, B. W. Boudouris, *ACS Appl. Polym. Mater.*, 2021, **3**, 1426–1435

3. A. J. Schuman, A. Raghavan, S. D. C. Banziger, Z.-B. Hu, B. L. Mash, A. L. Williams and T. Ren, *Inorg. Chem.*, 2021, **60**, 4447–4455

4. A. J. Schuman, S. F. T. Robey, E. C. Judkins, M. Zeller and T. Ren, *Dalton Trans.*, 2021, **50**, 4936–4943

5. A. J. Schuman, M. M. Mills, L. A. Miller-Clark and T. Ren, *Submitted to J. Organomet. Chem.*